SAPIENZA
UNIVERSITÀ DI ROMA

Gravitational-Wave Polarizations: a Fundamental Test of Gravity

Facoltà di Scienze Matematiche, Fisiche e Naturali

Corso di Laurea Magistrale in Fisica

Candidate

Samuel Patrone

ID number 1691855

Thesis Advisor

Dr. Francesco Pannarale

Co-Advisor

Prof. Alan J. Weinstein

Academic Year 2019/2020

Thesis defended on 21 July 2020
in front of a Board of Examiners composed by:

Prof. Paolo Mataloni (chairman)
Prof. Maria Chiara Angelini
Prof. Gianluca Cavoto
Prof. John Russo
Prof. Naurang Saini
Prof. Francesco Santanastasio
Prof. Raffaella Schneider

Gravitational-Wave Polarizations: a Fundamental Test of Gravity
Master's thesis. Sapienza – University of Rome

This thesis has been typeset by LaTeX and the Sapthesis class.

Author's email: patrone.1691855@studenti.uniroma1.it

A Nonna Mena,
Reginella del mio cuore

«The last enemy that shall be destroyed is death.»

J. K. Rowling

Acknowledgments

This thesis is based on a research project the author carried out in the context of the Summer Undergraduate Research Program (SURF) at the California Institute of Technology LIGOLab in 2019. The participation in this experience was made possible by the sponsorship of INFN Sezione di Roma and Scuola Superiore di Studi Avanzati Sapienza (SSAS).

A heartfelt and sincere thanks to my mentor Alan J. Weinstein for all the precious insights and support provided during that wonderful research experience, and for having me introduced to the exciting world of gravitational waves. Furthermore, a special thank goes to all the people who made my overseas summer unforgettable, among which I want to personally acknowledge Aaron, Alvin, Gabriele, Luca, Rico, Shruthi, all the fellow SURF students and all the LIGOLab graduate students, post-docs and professors. Nothing of this would have been possible without the precious hospitality of the California Institute of Technology and the Closson's family, who opened the door of their house and their heart to make me feel at home even miles away from it. Thank you, Clemmy, Tim, and Aubrey, for being my west coast American family!

I would like to express my deepest gratitude to my advisor Francesco Pannarale for having worked with me tirelessly at the final version of this dissertation. His adjustments and suggestions were essential for the good result of this thesis. I would like to extend my enthusiastic thanks to all my professors, teachers, and mentors for having me introduced to the wonderful path of knowledge. One among the others, Prof. Mattiacci, who taught me that a journey of a thousand miles begins with a single step and who was next to me when I made the first one.

This thesis is the last milestone of a five-year-long journey, that brought me closer to the understanding of the Universe. Although aware that many things are still obscure and my entire life would not be enough to even grasp a sense of them, I have concluded that no one of us is left alone in the mystery of our existence. Thanks to all my friends for having shared part of their unique being with me. In particular, Alessio, Leonardo, Pierluigi, and Tilde, for being there no matter what over the years. Gioacchino and Daniele, for having walked together through the academic jungle and managed to survive.

What this thesis will not show is how hard it can be to follow your dreams despite the circumstances. Difficulties are part of our life. They are not against us, they make us. However, what I know for sure is that nothing of what I am now would have been possible without the wholehearted support of my family. To my parents, Silde and Amato, to Zia Rosy, Nonno Mimmo, Nonna Pea, Zio Tore, and Zia Sara's east cost family, at risk of sounding sickeningly sweet and inappropriate, I want to say vi amo *from the bottom of my heart. And that's all it is.*

The last lines of these thoughts are dedicated to Nonna Mena and Viviana, who are just waiting for me around the corner...

And - again - to You, because I am.

Abstract

This thesis presents the results of an original and independent research that aims at assessing with software simulations the possibility of inferring the polarization content of a transient gravitational wave (GW) within a Bayesian framework, given the extended network of five ground-based interferometric detectors available in the near future.

A theoretical review on the phenomenon of gravitational radiation in Metric Theories of Gravity is provided and some characteristics of GWs in alternative theories of gravity are reproduced. In particular, it is shown that each theory makes different predictions on the GW polarization modes: this is one of the reasons for which GW polarization measurements are among the strongest fundamental tests we can perform on gravity.

In the central part of the dissertation, we illustrate the working principles of GW interferometers as well as the main data analysis techniques involved in processing GW data. The response in amplitude of a single interferometer to each polarization mode is shown to be determined by the geometry of the source-detector system (up to an overall normalization).

In the last part of the thesis, the response of a network of GW interferometric detectors is studied in order to discriminate among different polarizations. The methodology developed — on simulated data — provides a powerful check for one of the fundamental predictions of General Relativity, and is thus of major significance in both the fundamental physics of gravity and the astrophysics of GW sources.

We find that Bayesian inference can indeed accurately extract the polarization content of transient GW signals, with precision limited by the signal-to-noise ratio (SNR) in the response. As expected, the precision mostly improves with the total network SNR, with some exceptions due either to an SNR distributed very unevenly among the five detectors or to statistical fluctuations in the Bayesian sampler. Most of the code was written from scratch by the author. It is very flexible, as it allows for new ground-based interferometers with two or three arms to be easily added to (or removed from) the network. Such studies are of crucial importance since they can provide strong evidence in support of some particular configurations for future detectors. A technical note on this phenomenological study is publicly available on the LIGO Document Control Center [54].

Contents

Introduction

«Und wir, die an *steigendes* Glück
denken, empfänden die Rührung,
die uns beinah bestürzt,
wenn ein Glückliches *fällt.*»

Rainer Maria Rilke, *Duineser Elegien* X

Even if we do not realize it, we are constantly surrounded by *waves*. Of any kind. We can communicate through electromagnetic waves, we can surf on ocean waves, we can dream thanks to brainwaves, we can see the night sky with light waves, we can feel emotions listening to our favorite sound waves. Waves are everywhere, in our everyday life.

The first to be understood and studied in their fundamental principles were *mechanical waves*, periodical perturbations of a medium that can propagate for long distances. The harmonic motion of each particle of the medium around its starting point of *equilibrium* produces a perturbation that can be transmitted to another particle thanks to the interaction between the two. Three directions are possible in three-dimensional space for their oscillation, and depending on the nature and state of the medium, only some particular directions are allowed. The possible orientation along which the oscillation takes place is called *polarization mode* of the wave. *Transverse waves* are perpendicular to the propagation direction; in *longitudinal waves*, particles of the medium move parallel to the wave propagation vector. Mechanical waves can be of both types: the waves we produce by plucking a guitar string, or sea waves, are transverse, while sound waves are longitudinal.

Waves can also be oscillations of *fields*, physical quantities that can be represented by scalar, spinors, vectors or tensors (according to their properties under rotations) and take a specific value at each point of spacetime. Electromagnetic waves are generated and powered by the self-interaction of variable electric and magnetic fields and propagate all at the same constant velocity (in vacuum), in every system of reference. When electromagnetic waves have some range of frequencies, they become visible to the human eye, being commonly known as light. However, electromagnetic waves are only *transverse*, and this can be seen as a consequence of their propagation speed that does not allow for a longitudinal degree of freedom. In other words, electromagnetic waves have only two polarization modes.

The core of Quantum Physics can be summarized in the fact that particles, which constitute the Universe that surrounds us, can be thought as *quanta* of these fields, finite packets of energy that cannot be further subdivided into smaller ones. This means that the magnitude of the physical property described by fields can take on only discrete values consisting of integer multiples of one quantum. Hence, the *wave-particle duality*. The electromagnetic wave can be described as the propagation of photons, discrete quanta of energy, massless particles which ought to travel at the speed of light to preserve their identity (or more formally, their status as *irreducible representation of the Lorentz group*).

In light of the discussion above, after having understood that spacetime itself can be thought of as a field mediating the gravitational interaction, it does not seem absurd to think about *gravitational waves* (GWs), perturbations that propagate at the speed of light and locally deform spacetime. Indeed, in 1916 Albert Einstein, one year after the formulation the theory of General Relativity (GR), showed that, in the weak-field limit, his linearized field equations for gravity admit a wave-like solution. However, the expected effect was so small that many physicists, including Einstein himself, cast doubts about the possibility to ever be able to detect them. Some even questioned whether those waves were actually real or an artifact of the gauge freedom of the theory. Almost a century later, on the September 14, 2015, LIGO (the Laser Interferometer Gravitational-Wave Observatory) achieved the very first direct detection of a GW signal emitted by two black holes merging. This milestone in experimental gravitational physics started a new era in physics, kick-starting GW astronomy and astrophysics.

Thanks to GWs, not only will we be able to study the most exotic objects of the Universe (such as black holes and neutron stars) and its most extreme events, but also to test GR at unprecedented precision. Currently, all attempts to quantize Gravity, unifying Quantum Field theories with GR, have failed, and consequently led to the development of alternative theories of gravity. Many of these theories diverge from GR in their predictions, and GWs could be of help not only to test GR in the strong field regime, but also to place constraints on alternative theories.

In this thesis, we focus on one characteristic of GWs, their *polarization content*. As any other waves, GWs deform spacetime in some specific direction relatively to their direction of propagation. GR allows for two *tensor* polarizations only, both transverse to the direction of propagation (similar to the electromagnetic case). However, modification of the field equations introduced by alternative theories of gravity can lead to the existence of additional degrees of freedom of the wave, the so-called *vector* or *scalar modes*. This is the reason why the study of GW polarizations provides one of the strongest GR tests we can perform.

In Chapter 1, we analyze in detail the foundations of any metric theory of gravity, developing a theoretical framework, the Parametrized Post-Newtonian (ppN) Framework, that allows for a classification of alternative theories of gravity and that can be used to make predictions in the weak-field regime.

In Chapter 2, we investigate the phenomenon of Gravitational Radiation within the frame of metric theories, reproducing some important results concerning the most distinctive features of these waves. Particular attention is devoted to the polarization degrees: we show, first using the ppN formalism, then with more general arguments within the Newman-Penrose formulation of the theory, that a total of *six* propagating degrees of freedom are allowed for a wave in the most generic metric theory.

In Chapter 3, we study the response of GW interferometers to the perturbation of the metric. We show that the measured amplitude of each polarization depends only on the relative geometry between source and detector, and we present some first original results on the sensitivity of the five-detector network that will be operating in the near future.

In Chapter 4, we review the most updated GW data analysis techniques. We describe filtering techniques to isolate the GW signal from the background noise, and we develop a complete Bayesian framework to statistically infer the characteristic of the wave from the measured data.

In Chapter 5, we present the results of an original and independent research that aims at assessing with software simulations the possibility of inferring the polarization content of a transient GW within a Bayesian framework, given the extended network of five ground-based interferometric detectors. We use a toy model to carry out a model-independent study of the network response, and we show that Bayesian inference can indeed accurately extract the polarization content of transient GW signals, with precision limited by the signal-to-noise ratio (SNR) in the response. Most of the analysis code is written from scratch by the author, and it is very flexible: new ground-based interferometers with two or three arms can be easily added to (or removed from) the network. Such studies are of crucial importance since they can provide strong evidence in support of some particular configurations for future detectors. A technical note on this phenomenological study is publicly available on the LIGO Document Control Center [54].

At the end of the thesis, we provide a short survey of the results obtained and some suggestions on the possible extension of this work that could be carried out in the future.

Chapter 1

Metric Theories of Gravity and the Parametrized Post-Newtonian Formalism

In this first chapter, we will introduce the foundations of any viable Theory of Gravitation. After a brief historical introduction, we will provide a description of what is a generic Metric Theory of Gravity. Then, we will develop the parametrized post-Newtonian (ppN) framework, useful to study and classify the variety of Metric Theories in a weak-field regime. In the last section, some examples of Metric Theories will be provided.

1.1 Early Concepts and Newton's Theory of Gravity

Although Gravity is by far the weakest fundamental interaction of our Universe and it does not play any role in the composition of everyday matter, its long range and universal action dominates the motion of planets, stars and galaxies, allowing humans and scientists to wonder about nature, safely anchored to Earth, one of the many spinning celestial bodies in our Cosmos.

At the dawn of Science (known as *PhilosophiæNaturalis*), Greek philosophers such as *Aristotle (384 - 322 BC)* did not realize that the force responsible for the downwards attraction to the soil was the same that affects celestial bodies in their movements. The perpetually repeating motion of stars and planets in the sky, not necessarily descendent, was thought to be a *natural motion*, consequence of the rotation of celestial spheres to which stars were attached. Two other hypotheses about dynamics were held until the XVI century, that essentially impeded any further comprehension or advancement in mechanics: a constant force is needed for uniform motion and a force can be applied only by direct contact.

The Italian astronomer and natural philosopher *Galileo Galilei (1564-1642)*, who founded the *scientific method* as the winning combination of theory and experiments, was the first to think out of the box and to propose, supported by observation, that a constant force is instead responsible of an accelerated motion. He was also the first physicist to formulate the *Principle of Equivalence*, which states that laws of Physics (or more precisely of Mechanics, as it was the only branch of Natural Philosophy studied at that time) must be invariant under *Galilean Transformations*, coordinate changes between systems of reference in relative motion at constant velocity one respect to the other. Galileo was also the first to show experimentally that bodies fall with the same acceleration regardless of their composition (a statement which will later be known as the *Weak Principle of Equivalence*).

The German astronomer *Johannes Kepler (1571-1630)* was another protagonist in the history of gravitation. His starting point was the *Heliocentric Theory*, first proposed by the Greek philosopher *Aristarchus of Samos (310-230 BC)*, but later argued by the Polish astronomer *Nicolaus Copernicus (1473-1543)*. According to this theory, planets orbit the Sun, not the Earth. Analyzing the data on planets motion collected by the Danish astronomer *Tycho Brahe (1546-1601)*, he was able to formulate his homonimous three quantitative laws of motion for planets orbiting the Sun. He showed that the simplest explanation for planet trajectories in the sky is drawn by the assumption that every planet (in the Solar System) follows an elliptic path around the Sun.

Sir Isaac Newton (1642-1726) was the first to understand that the heavenly motion of the Moon and the earthly one of a free falling body were manifestations of the same force acting at a distance between every massive object in the Universe, without requiring bodily contact. We cannot but quote the well-known formula that captures the principal features of Newton's Gravity:

$$\mathbf{F} = -G\frac{m_1 m_2}{r^2}\hat{\mathbf{r}}\,, \tag{1.1}$$

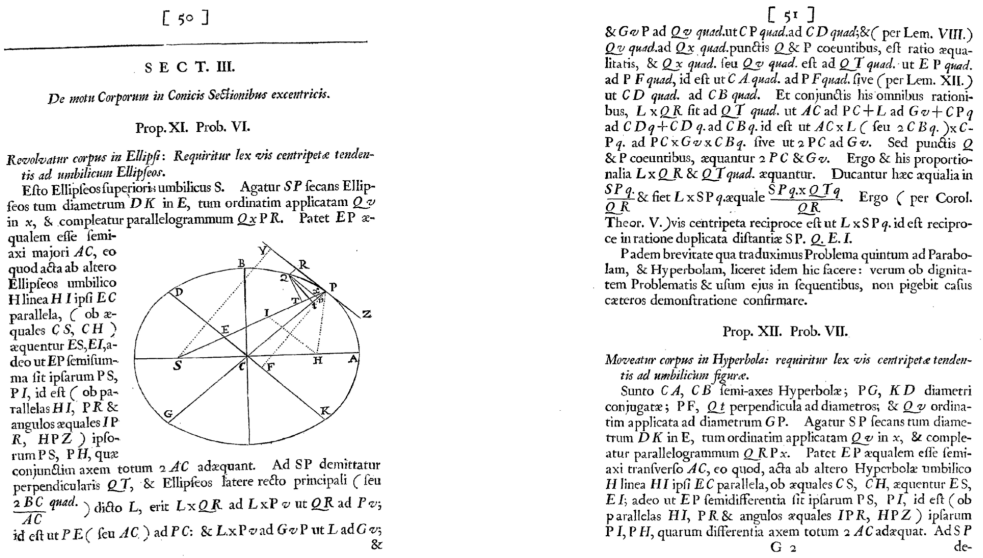

[50]

SECT. III.

De motu Corporum in Conicis Sectionibus excentricis.

Prop. XI. Prob. VI.

Revolvatur corpus in Ellipsi: Requiritur lex vis centripetæ tendentis ad umbilicum Ellipseos.

Esto Ellipseos superioris umbilicus S. Agatur *SP* secans Ellipseos tum diametrum *DK* in *E*, tum ordinatim applicatam *Qv* in *x*, & compleatur parallelogrammum *QxPR*. Patet *EP* æqualem esse semiaxi majori *AC*, eo quod acta ab altero Ellipseos umbilico *H* linea *HI* ipsi *EC* parallela, (ob æquales *CS*, *CH*) æquentur *ES*, *EI*, adeo ut *EP* semisumma sit ipsarum *PS*, *PI*, id est (ob parallelas *HI*, *PR* & angulos æquales *IPR*, *HPZ*) ipsorum *PS*, *PH*, quæ conjunctim axem totum 2*AC* adæquant. Ad *SP* demittatur perpendicularis *QT*, & Ellipseos latere recto principali (seu $\frac{2BC\ quad.}{AC}$) dicto *L*, erit *L* x *QR* ad *L* x *Pv* ut *QR* ad *Pv*; id est ut *PE* (seu *AC*) ad *PC*: & *L* x *Pv* ad *Gv* *P* ut *L* ad *Gv*; &

[51]

& *Gv* *P* ad *Qv quad.* ut *CP quad.* ad *CD quad.*; & (per Lem. VIII.) *Qv quad.* ad *Qx quad.* punctis *Q* & *P* coeuntibus, est ratio æqualitatis, & *Qx quad.* seu *Qv quad.* est ad *QT quad.* ut *EP quad.* ad *PF quad.*, id est ut *CA quad.* ad *PF quad.* (sive (per Lem. XII.) ut *CD quad.* ad *CB quad.* Et conjunctis his omnibus rationibus, *L* x *QR* fit ad *QT quad.* ut *AC* ad *PC* + *L* ad *Gv* + *CP q* ad *CD q* + *CD q.* ad *CB q.* id est ut *AC* x *L* (seu 2*CB q.*) x *CP q.* ad *PC* x *Gv* x *CB q.* sive ut 2*PC* ad *Gv*. Sed punctis *Q* & *P* coeuntibus, æquantur 2*PC* & *Gv*. Ergo & his proportionalia *L* x *QR* & *QT quad.* æquantur. Ducantur hæc æqualia in $\frac{SP\,q.}{QR}$ & fiet *L* x *SP q.* æquale $\frac{SP\,q.\times QT\,q.}{QR}$. Ergo (per Corol. Theor. V.) vis centripeta reciproce est ut *L* x *SP q.* id est reciproce in ratione duplicata distantiæ *SP*. *Q. E. I.*

Padem brevitate qua traduximus Problema quintum ad Parabolam, & Hyperbolam, liceret idem hic facere: verum ob dignitatem Problematis & usum ejus in sequentibus, non pigebit casus cæteros demonstratione confirmare.

Prop. XII. Prob. VII.

Moveatur corpus in Hyperbola: requiritur lex vis centripetæ tendentis ad umbilicum figuræ.

Sunto *CA*, *CB* semi-axes Hyperbolæ; *PG*, *KD* diametri conjugatæ; *PF*, *Qt* perpendicula ad diametros; & *Qv* ordinatim applicata ad diametrum *GP*. Agatur *SP* secans tum diametrum *DK* in *E*, tum ordinatim applicatam *Qv* in *x*, & compleatur parallelogrammum *QRPx*. Patet *EP* æqualem esse semiaxi transverso *AC*, eo quod, acta ab altero Hyperbolæ umbilico *H* linea *HI* ipsi *EC* parallela, ob æquales *CS*, *CH*, æquentur *ES*, *EI*; adeo ut *EP* semidifferentia sit ipsarum *PS*, *PI*, id est (ob parallelas *HI*, *PR* & angulos æquales *IPR*, *HPZ*) ipsarum *PI*, *PH*, quarum differentia axem totum 2*AC* adæquat. Ad *SP*

G 2 de-

Figure 1.1. *PhilosophiæNaturalis Principia Mathematica*, Isaac Newton, (1686). In these pages taken from the first edition of the *Principia*, we can appreciate the geometric proof given by Newton for elliptical trajectories of a body that is subject to a force directed toward one of the ellipse's foci (first law of Kepler).

where $\mathbf{F}$ is the three-vector force acting on the two masses, m_1 and m_2, and $\mathbf{r}$ is the separation vector between them, with the origin of the reference frame centered in one of the two bodies. The minus sign reflects the attractive nature of gravity while G is a proportionality constant, that can be experimentally determined.

Newton's law correctly predicts the orbital motion of planets as described by Kepler's laws (see Fig. 1.1). Gravity is indeed a *central force*: its invariance under rotations implies conservation of angular momentum, which leads to planar and closed orbits. However, the crucial point of Newton's argument is what later was called the *Weak Equivalence Principle* (WEP), already suggested by Galileo's observations: the *inertial mass*, i.e., the resistance that a body opposes to the application of a force, appears to be the same as the *gravitational mass*, the charge of the body subject to gravitational interaction [the m's in Eq. (1.1)]. The importance of this principle was indeed guessed by Newton, who placed it at the beginning of his masterpiece *PhilosophiæNaturalis Principia Mathematica*. The mysterious *action at a distance*, however, seemed to avoid any kind of possible explanation based on the Physics known at that time, and the English scientist humbly commented *«Hypotheses non fingo»* («I feign no hypotheses») on the impossibility of going beyond the descriptions of phenomena to find their cause.

1.2 The Einstein Equivalence Principle

At the beginning of the XX century, a huge revolution in the foundations of Physics was carried out by *Albert Einstein (1879-1955)*, whose articles issued on the *Annalen der Physik* scientific journal in 1905 completely changed our understanding of the world. He succeeded in restoring the equivalence between inertial systems that seemed to be broken by Maxwell's electrodynamics, which is not invariant under Galilean Transformations. In the framework of *Special Relativity*, Space and Time are no more separate entities, but directions in a four-dimensional space in which the maximum velocity allowed is the speed of light, c. The laws of Mechanics and Electrodynamics are the same in every *inertial system of reference* (a modified version of the Galilean Equivalence Principle mentioned before), we only have to replace Galilean Transformations of coordinates with Lorentz ones. At the same time, Einstein led the foundations of Quantum Mechanics postulating the discrete nature of energy in his analysis of the *Photoelectric Effect* and he provided a proof of the existence of atoms based on *Brownian motion*.

In the following years, he went further, trying to reconcile Special Relativity with Gravitation. He started from the well-established WEP, adding a key element that revealed the path to General Relativity. If all bodies fall with the same acceleration in an external gravitational field, then for an observer in a freely falling elevator in the same gravitational field the bodies should be unaccelerated (except for possible tidal effects due to inhomogeneities in the gravitational field, which can be made small by working in a sufficiently small elevator). Thus, the equivalence of a local free falling system of reference to an inertial one, in which *all* laws of Physics must behave under the domain of Special Relativity. This extension of the WEP is called *Einstein Equivalence Principle* (EEP). Following [76], we can formulate it in three separate statements:

Postulate 1.1. The Einstein Equivalence Principle (EEP)

- Weak Equivalence Principle (WEP)*: if an uncharged test body is placed at an initial event in spacetime and given an initial velocity there, then its subsequent trajectory will be independent of its internal structure and composition;*
- Local Lorentz Invariance (LLI)*: the outcome of any local non-gravitational test experiment is independent of the velocity of the (freely falling) apparatus;*
- Local Position Invariance (LPI)*: the outcome of any local non-gravitational test experiment is independent of where and when in the universe it is performed.*

The EEP naturally suggests that gravitation should be a metric effect of curved spacetime, described by what is called a *Metric Theory of Gravity*. Let's briefly sketch the arguments that leads from the EEP to a metric description.

The WEP suggests that in our Universe there are some preferred trajectories along which freely falling bodies move: following these 4-d lines, we can find local frames respect to which bodies are unaccelerated. Invoking the LLI, we can state that around the same point in spacetime $\mathcal{P}$ it is possible to find an infinite set of free

falling frames with different relative velocities such that non-gravitational laws of Physics are the same (i.e, they are described by Lorentz invariant equations). This last condition implies that there will be a set of second-rank tensors $\mathbf{\Psi}^{(A)}_{\mu\nu}$ that in a local freely falling frame reduce to terms proportional to the Minkowski metric, up to a constant dependent on both the specific tensor A and the point $\mathcal{P}$. These dependencies can be parametrized through a scalar field $\phi^{(A)}(\mathcal{P})$. In formulae:

$$\mathbf{\Psi}^{(A)}_{\mu\nu} \to \phi^{(A)}(\mathcal{P})\boldsymbol{\eta}_{\mu\nu} \tag{1.2}$$

where $\boldsymbol{\eta}_{\mu\nu}$ is the Minkowski flat metric.

Physical laws of any local non-gravitational interaction, however, must be independent of the point $\mathcal{P}$ at which they are formulated (LPI). Then, using some simple arguments from differential geometry, one can prove that there must exist a unique, symmetric, second-rank tensor field $\mathbf{g}_{\mu\nu}$, which we will call *metric*, that reduces to the Minkoswki tensor $\boldsymbol{\eta}_{\mu\nu}$ in every local freely falling frame. Furthermore, the metric has a family of preferred worldlines called *geodesics*. At each point $\mathcal{P}$, it is possible to find some reference frames, called *Local Lorentz frames*, which follow these geodesics, such that:

$$\mathbf{g}_{\mu\nu}(\mathcal{P}) = \boldsymbol{\eta}_{\mu\nu} + \mathcal{O}(|x^\alpha - x^\alpha(\mathcal{P})|^2) \tag{1.3}$$

We therefore conclude that Local Lorentz frames are exactly the freely falling frames of the EEP and geodesics must be the trajectories of freely falling bodies. In the next section, the postulates of metric theories of gravity will be analyzed.

Here we wish to stress how the EEP, suggesting that any viable theory of gravity must be metric, indirectly solves one of the greatest mysteries of gravitation, the so-called Newtonian *action at a distance*. There is no longer need for this artifact to explain gravitational attraction since gravity is only a consequence of curved spacetime, a local property of the Universe itself. Newton's starting point (the WEP) was correct, but his conception of space and time as separate and absolute entities misled him, preventing him from going further.

1.3 Metric Theories of Gravity

In the previous section, we argued that the effect of gravity must be equivalent to the ones produced by a curved spacetime in which freely falling objects follow special trajectories, called *geodesics of the metric*. It turns out that the most general Theory of Gravity, assuming EEP as the founding principle of our Universe, has some peculiar characteristics. In the following, we first analyze the properties of a *Metric Theory of Gravity*, focusing our attention on Lagrangian-based theories, for which an important result holds. We will then provide a first classification for Metric theories, mainly based on the gravitational fields we include in our theory. Finally, we will modify EEP to include gravitational experiments: this will lead to the definition of the Strong Equivalence Principle (SEP), valid in (but non exclusive of) General Relativity.

1.3.1 Definition

We can write three postulates that constitute the essential requirements for any Metric Theory of Gravity:

Postulate 1.2. Metric Theory of Gravity

- *Spacetime is endowed with a metric* $\boldsymbol{g}$*;*
- *Free falling bodies follow the metric geodesics;*
- *In local Lorentz frames, the non-gravitational laws of physics are those of Special Relativity.*

To understand what the properties of a generic Metric Theory of Gravity are and how we can generate (and parametrise) different theories that obey the EEP, we must introduce some definitions, following [67]. First of all, we will restrict our attention to a subclass of all possible generally covariant physical theories, called *Lagrangian-based, relativistic theories*. These theories are based on an action principle that, with extremization with respect to variations of all dynamical variables, generates all the dynamical laws of the theory. The Lagrangian density $\mathcal{L}$ can be split into two contributions $\mathcal{L} = \mathcal{L}_G + \mathcal{L}_{NG}$. The gravitational part, $\mathcal{L}_G$, is the largest part and it contains only gravitational fields. The non-gravitational part, $\mathcal{L}_{NG}$, is the remainder: when gravity is turned off, it approaches the total Lagrangian of Special Relativity.

We then define what it means for such a theory to be *universally coupled*.

Definition 1.3 (Universal coupling)**.** *A generally covariant Lagrangian-based relativistic theory is* universally coupled *if it can be cast into a mathematical form (representation) in which the action for matter and non-gravitational fields* I_{NG} *contains precisely one gravitational field: a symmetric, second-rank tensor* $\mathbf{g}_{\mu\nu}$ *that reduces to* $\boldsymbol{\eta}_{\mu\nu}$ *when gravity is turned off; and when* $\mathbf{g}_{\mu\nu}$ *is replaced by* $\boldsymbol{\eta}_{\mu\nu}$*,* I_{NG} *becomes the action of Special Relativity.*

It can be proved that any Lagrangian-based theory universally coupled is a Metric Theory and vice versa (see [67] for details). This theorem stresses the fact that independently on how many gravitational fields we consider in our theory, matter and non-gravitational fields, within the context of a Lagrangian-based relativistic Metric Theory, only couple with the metric $\mathbf{g}_{\mu\nu}$. Therefore, we can consider the metric as a property of the spacetime itself, rather than a field over spacetime.

1.3.2 Classification

The fact that matter and non-gravitational fields are essentially oblivious to extra gravitational fields other than the metric does not mean that these last have no role in gravitation theory: they alter and modify the way in which matter and non-gravitational fields generate spacetime curvature and produce the metric. Based on the different kind of gravitational fields we can add to our theory, we can distinguish between two broad classes:

- *Purely dynamical*: Metric theories whose gravitational fields have their structure and evolution determined by coupled differential equations;
- *Prior-geometric*: Metric theories for which there is at least one gravitational field whose structure and evolution is given *a priori*, independent on the other fields of the theory.

Furthermore, depending on the nature of the extra gravitational fields, we can have different effects that influence the results of local gravitational experiments. Consider a frame sufficiently small that inhomogeneities of external gravitational fields can be neglected, but large enough to encompass a system of gravitating bodies: we will call it *quasi-local Lorentz Frame*. Gravitational-like experiments can be influenced by the presence of external gravitational fields (not coupled with matter and non-gravitational fields) through the values they assume at the boundary of the local frame. These boundary conditions alter and modify the metric generated by the local system, making local gravitational experiments sensitive to the location or velocity of the *quasi-local Lorentz Frame* with respect to the external environment. In other words, we can have a violation of the equivalence principle for *gravitational experiments*. We ought to point out that there is no EEP violation, since non-gravitational experiments couple only to the metric that can always be made locally Minkowskian. Depending on the nature of the extra gravitational fields in the theory, we can distinguish three main behaviours:

- *Metric-only theories*: if there is only the metric $\mathbf{g}_{\mu\nu}$; local gravitational physics is independent of location and velocity of the local system;
- *Dynamical Scalar theories*: if there are some dynamical scalar fields $\phi^{(A)}$ besides the metric; local gravitational physics may depend on the location of the frame.
- *Dynamical Vector-Tensor or prior-geometric theories*: if there are additional dynamical vector-tensor gravitational fields or prior-geometric fields besides the metric; local gravitational physics may depend on both the location and the velocity of the frame.

1.3.3 The Strong Equivalence Principle

General Relativity (GR) is the simplest Metric Theory of Gravity we can imagine, with only one gravitational field, the metric $\mathbf{g}_{\mu\nu}$. Based on the previous observations, we are tempted to reformulate the Einstein Equivalence Principle to include gravitational experiments, seeking a founding postulate for GR. We can state the Strong Equivalence Principle (SEP) in the following way [75]:

Postulate 1.4. The Strong Equivalence Principle (SEP)

- Gravitational Weak Equivalence Principle (GWEP)*: WEP is valid for self-gravitating bodies as well as for test bodies;*

- Local Lorentz Invariance (LLI)*: the outcome of any local test experiment is independent of the velocity of the (freely falling) apparatus;*
- Local Position Invariance (LPI)*: the outcome of any local test experiment is independent of where and when in the universe it is performed.*

With respect to the EEP, the SEP includes self-gravitating bodies as well as gravitational experiments. Although the conjecture

$$\text{SEP} \Rightarrow \text{GR}$$

seems very likely, there is presently no rigorous proof of it. Further, there are some quantum-inspired modifications of GR (known as R^2*-terms* theories) that at very small scale provide a counterexample to the previous statement. However, since several metric theories (with GR as the notable exception) are expected to violate the Strong Equivalence Principle in some way, SEP testing plays an essential role in the research of the ultimate theory of gravity.

1.4 The Parametrized Post-Newtonian Formalism

The parametrized post-Newtonian (ppN) limit of a metric theory of Gravity was first developed by *Kenneth Nordtvedt, Jr. (1939)* in [51], extending the work initiated by Eddington, Robertson and Schiff. It was later modified by *Clifford M. Will (1946)* in [74] to include hydrodynamics. The full and most generalized version we present in the following was elaborated by Nordtvedt and Will in [77] and it is regarded as the canonical ppN framework for the choice of parameters and gauges. We begin with a brief review of the Newtonian limit of any metric theory, which allows us to establish the connection between the metric and gravitational potentials.

1.4.1 The Geodesic Equation and The Newtonian Limit

To understand the connection and the correspondence between Newton's theory and its metrical generalization, we start with the aforementioned WEP (see Postulate 1.1), trying to find the equation of motion for a test particle that is freely falling in a homogeneous gravitational field. If we place ourselves in the Local Lorentz frame, which the Equivalence Principle always allows us to do, we do not see the particle subject to any acceleration. The particle moves instead along a straight line in a four dimensional space: in this local frame, it is simply a free particle under laws of Special Relativity. If we call ξ^α the coordinates in this frame and τ the test particle's proper time (that is both a Lorentz invariant and the time coordinate in the comoving Lorentz Frame), we can write:

$$\frac{\mathrm{d}^2\xi^\alpha}{\mathrm{d}\tau^2} = 0\,. \tag{1.4}$$

We now consider a generic transformation of coordinates — a *diffeomorphism* in the language of differential geometry — expressed by the relation $\xi^\alpha = \xi^\alpha(x^\mu)$. Consequently, the coordinate displacement has to change accordingly:

$$\mathrm{d}\xi^\alpha = \frac{\partial \xi^\alpha}{\partial x^\mu}\mathrm{d}x^\mu \,. \tag{1.5}$$

After some manipulations, we can rewrite Eq. (1.4) in the x-coordinate system as follows:

$$0 = \frac{\mathrm{d}^2\xi^\alpha}{\mathrm{d}\tau^2} = \frac{\mathrm{d}}{\mathrm{d}\tau}\left(\frac{\partial \xi^\alpha}{\partial x^\mu}\frac{\mathrm{d}x^\mu}{\mathrm{d}\tau}\right) = \frac{\mathrm{d}^2 x^\mu}{\mathrm{d}\tau^2} + \left[\frac{\partial x^\mu}{\partial \xi^\alpha}\frac{\partial^2 \xi^\alpha}{\partial x^\rho \partial x^\sigma}\right]\frac{\mathrm{d}x^\rho}{\mathrm{d}\tau}\frac{\mathrm{d}x^\sigma}{\mathrm{d}\tau} \,. \tag{1.6}$$

We can define the functions in the square brackets as the *Christoffel Symbols* (also called *Affine Connections*), using the following notation:

$$\Gamma^\mu_{\rho\sigma} \equiv \frac{\partial x^\mu}{\partial \xi^\alpha}\frac{\partial^2 \xi^\alpha}{\partial x^\rho \partial x^\sigma} \,. \tag{1.7}$$

The $\Gamma^\mu_{\rho\sigma}$ symbols vanish completely in the Local Lorentz frame, as we can see restoring $x^\mu = \xi^\mu$ in Eq. (1.6) and checking its consistency with Eq. (1.4). Further, they are symmetric over the two low indices and they are not tensors, otherwise they would have to vanish in every system of reference. Equation (1.6) is called the *geodesic equation* and it identifies special trajectories in curved spacetime along which a freely falling body moves.

Differential geometry provides an alternative description for Christoffel symbols. They naturally emerge when we deal with the definition of *covariant derivative*. Without going through the specific derivation (which is available in standard texts of General Relativity, e.g. [48]), we quote only their relation to the metric. Indeed, the requirement that geodesics coincide with the *straight lines* in the local Lorentz geometry allows us to uniquely define Christoffel symbols as linear combinations of the first derivative of the metric. In formulae:

$$\Gamma^\mu_{\rho\sigma} = \frac{1}{2}g^{\mu\alpha}(g_{\alpha\rho,\sigma} + g_{\alpha\sigma,\rho} - g_{\rho\sigma,\alpha}) \,, \tag{1.8}$$

where we used the coma convention for partial derivative, i.e. $g_{\alpha\rho,\sigma} = (\partial/\partial x^\sigma)g_{\alpha\rho}$.

Let's now see how the geodesic equation modifies in the Newtonian limit of the theory. When the gravitational potential is sufficiently small and velocities are much smaller than the speed of light, the Newtonian approximation works properly. We can describe this limit with coordinates that are as nearly globally Lorentz as possible:

$$g_{\mu\nu} = \eta_{\mu\nu} + h_{\mu\nu} \quad \text{with} \quad |h_{\mu\nu}| \ll 1 \text{ and } |v^j| = \left|\frac{\mathrm{d}x^j}{\mathrm{d}t}\right| \ll 1 \,. \tag{1.9}$$

Since at this level of approximation $\mathrm{d}t/\mathrm{d}\tau \approx 1$, using the *geodesic equation* (1.6) and the relation between the metric and Christoffel symbols of Eq. (1.8), we can write:

$$\frac{\mathrm{d}^2 x^i}{\mathrm{d}t^2} \approx \frac{\mathrm{d}^2 x^i}{\mathrm{d}\tau^2} = -\Gamma^i_{\rho\sigma}\frac{\mathrm{d}x^\rho}{\mathrm{d}\tau}\frac{\mathrm{d}x^\sigma}{\mathrm{d}\tau} \approx -\Gamma^i_{00} = \frac{1}{2}h_{00,i} - h_{0i,0} \,. \tag{1.10}$$

We can further simplify Eq. (1.10) noticing that, in the Newtonian limit, time derivatives of the metric are much smaller than spatial derivatives, as we can intuitively see from a dimensional analysis argument ($h_{\alpha\beta,0} \sim v h_{\alpha\beta,i}$). In the Newtonian approximation, we therefore obtain the following relation:

$$\frac{\mathrm{d}^2 x^i}{\mathrm{d}t^2} \approx \frac{1}{2} h_{00,i} \,. \tag{1.11}$$

Recalling some notions of classical mechanics and conservative forces, we can express the acceleration as the gradient of a scalar function U, called the *gravitational potential*. Given a distribution of matter described by the density $\rho(\mathbf{x}, t)$, we have that:

$$\frac{\mathrm{d}^2 x^i}{\mathrm{d}t^2} = \frac{\partial U}{\partial x_i} \quad \text{where} \quad U(\mathbf{x}, t) = \int \frac{\rho(\mathbf{x}', t)}{|\mathbf{x} - \mathbf{x}'|} \mathrm{d}^3 x' \,. \tag{1.12}$$

Comparing Eqs. (1.11) and (1.12), we find that the Newtonian limit for the metric perturbation h is:

$$h_{00} = 2U \,, \quad h_{0i} = h_{ij} = 0 \,. \tag{1.13}$$

This relation is crucial since it shows that Newtonian gravity can be seen, from the metric point of view, as a *warped time* first order effect. The invariant line element $\mathrm{d}s^2$ will consequently differ from the Minkoskian one, being:

$$\mathrm{d}s^2 = g_{00}\mathrm{d}t^2 + \mathrm{d}x^2 + \mathrm{d}y^2 + \mathrm{d}z^2 = (-1 + 2U)\mathrm{d}t^2 + \mathrm{d}x^2 + \mathrm{d}y^2 + \mathrm{d}z^2 \,. \tag{1.14}$$

The *geodesic equation* (1.6) can be found in a more elegant way starting from a variational principle for a free falling particle, extremizing the free action:

$$\begin{aligned} S_{NG} &= -m_0 \int \mathrm{d}\tau = -m_0 \int \left(- g_{\mu\nu} \frac{\mathrm{d}x^\mu}{\mathrm{d}t} \frac{\mathrm{d}x^\nu}{\mathrm{d}t} \right)^{1/2} \mathrm{d}t \\ &= -m_0 \int (-g_{00} - 2g_{0j} v^j - g_{jk} v^j v^k)^{1/2} dt \,. \end{aligned} \tag{1.15}$$

In the integrand of Eq. (1.15), we recognize the Lagrangian L for a single particle in a metric gravitational field, which in the Newtonian limit reproduces the well-known result[1]:

$$L = -m_0 (1 - 2U - v^2)^{1/2} \approx -m_0 + \frac{1}{2} m_0 v^2 + m_0 U \,. \tag{1.16}$$

1.4.2 Post-Newtonian Variables and Expansion

The main goal of this section is to further expand (in the most generic way) the Lagrangian at the following orders in the perturbation of the metric. This will lead to the definition of other gravitational potentials and it will allow to make quantitative prediction on the possible deviations from Newton's theory of gravity, generically called *post-Newtonian* effects. Among these last, we can only but quote the iconic perihelion advance of Mercury, which is certainly one of the most famous tests of General Relativity within the Solar System.

[1] Apart from a constant factor $-m_0$ and a minus sign in front of the third term, due to the convention we implicitly used to define $U = -\Phi$, where Φ is the classical gravitational potential.

The post-Newtonian framework works when we are dealing with *weak gravitational fields* and we are in a *slow-motion approximation*, i.e. velocities are much smaller than the speed of light. Let's first describe the variables we will use to describe the energy-matter content of the system:

- U is the *gravitational potential* as defined in Eq. (1.12);
- ρ is the *mass density* of the system, which can be viewed as a measure of the number density of baryons n multiplied by a standard rest mass per baryon μ_0 in a standard state, measured in a local, free falling, comoving frame;
- p is the *pressure* (for a perfect fluid, the diagonal components of the energy momentum tensor in the Lorentz Local frame);
- Π is the ratio of the total energy density (all other forms, such as compressional, thermal, magnetic, radiative) to rest mass density ρ; we can write for the total energy $E \sim \rho\Pi\mathcal{V}$, where $\mathcal{V}$ is the total volume.

Assuming a *perfect fluid* description for matter, we can write the energy-momentum tensor $T^{\mu\nu}$ in a fully covariant form (for details about hydrodynamics in curved spacetime, we refer to [76], Section 3.2):

$$T^{\mu\nu} = (\rho + \rho\Pi + p)u^\mu u^\nu + pg^{\mu\nu}\,, \tag{1.17}$$

where $u^\mu = \mathrm{d}x^\mu/\mathrm{d}\tau$ is the four-velocity of the fluid element. As long as the equations of motion for the non-gravitational matter hold, we can prove the local conservation of the energy-momentum tensor, expressed by the vanishing of its covariant derivative $\nabla_\nu T^{\mu\nu} = 0$ (valid in every frame):

$$\begin{aligned}\nabla_\nu T^{\mu\nu} \equiv T^{\mu\nu}{}_{;\nu} &= T^{\mu\nu}{}_{,\nu} + \Gamma^\nu_{\nu\alpha}T^{\mu\alpha} + \Gamma^\mu_{\alpha\nu}T^{\alpha\nu} \\ &= \frac{1}{\sqrt{-g}}\partial_\nu(\sqrt{-g}T^{\mu\nu}) + \Gamma^\mu_{\alpha\nu}T^{\alpha\nu} = 0\,,\end{aligned} \tag{1.18}$$

with $g = \det(g_{\mu\nu})$ and we have introduced the usual notation convention for covariant derivative $\nabla_\mu\phi \equiv \phi_{;\mu}$. To fully describe hydrodynamics in curved spacetime, we can add to Eq. (1.18) the rest mass conservation law (or, alternatively, the baryonic number conservation law). Its covariant form is the following:

$$\begin{aligned}(\rho u^\mu)_{;\mu} &= 0\,, \\ \sqrt{-g}(\rho u^\mu)_{;\mu} = (\sqrt{-g}\rho u^\mu)_{,\mu} &= \frac{\partial}{\partial t}\rho^* + \frac{\partial}{\partial x^j}(\rho^* v^j) = 0\,,\end{aligned} \tag{1.19}$$

The manipulations in the second line lead us to the definition of the variable $\rho^* \equiv \rho\sqrt{-g}u^0$ which satisfies the "Eulerian" continuity equation in any $(t, \mathbf{x})$ coordinate system.

Let ϵ be an adimensional small parameter through which we will expand the metric. We can use the virial theorem for a gravitationally bound system (the solar system, for example) to relate the mean velocity of its components to the mean value of the gravitational potential U. By order of magnitudes, we can write (in geometrized units):

$$v^2 \sim U \sim \mathcal{O}(\epsilon^2)\,. \tag{1.20}$$

Assuming *hydrostatic equilibrium*, we can relate density and pressure to the potential:

$$p/\rho \sim U \sim \mathcal{O}(\epsilon^2)\,. \tag{1.21}$$

Furthermore, from thermodynamics we can link the total energy to the pressure of the system by:

$$E \sim p\mathcal{V} \sim \rho\Pi\mathcal{V} \quad \Rightarrow \quad \Pi \sim p/\rho \sim \mathcal{O}(\epsilon^2)\,. \tag{1.22}$$

To complete our overview by order of magnitudes of the variables, we observe that *far from the radiation zone* changes in time of all quantities at fixed position are due primarily to the motion of matter, in formulae:

$$\frac{\partial}{\partial t} \sim \mathbf{v}\cdot\nabla \quad \Rightarrow \quad \frac{|\partial/\partial t|}{|\partial/\partial x|} \sim \mathcal{O}(\epsilon)\,. \tag{1.23}$$

If we recall the general form of the Lagrangian L introduced in Eq. (1.16), we can notice that the Newtonian approximation is given by corrections up to order $\mathcal{O}(\epsilon^2)$ in the metric. To find the post-Newtonian approximation, it is sufficient to go up to order $\mathcal{O}(\epsilon^4)$, as can be explicitly seen by writing the Lagrangian as:

$$L = -m_0\left(1 - 2U - v^2 - \delta g_{00}[\mathcal{O}(\epsilon^4)] - 2\delta g_{0j}[\mathcal{O}(\epsilon^3)]v^j - \delta g_{jk}[\mathcal{O}(\epsilon^2)]v^j v^k\right)^{1/2}\,. \tag{1.24}$$

We have not included in the Lagrangian expansion odd-order terms. Since they contain odd number of velocities $\mathbf{v}$ or time derivatives $\partial/\partial t$, they are not invariant under time inversion and they represent dissipative effects. $\mathcal{O}(\epsilon)$ and $\mathcal{O}(\epsilon^3)$ are respectively forbidden by conservation of rest-mass energy (baryon number) and conservation of energy in the Newtonian limit. Beyond $\mathcal{O}(\epsilon^4)$, different theories make different predictions.

1.4.3 Post-Newtonian Potentials and Metric

Although at first sight for an exact description of a perfect fluid in any metric theory of gravity a formal solution of the field equations in each theory seems to be needed, we can guess the general form of the metric corrections by parametrizing them with suitable *post-Newtonian potentials*. These are functionals of the matter variables we described in the previous section, computed up to the order required by consistency of the expansion. Unfortunately there are an infinite number of such potentials. To perform any reasonable calculation, we have to assume some constraints to restrict their number, in part as evidence obtained from known results in other gravitation theories. Following [48], we assume for the corrections δg to the metric in post-Newtonian approximation that:

1. they have to be of the order written in Eq. (1.24);
2. they must be dimensionless (in geometrized units);
3. under rotations, δg_{00} must be scalar, δg_{0j} vector and δg_{jk} a two index 3-tensor and should be built by appropriate combinations of the variables associated with the matter distribution;

4. the coordinates must asymptotically reduce to the global Lorentz frame and the metric to flat spacetime at $r \to \infty$: this is possible if we assume that the corrections die out at least as fast as $1/r$;

5. for simplicity, the functionals are generated only by rest mass density ρ (or better its modified "Eulerian" version ρ^*), the energy density Π, pressure p and their combinations with velocity, not by their gradients.

We have to specify a coordinate system in which to carry out our computations of the metric corrections. We will use a *local quasi-Cartesian* system (also referred to as *ppN coordinates*) with coordinates $(t, x^j) = (t, x_j)$ as nearly Lorentz as possible. We further assume that the center of mass of the local fluid is at rest with respect to a *universal rest frame*, in which the universe appears isotropic. Although it can be proved that the surrounding cosmological setting may be ignored when imposing asymptotic boundary conditions to the metric, cosmological boundary conditions of auxiliary fields can be crucial (for details, see Section 4.1.3 in [76]). As a first step, we redefine the *Newtonian potential* U, using the conserved density ρ^*:

$$U(t, \mathbf{x}) \equiv \int \frac{\rho^*(t, \mathbf{x}')}{|\mathbf{x} - \mathbf{x}'|} \mathrm{d}^3 x' \quad , \quad \nabla^2 U = -4\pi\rho^* \, . \tag{1.25}$$

Dropping the explicit dependency on primed coordinates for matter variables (e.g. $\rho^*(t, \mathbf{x}') \equiv \rho^{*\prime}$), we can build the following potentials, in order to expand the metric:

- $\delta g_{jk}[\mathcal{O}(\epsilon^2)]$: it must be a 3-tensor, the only terms allowed are $U\delta_{jk}$ and U_{jk} where

$$U_{jk} \equiv \int \rho^{*\prime} \, \frac{(x - x')_j (x - x')_k}{|\mathbf{x} - \mathbf{x}'|^3} \, \mathrm{d}^3 x' \, , \tag{1.26}$$

  related by the superpotential

$$X \equiv \int \rho^{*\prime} \, |\mathbf{x} - \mathbf{x}'| \, \mathrm{d}^3 x' \, , \tag{1.27}$$

  such that:

$$X_{,jk} = U\delta_{jk} - U_{jk} \, . \tag{1.28}$$

- $\delta g_{0j}[\mathcal{O}(\epsilon^3)]$: we can build out two 3-vector potentials V_j and W_j:

$$\begin{aligned} V_j &\equiv \int \rho^{*\prime} \, \frac{v'_j}{|\mathbf{x} - \mathbf{x}'|} \, \mathrm{d}^3 x' \quad , \quad \nabla^2 V_j = -4\pi\rho^* v_j \, , \\ W_j &\equiv \int \rho^{*\prime} \, \frac{\mathbf{v}' \cdot (\mathbf{x} - \mathbf{x}')(x - x')_j}{|\mathbf{x} - \mathbf{x}'|^3} \, \mathrm{d}^3 x' \, . \end{aligned} \tag{1.29}$$

  These also are related to the superpotential X by:

$$X_{,0j} = W_j - V_j \, . \tag{1.30}$$

- $\delta g_{00}[\mathcal{O}(\epsilon^4)]$: we can build several scalar potentials at fourth order in ϵ. We will limit ourselves to contributions from U^2 and the following other possibilities:

$$\begin{aligned}
\Phi_1 &\equiv \int \rho^{*\prime}\, \frac{v'^2}{|\mathbf{x}-\mathbf{x}'|}\, \mathrm{d}^3x' \quad , \qquad \nabla^2\Phi_1 = -4\pi\rho^* v^2\,,\\
\Phi_2 &\equiv \int \rho^{*\prime}\, \frac{U'}{|\mathbf{x}-\mathbf{x}'|}\, \mathrm{d}^3x' \quad , \qquad \nabla^2\Phi_2 = -4\pi\rho^* U\,,\\
\Phi_3 &\equiv \int \rho^{*\prime}\, \frac{\Pi'}{|\mathbf{x}-\mathbf{x}'|}\, \mathrm{d}^3x' \quad , \qquad \nabla^2\Phi_3 = -4\pi\rho^* \Pi\,,\\
\Phi_4 &\equiv \int \frac{p'}{|\mathbf{x}-\mathbf{x}'|}\, \mathrm{d}^3x' \qquad , \qquad \nabla^2\Phi_4 = -4\pi p\,,\\
\Phi_5 &\equiv \int \rho^{*\prime}\nabla' U' \cdot \frac{(\mathbf{x}-\mathbf{x}')}{|\mathbf{x}-\mathbf{x}'|}\, \mathrm{d}^3x'\,,\\
\Phi_6 &\equiv \int \rho^{*\prime}\frac{(\mathbf{v}'\cdot(\mathbf{x}-\mathbf{x}'))^2}{|\mathbf{x}-\mathbf{x}'|^3}\, \mathrm{d}^3x'\,,\\
\Phi_W &\equiv \int\int \rho^{*\prime}\rho^{*\prime\prime}\frac{(\mathbf{x}-\mathbf{x}')}{|\mathbf{x}-\mathbf{x}'|^3}\cdot\left[\frac{(\mathbf{x}'-\mathbf{x}'')}{|\mathbf{x}-\mathbf{x}''|} - \frac{(\mathbf{x}-\mathbf{x}'')}{|\mathbf{x}'-\mathbf{x}''|}\right]\mathrm{d}^3x'\mathrm{d}^3x''\,.
\end{aligned} \tag{1.31}$$

Using a suitable gauge transformation, known as the *standard ppN gauge*, we can make the spatial part of the metric diagonal and isotropic by removing both the U_{jk} and Φ_5 dependency[2]. We are therefore left with 10 potentials, associated to the metric corrections:

$$\begin{aligned}
&\delta g_{jk}[\mathcal{O}(\epsilon^2)]: \; U\delta_{jk}\,,\\
&\delta g_{0j}[\mathcal{O}(\epsilon^3)]: \; V_j,\; X_{,0j}\,,\\
&\delta g_{00}[\mathcal{O}(\epsilon^4)]: \; U^2,\; \Phi_1,\; \Phi_2,\; \Phi_3,\; \Phi_4,\; \Phi_6,\; \Phi_W\,.
\end{aligned}$$

Choosing the following ten conventional parameters, denoted by γ, β, ξ, α_1, α_2, α_3, ζ_1, ζ_1, ζ_3, ζ_4 we can finally write the *ppN metric*:

$$g_{00} = -1 + 2U + 2(\psi - \beta U^2) + \mathcal{O}(\epsilon^6)\,, \tag{1.32a}$$

$$g_{0j} = -\frac{1}{2}[4(1+\gamma)+\alpha_1]V_j - \frac{1}{2}[1+\alpha_2-\zeta_1+2\xi]X_{,0j} + \mathcal{O}(\epsilon^5)\,, \tag{1.32b}$$

$$g_{jk} = (1+2\gamma U)\delta_{jk} + \mathcal{O}(\epsilon^4)\,. \tag{1.32c}$$

where

$$\begin{aligned}
\psi :=& \frac{1}{2}(2\gamma+1+\alpha_3+\zeta_1-2\xi)\Phi_1 - (2\beta-1-\zeta_2-\xi)\Phi_2 + (1+\zeta_3)\Phi_3\\
&+ (3\gamma+3\zeta_4-2\xi)\Phi_4 - \frac{1}{2}(\zeta_1-2\xi)\Phi_6 - \xi\Phi_W\,.
\end{aligned} \tag{1.33}$$

The parameters are chosen to have a special physical significance, as summarized in Fig. 1.2. Although strictly speaking their numerical values depend on the coordinates choice for a given solution, we can give a heuristic interpretation of them by studying their value in GR, for some characteristic coordinates and metric. In

[2]The desired simplification is obtained by using the gradient of the superpotential $X_{,\mu}$ as infinitesimal coordinates shift. See Section 4.2.2 of [76] for details.

Parameter	What it measures relative to GR	GR value	Semi-conservative theories	Fully-conservative theories
γ	How much spatial curvature produced by mass?	1	γ	γ
β	How much nonlinearity in superposition of gravity?	1	β	β
ξ	Preferred-location effects?	0	ξ	ξ
α_1	Preferred-frame effects?	0	α_1	0
α_2		0	α_2	0
α_3		0	0	0
α_3	Is total momentum	0	0	0
ζ_1	conserved?	0	0	0
ζ_2		0	0	0
ζ_3		0	0	0
ζ_4		0	0	0

Note that α_3 is listed twice to indicate that it is a measure of two separate effects.

Figure 1.2. *Physical interpretation of ppN parameters.* This table, reproduced from [76], provides a heuristic explanation of the ppN parameters chosen in the canonical parametrized post-Newtonian framework. The third column reports generic values for the parameters. The last two columns list non-vanishing parameters in two classes of metric theories for which they are computed. For additional details, see Sec. 1.4.4.

the Schwarzschild solution to the GR equations expressed in *isotropic coordinates*, we see that $\gamma = \beta = 1$ and all the other parameters vanish. The coefficient β can be seen as a proxy to quantify the non-linearity of the theory (it multiplies the U^2 term of the metric) with respect to GR, while the coefficient γ can be thought of as a measure of how much spatial curvature is produced by the unit mass.

1.4.4 Post-Galilean Transformations and Preferred Frame Effects

In order to understand the meaning of the ppN parameters other than β and γ, it is useful to study how the metric changes under the action of a coordinate transformation that allows the center of mass of the fluid to move with a velocity $\mathbf{w}$ with respect to the *universe rest frame*, for $|\mathbf{w}| \sim \mathcal{O}(\epsilon)$. In Sec. 1.3.2, we provided a classification of generic metric theories based on their behaviour under local Lorentz transformations, i.e. on the possible dependency of gravitational experiments on the velocity of the chose *quasi-local Lorentz* frame. We said that for *Metric-only theories* (such as GR) and *Dynamical scalar theories*, local gravitational physics is independent from the coordinates chosen. Therefore, for such theories the ppN metric should be invariant under any transformation of coordinates *within* the post-Newtonian approximation, which we will now show.

We first generalize the metric to take into account coordinate-frame motion relative to the universal rest frame by considering the coordinates subject to a *post-Galilean transformation* (first introduced in [18] by Chandrasekhar and Contopolous). This class of transformations rises from the mixing of a Lorentz boost, truncated at the appropriate order, with a gauge adjustment to keep the metric "simple," i.e. with vanishing off-diagonal spatial components and no Φ_5 dependence. Explicitly, the post-Galilean transformation from the rest frame coordinates $x^\alpha = (t, \mathbf{x})$ to the moving ones $\tilde{x}^\alpha = (\tau, \tilde{\mathbf{x}})$ reads:

$$\begin{aligned}
\mathbf{x} &= \tilde{\mathbf{x}} + \left(1 + \frac{1}{2}w^2\right)\mathbf{w}\tau + \frac{1}{2}(\tilde{\mathbf{x}}\cdot\mathbf{w})\mathbf{w} + \mathcal{O}(\tilde{\mathbf{x}}\epsilon^4 + \tau\epsilon^5)\,, \\
t &= \tau\left(1 + \frac{1}{2}w^2 + \frac{3}{8}w^4\right) + \left(1 + \frac{1}{2}w^2\right)\tilde{\mathbf{x}}\cdot\mathbf{w} + \\
&\quad + \underbrace{\frac{1}{2}(1 - \alpha_2 - \zeta_1 + 2\xi)w^k X_{,k}}_{\text{gauge change}} + \mathcal{O}(\tilde{\mathbf{x}}\epsilon^5 + \tau\epsilon^6)\,.
\end{aligned} \tag{1.34}$$

where the extra gauge freedom derived from the introduction of the additional post-Newtonian variable $\mathbf{w}$.

In the new coordinates, the metric becomes:

$$\tilde{g}_{00} = g_{00} + \Phi^{PF}\,, \tag{1.35a}$$

$$\tilde{g}_{0j} = g_{0j} + \Phi^{PF}_j\,, \tag{1.35b}$$

$$\tilde{g}_{jk} = g_{jk}\,, \tag{1.35c}$$

where the metric components on the right hand side are the ones of Eqs. (1.32) computed in the new coordinate system, and

$$\begin{aligned}
\Phi^{PF} &= (\alpha_3 - \alpha_1)w^2 U + (2\alpha_3 - \alpha_1)w^j V_j + \alpha_2 w^j w^k X_{,jk}\,, \\
\Phi^{PF}_j &= -\frac{1}{2}\alpha_1 w_j U + \alpha_2 w^k X_{,jk}\,.
\end{aligned} \tag{1.36}$$

As we may see, the α_i's are connected to *preferred-frame effects*. They are seen not to vanish only in *Vector-Tensor theories* and in *prior-geometric* ones, where the presence of vector/tensor gravitational fields in the former and the existence of an *absolute* gravitational field (such as a flat background metric) in the latter explicitly break local Lorentz Invariance.

The ζ_i parameters and α_3 are linked to the possibility of finding a conserved total momentum (not energy, which is already conserved at this level of approximation by Newtonian dynamics). It can be proved [42] that any metric theory with no *absolute elements* whose field equations can be derived from an invariant action principle has $\zeta_i = \alpha_3 = 0$ and consequently a conserved total momentum. Theories of gravity with these properties are called *semi-conservative*. Total angular momentum is conserved only if we have invariance under the aforesaid post-Galilean transformations (i.e. α_1 and α_2 vanish too) and these theories are called *fully-conservative*.

Finally, the ξ parameter is instead connected to the Whitehead potential Φ_W (first spotted in Whitehead theory of gravity) and it can appear also in GR if one uses gauges that are not diagonal in the spatial part of the metric.

1.5 Metric Theories of Gravity: an Overview

In this section, we briefly present some examples of Metric Theories of Gravity. The ppN formalism described in the previous section allows to compare and classify generic metric theories through the computation of their post-Newtonian limit and parameters. The general procedure is described in [76], Sec. 5.1. The method consists in solving by iteration the field equations of each theory at post-Newtonian order, imposing boundary cosmological conditions to the fields. The starting point of every generally covariant, Lagrangian-based, relativistic, universally coupled theory (i.e. a Metric Theory according to the theorem we quoted in Sec. 1.3.1) is an invariant action, from which we can derive field equations through a variational principle. At the end of this section, the ppN parameters for the cited theories are reported in Fig. 1.3, while the most updated experimental bounds for their values are reported in Fig. 1.4. In the following, we will not use geometrized units.

1.5.1 General Relativity

GR is undoubtedly the simplest metric theory we can think of. It is a *metric-only* theory with one gravitational field, the metric $\mathbf{g}$. If we neglect the cosmological constant (which brings effects only at cosmological scales), it has no arbitrary parameters. Field equations can be derived from an invariant action principle (as shown in Ch. 21 of [48]) $\delta I = 0$, where:

$$I = \frac{c^4}{16\pi G} \int R\sqrt{-g}\ \mathrm{d}^4x + I_m(\psi_m, g_{\mu\nu})\,, \tag{1.37}$$

where G is the experimentally measurable Newton coupling constant, $R = g^{\mu\nu}R_{\mu\nu}$ is the *Ricci Scalar Curvature* derived from *Ricci Tensor* $R_{\mu\nu}$, I_m is the non-gravitational action universally coupled with the metric and containing all the matter fields ψ_m.

The action was first proposed by the German mathematician *David Hilbert* in 1915. By varying the action with respect to $g_{\mu\nu}$, we obtain the field equations:

$$G^{\mu\nu} = \frac{8\pi G}{c^4} T^{\mu\nu}\,, \tag{1.38}$$

where $G^{\mu\nu} = R^{\mu\nu} - \frac{1}{2}g^{\mu\nu}R$ is the *Einstein tensor* and $T^{\mu\nu}$ is the energy-momentum tensor. As the Einstein tensor satisfies the Bianchi Identities $G^{\mu\nu}{}_{;\nu} = 0$, $T^{\mu\nu}{}_{;\nu} = 0$ holds and the energy-momentum tensor is conserved.

In a 1974 paper [42], Lee, Lightman and Ni showed that the conservation equation for $T^{\mu\nu}$ for a Lagrangian-based, generally covariant metric theory is a consequence of the gravitational field equations if and only if there are no *absolute variables*, i.e. *prior geometric* inputs, in the theory. This condition forces the ζ_i and α_3 parameters to vanish in the ppN framework, as stated in Sec. 1.4.4. This indeed is a necessary condition to build a conserved tensor $\Theta^{\mu\nu}$ (with $\Theta^{\mu\nu}{}_{;\nu} = 0$) that reduces to $T^{\mu\nu}$ in the absence of gravity.

GR ppN parameters can be computed by the post-Minkowskian approximation of the theory (see [56] for a pedagogical introduction). At the end of the computation, all parameters are seen to vanish with the exception of $\gamma = \beta = 1$. GR is then a *fully conservative* theory with no preferred-frame effects.

1.5.2 Scalar-Tensor Theories

Scalar-Tensor theories differ from General Relativity by the addition of a scalar gravitational field[3] ϕ, coupled to the metric tensor through an arbitrary function $w(\phi)$ and with a potential $V(\phi)$. Pioneered by Brans and Dicke in 1961 [15], they have regained attention in a more generalized version due to the rise of new cosmological theories of inflation. Their invariant action, written in what is called the *Jordan Frame*, is:

$$I = \frac{c^4}{16\pi G}\int\left[\phi R - \frac{w(\phi)}{\phi}g^{\mu\nu}\phi_{,\mu}\phi_{,\nu} - V(\phi)\right]\sqrt{-g}\ \mathrm{d}^4x + I_m(\psi_m, g_{\mu\nu})\,. \tag{1.39}$$

Varying the action with respect to $g_{\mu\nu}$ and ϕ, we can straightforwardly obtain the field equations:

$$G^{\mu\nu} = \frac{8\pi G}{\phi c^4}T^{\mu\nu} + \frac{w(\phi)}{\phi}\left(\phi_{,\mu}\phi_{,\nu} - \frac{1}{2}g_{\mu\nu}\phi_{,\beta}\phi^{,\beta}\right) + \frac{1}{\phi}(\phi_{;\mu\nu} - g_{\mu\nu}\Box_g\phi)\,, \tag{1.40}$$

$$\Box_g\phi = \frac{1}{3+2w(\phi)}\left(\frac{8\pi G}{c^4}T - \frac{\mathrm{d}w}{\mathrm{d}\phi}\phi_{,\beta}\phi^{,\beta} + \frac{\mathrm{d}}{\mathrm{d}\phi}(\phi^2 V)\right), \tag{1.41}$$

where $T = g_{\mu\nu}T^{\mu\nu}$ and $\Box_g = g^{\mu\nu}\nabla_\mu\nabla_\nu$ is the scalar d'Alambertian with respect to the metric.

Let ϕ_0 be the asymptotic value of the scalar field at present cosmological time and $w_0 \equiv w(\phi_0)$. If we develop the theory perturbatively, at first order in the Newtonian limit with $g_{\mu\nu} = \eta_{\mu\nu} + h_{\mu\nu}$ we obtain (in the $V(\phi) = 0$ approximation):

$$h_{00} = 2\frac{U}{c^2}\quad,\quad h_{0i} = h_{ij} = 0\quad\text{with}\quad \nabla^2 U = 8\pi G_{\text{eff}}\,, \tag{1.42}$$

where

$$G_{\text{eff}} = \frac{G}{\phi_0}\frac{4+2w_0}{3+2w_0}\,. \tag{1.43}$$

From Eq. (1.43), we see that the *empirical gravitational constant* G_{eff} (i.e. what experiments can measure) is no longer a constant, but a function of the present value of the scalar-field background ϕ_0 and therefore theoretically depends on time and location.

Among the first and simplest modifications of GR, there were $f(R)$ theories, whose invariant actions can be written as:

$$I = \frac{c^4}{16\pi G}\int f(R)\sqrt{-g}\ \mathrm{d}^4x + I_m(\psi_m, g_{\mu\nu})\,, \tag{1.44}$$

where $f(R)$ is a proper function of the Ricci scalar. $f(R)$ can be adjusted to make the universe experience an accelerated expansion without introducing Dark Matter or any Cosmological Constant. These theories are equivalent to Scalar-Tensor ones, as can be seen by replacing $f(R)$ with $f(\chi) - f_{,\chi}(\chi)(R-\chi)$, where χ is a dynamical scalar field. As long as $f_{,\chi\chi} \neq 0$, equation of motions for the χ field impose that $\chi = R$. We can then cast the action in the form of Eq. (1.39) by defining $\phi \equiv -f_{,\chi}(\chi)$ and setting $w(\phi) = 0$ and $\phi^2 V = \phi\chi(\phi) - f(\chi(\phi))$.

[3] We consider the case of a single additional scalar gravitational field for simplicity, but multiple ones are also admitted.

The computation of ppN parameters resembles the GR case, leading to all vanishing parameters with the exception of:

$$\gamma = \frac{1+w_0}{2+w_0}\,, \tag{1.45}$$

$$\beta = 1 + \frac{\phi_0 w_0'}{(3+2w_0)(4+2w_0)^2}\,. \tag{1.46}$$

In the original Brans-Dicke Theory, $w = w_{BD}$ is a constant and in the limit $w_{BD} \to \infty$ the theory is indistinguishable from GR, where $\gamma = \beta = 1$.

1.5.3 Vector-Tensor Theories

These theories contain two gravitational fields, the metric $\mathbf{g}$ and a dynamical, timelike, four-vector field u^μ. They depend on five different coupling constants ω, c_1, c_2, c_3, c_4, and a constraint parameter λ. The action can be generically written as:

$$I = \frac{c^4}{16\pi G}\int\left[(1+\omega u_\mu u^\mu)R - K^{\mu\nu}_{\alpha\beta}\nabla_\mu u^\alpha \nabla_\nu u^\beta + \lambda(u^\mu u_\mu + 1)\right]\sqrt{-g}\,\mathrm{d}^4x + I_m(\psi_m, g_{\mu\nu})\,, \tag{1.47}$$

where

$$K^{\mu\nu}_{\alpha\beta} = c_1 g^{\mu\nu}g_{\alpha\beta} + c_2\delta^\mu_\alpha\delta^\nu_\beta + c_3\delta^\nu_\alpha\delta^\mu_\beta - c_4 u^\mu u^\nu g_{\alpha\beta}\,. \tag{1.48}$$

We can divide this broad class of theories into two subsets:

- *constrained theories*, for which λ works as a Lagrangian multiplier, enforcing the normalization $u^\mu u_\mu = -1$. As a consequence, the ω term can be re-absorbed into the definition of G or, equivalently, set to zero;
- *unconstrained theories*, for which λ vanishes, ω is arbitrary, and the asymptotic value of the vector u^0 as another free parameter to be set.

Einstein-Æther Theory — Among constrained theories, particular relevance is held by the Einstein-Æther model, which is the most general parity-preserving but Lorentz-violating theory that includes up to (quadratic) first derivatives in the vector field. In some special cases, Lorentz symmetry breaking has been shown to be a mechanism for renormalization of gravity [70], which makes these theories particularly interesting to study. Einstein-Æther theories have a single 4-vector field, known as the "æther" and it is one of the possible constrained theories we described before. The theory was studied in its generality by Jacobson and collaborators [39, 44, 40, 29]. In [33], Foster and Jacobson computed the ppN parameters for this theory. Defining the following standard combination of c_i parameters

$$c_{14} \equiv c_1 + c_4\,, \quad c_{123} \equiv c_1 + c_2 + c_3\,, \quad c_\pm \equiv c_1 \pm c_3\,, \tag{1.49}$$

the ppN parameters for Einstein-Æther model are:

$$\begin{aligned}
&\gamma = \beta = 1\,, \quad \xi = \alpha_3 = \zeta_1 = \zeta_2 = \zeta_3 = \zeta_4 = 0\,,\\
&\alpha_1 = -\frac{8(c_3^2 + c_1 c_4)}{2c_1 - c_+ c_-}\,,\\
&\alpha_2 = \frac{1}{2}\alpha_1 - \frac{(2c_+ - c_{14})(c_+ + c_{14} + 3c_2)}{c_{123}(2 - c_{14})}\,.
\end{aligned} \tag{1.50}$$

One of the most interesting consequence of the model is that the gravitational constant $\mathcal{G}$ that enters Kepler's third law in a binary system is not the same as the constant G_N that enters Newton's third law in a Cavendish-type measurement. In turn, this is different from the bare constant G entering the Einstein-Æther action. Defining the *sensitivity* σ as:

$$\sigma = \left(\frac{2}{3}\alpha_2 - \alpha_1\right) C^*\,,$$

where C^* is the compactness of the body [32], we can write the following relations between the three gravitational constants:

$$G_N = G\left(1 - \frac{c_{14}}{2}\right)^{-1}\,, \quad \mathcal{G} = \frac{G_N}{(1+\sigma_A)(1+\sigma_B)}\,.$$

If we impose that gravitational-wave modes have real (not imaginary) frequencies and we require energy to be positive, we can constrain the values of the c_i parameters. Furthermore, imposing the condition $c_4 = -c_3^2/c_1$ and the condition that either $c_+ = 0$ or that $c_2 = c_+(c_3 - 2c_1)/3c_1$, we can reproduce GR ppN parameters, making $\alpha_1 = \alpha_2 = 0$ and reducing the free parameters of the model down to two (conventionally, $c_\pm$). For further details, see e.g. [79].

1.5.4 Other Kinds of Theories

Tensor-Vector-Scalar Theories — Modified Newtonian Dynamics (MOND) is a phenomenological mechanism proposed by Milgrom in [47] to explain flat rotation curves observed in spiral galaxies, without the assumption of hidden Dark Matter, but instead proposing a modified gravitational dynamic to take into account the anomalous behaviour of galaxy outer velocities. Three gravitational fields — the metric $\mathbf{g}$, a four-vector field u^μ and a scalar field ϕ — are necessary to reproduce MOND phenomenology in a fully relativistic theory of gravity, which is called indeed *Tensor-Vector-Scalar* (TeVeS) Theory. The only ppN parameters of this class of theories different from the ones of GR are α_1 and α_2, computed only in some particular cases. For further references, see [63].

Quadratic Gravity — Quadratic gravity theories rise from the idea of adding to the GR action terms that are quadratic in the Riemann tensor, Ricci tensor and Ricci scalar in order to reproduce an "effective field theory" model. They can contain parity-violating terms (proportional to $\tilde{R}R = \tilde{R}^{\alpha}{}_{\beta}{}^{\gamma\delta} R^{\beta}{}_{\alpha\gamma\delta}$, where $\tilde{R}^{\alpha}{}_{\beta}{}^{\gamma\delta} \equiv 1/2\varepsilon^{\gamma\delta\rho\sigma} R^{\alpha}{}_{\beta\rho\sigma}$)

and a scalar field ϕ. *Chern-Simons gravity* is one of the simplest among these theories. It contains only the parity-violating term $\tilde{R}R$ besides the scalar field. It can emerge in string theory as well as in loop quantum gravity to contribute to anomaly cancellation. For details, we refer to [11]. Other theories in this class have an action proportional to the Gauss-Bonnet invariant of the manifold, $R^2 - 4R_{\alpha\beta}R^{\alpha\beta} + R_{\alpha\beta\gamma\delta}R^{\alpha\beta\gamma\delta}$, and for this reason they are called *Einstein-Dilaton-Gauss-Bonnet*.

Massive Gravity — These theories emerge from attempts to provide the *graviton* with mass, although within a completely classical framework. This is equivalent to the addition of three helicity states to the propagation of gravitational fields, bringing problems of continuity with GR. These problems can be avoided only by carefully introducing non trivial elements or mechanisms in the theory, such as non-dynamical flat-background metric or screening effects. For a thorough reference, see [21].

Theory	Arbitrary functions or constants	Cosmic matching parameters	PPN parameters				
			γ	β	ξ	α_1	α_2
General relativity	none	none	1	1	0	0	0
Scalar–tensor							
Brans–Dicke	$\omega_{\rm BD}$	ϕ_0	$\frac{1+\omega_{\rm BD}}{2+\omega_{\rm BD}}$	1	0	0	0
General, $f(R)$	$A(\varphi)$, $V(\varphi)$	φ_0	$\frac{1+\omega}{2+\omega}$	$1+\frac{\lambda}{4+2\omega}$	0	0	0
Vector–tensor							
Unconstrained	$\omega, c_1, c_2, c_3, c_4$	u	γ'	β'	0	α_1'	α_2'
Einstein-Æther	c_1, c_2, c_3, c_4	none	1	1	0	α_1'	α_2'
Khronometric	$\alpha_k, \beta_k, \lambda_k$	none	1	1	0	α_1'	α_2'
Tensor–Vector–Scalar	k, c_1, c_2, c_3, c_4	ϕ_0	1	1	0	α_1'	α_2'

Figure 1.3. *ppN parameters values for some semi-conservative metric theories* ($\alpha_3 = \zeta_i = 0$). Primed values denote complicated functions of the arbitrary constants and matching parameters for each theory. (Reproduced from [75].)

Parameter	Effect	Limit	Remarks
$\gamma - 1$	time delay	2.3×10^{-5}	Cassini tracking
	light deflection	2×10^{-4}	VLBI
$\beta - 1$	perihelion shift	8×10^{-5}	$J_{2\odot} = (2.2 \pm 0.1) \times 10^{-7}$
	Nordtvedt effect	2.3×10^{-4}	$\eta_{\rm N} = 4\beta - \gamma - 3$ assumed
ξ	spin precession	4×10^{-9}	millisecond pulsars
α_1	orbital polarization	10^{-4}	Lunar laser ranging
		4×10^{-5}	PSR J1738+0333
α_2	spin precession	2×10^{-9}	millisecond pulsars
α_3	pulsar acceleration	4×10^{-20}	pulsar $\dot{P}$ statistics
ζ_1	—	2×10^{-2}	combined PPN bounds
ζ_2	binary acceleration	4×10^{-5}	$\ddot{P}_{\rm p}$ for PSR 1913+16
ζ_3	Newton's 3rd law	10^{-8}	lunar acceleration

Figure 1.4. *Current ppN parameters experimental bounds.* For the majority of theories, ζ_4 is not available independently from the other parameters, therefore it is not listed. (Reproduced from [75].)

Chapter 2

Gravitational-Wave Radiation in Metric Theories of Gravity

This chapter briefly reviews the theoretical foundations of the phenomenon of Gravitational Radiation in a generic Metric Theory of Gravity. The approach to solve wave equations in GR is shown to remain valid, with little modifications, in other theories of gravity. The speed of gravitational waves in some of the theories quoted in the first chapter is computed. In the last section, gravitational-wave polarization modes are studied in detail, providing the essential toolkit to analyze detector responses to them.

2.1 Wave Solutions in General Relativity

In this first section, after a brief overview on the long-lasting debate about the existence of gravitational waves, we will focus on the phenomenon of gravitational radiation in GR. We will develop an alternative formalism for GR, mainly due to the Russian theorists *Lev Davidovič Landau (1908-1968)* and *Evgenii Mikhailovich Lifshitz (1915-1985)*, to efficiently find wave equations of the theory, without any approximation. Then, the *DIRE (Direct Integration of Relaxed Einstein Equation) approach* to compute gravitational waveforms by subsequent iterations will be illustrated in some detail. Finally, the well-known result of the *quadrupole formula* will be derived from the machinery introduced, leading to a rough estimate of the gravitational-wave amplitude.

2.1.1 A Century Long Debate

At first sight, the presence of wave solutions to the Einstein field equations in GR could seem quite surprising. Geodesic motion indeed does not produce any form of wave. However, the possibility that small perturbations of the metric can propagate throughout spacetime was already deduced by Albert Einstein himself. By addressing the problem of the motion of a rotating dumbbell, held together by non-gravitational forces, in a couple of papers in 1916-1918 [26, 27], Einstein discovered that such dynamical system would radiate energy through metric waves, the leading term of which was found to be proportional to the second time derivative of the *quadrupole moment* of the source. Although the calculation was straightforward, the magnitude of the predicted waves was so small that Einstein himself thought they could have never been detected. For decades, some physicists even cast doubts upon the reality of these gravitational waves (GWs), considering them as artefact of general covariance.

In the 60s there were the first serious attempts to experimentally detect GWs with resonant bar detectors, pioneered by Joseph Weber. However, the sensitivity of the apparatus was not enough to reveal any feasible sources of GWs. In 1979, observations of the decay rate of the orbit of a binary pulsar system were shown to be in agreement with the *quadrupole formula* [65]. This led Hulse and Taylor to be awareded with the 1993 Nobel Prize in Physics. However, in 1976, Ehlers et al. [25] moved serious criticism toward the solution of the mathematical problem of radiation emitted by self-gravitating bodies, because of the use of techniques from classical electrodynamics to solve the field equations which involved ill-defined integrals. By 1990, all these computational problems were solved. Meanwhile, the proposals of large-scale interferometric gravitational-wave detectors began to build consensus, making the inspiral and coalescence of binary compact objects (such as black holes or neutron stars) a promising candidate source for detectable waves.

Every doubt on the reality and detectability of GWs was definitely clarified on September 14, 2015, when the first direct detection of GWs emitted by the coalescence of two black holes was seen by the LIGO interferometers, in USA [6]. Among the subsequent detections achieved by the LIGO-Virgo Collaboration [4] is

the first neutron star binary coalescence in 2017 [3]. This sparked the flourishing of a new branch of Observational Astronomy, called Multi-Messenger [7], which provides a new way of testing GR in high field regimes [2]. We are just at the dawn of a new era that will surely bring precious insights to our comprehension of the Universe.

2.1.2 Einstein's Equations in *Relaxed* Form

To provide an efficient calculation method for GWs, it is convenient to rewrite the Einstein field equations (1.38) using a different formalism, first developed by Landau and Lifshitz in their influential book *The Classical Theory of Fields* [41]. In the remainder of this section, we will not use geometrized units.

We start with the definition of the key object of Landau-Lifshitz framework, the *gothic inverse metric* $\mathfrak{g}^{\alpha\beta}$:

$$\mathfrak{g}^{\alpha\beta} \coloneqq \sqrt{-g} g^{\alpha\beta} \,, \tag{2.1}$$

where $g^{\alpha\beta}$ is the inverse metric and $g = \det(g_{\mu\nu})$. The inverse gothic metric as defined in Eq. (2.1) is not a tensor, but a *tensor density*. From $\mathfrak{g}^{\alpha\beta}$, we can build $H^{\alpha\mu\beta\nu}$, another tensor density with the same symmetries of the Riemann tensor:

$$H^{\alpha\mu\beta\nu} \coloneqq \mathfrak{g}^{\alpha\beta}\mathfrak{g}^{\mu\nu} - \mathfrak{g}^{\alpha\nu}\mathfrak{g}^{\beta\mu} \,. \tag{2.2}$$

It can be shown that

$$\frac{1}{2(-g)} \partial_{\alpha\beta} H^{\alpha\mu\beta\nu} = G^{\mu\nu} + \frac{8\pi G}{c^4} t^{\mu\nu}_{LL} \,, \tag{2.3}$$

where $t^{\mu\nu}_{LL}$ is known as *Landau-Lifshitz pseudotensor*. This object may be explicitly written as a quadratic combination of Christoffel Symbols:

$$\begin{aligned} t^{\mu\nu}_{LL} = \frac{c^4}{16\pi G} \{ & (2\Gamma^\sigma_{\alpha\beta}\Gamma^\rho_{\sigma\rho} - \Gamma^\sigma_{\alpha\rho}\Gamma^\rho_{\beta\sigma} - \Gamma^\sigma_{\alpha\sigma}\Gamma^\rho_{\beta\rho})(g^{\mu\alpha}g^{\nu\beta} - g^{\mu\nu}g^{\alpha\beta}) + \\ & + g^{\mu\alpha}g^{\beta\sigma}(\Gamma^\nu_{\alpha\rho}\Gamma^\rho_{\beta\sigma} + \Gamma^\nu_{\beta\sigma}\Gamma^\rho_{\alpha\rho} - \Gamma^\nu_{\sigma\rho}\Gamma^\rho_{\alpha\beta} - \Gamma^\nu_{\alpha\beta}\Gamma^\rho_{\sigma\rho}) + \\ & + g^{\nu\alpha}g^{\beta\sigma}(\Gamma^\mu_{\alpha\rho}\Gamma^\rho_{\beta\sigma} + \Gamma^\mu_{\beta\sigma}\Gamma^\rho_{\alpha\rho} - \Gamma^\mu_{\sigma\rho}\Gamma^\rho_{\alpha\beta} - \Gamma^\mu_{\alpha\beta}\Gamma^\rho_{\sigma\rho}) + \\ & + g^{\alpha\beta}g^{\sigma\rho}(\Gamma^\mu_{\alpha\sigma}\Gamma^\nu_{\beta\rho} - \Gamma^\mu_{\alpha\beta}\Gamma^\nu_{\sigma\rho}) \} \,. \end{aligned} \tag{2.4}$$

To gain insight on the physical relevance and meaning of the object we just defined, we can substitute the Einstein tensor $G^{\mu\nu}$ using Einstein's field equations (1.38) in Eq. (2.3), finding:

$$\frac{1}{2(-g)} \partial_{\alpha\beta} H^{\alpha\mu\beta\nu} = \frac{8\pi G}{c^4} (T^{\mu\nu} + t^{\mu\nu}_{LL}) \,. \tag{2.5}$$

This expression provides a non-tensorial form of Einstein's field equations. Further, using $H^{\alpha\mu\beta\nu}$'s anti-symmetry, from the identity

$$\partial_{\nu\alpha\beta} H^{\alpha\mu\beta\nu} = 0 \,, \tag{2.6}$$

we can write the following *conservation law*:

$$\partial_\nu \Big[(-g)(T^{\mu\nu} + t^{\mu\nu}_{LL}) \Big] = 0 \,. \tag{2.7}$$

In the context of GR, this equation is equivalent to the usual expression of energy-momentum conservation $T^{\mu\nu}{}_{;\nu} = 0$ and suggests that we can interpret the *Landau-Lifshitz pseudo-tensor* as the entity that contains the information of the energy and the momentum carried by the gravitational field. Since in the local inertial frame in which gravity is suppressed Christoffel Symbols are seen to vanish, $t^{\mu\nu}_{LL}$ cannot be a tensor (it would have to vanish in every reference frame) and its numerical value is coordinate-dependent.

Now, we can use the residual gauge freedom to impose the *harmonic gauge condition* $\partial_\beta \mathfrak{g}^{\alpha\beta} = 0$. Introducing the potentials

$$h^{\alpha\beta} \coloneqq \eta^{\alpha\beta} - \mathfrak{g}^{\alpha\beta}\,, \tag{2.8}$$

we can rewrite the field equations in the so-called *relaxed form*:

$$\Box h^{\alpha\beta} = -\frac{16\pi G}{c^4}\tau^{\alpha\beta}\,, \tag{2.9}$$

where

$$\tau^{\alpha\beta} \coloneqq (-g)(T^{\alpha\beta}[m,g] + t^{\alpha\beta}_{LL}[h] + t^{\alpha\beta}_{H}[h])\,, \tag{2.10}$$

$$t^{\alpha\beta}_{H}[h] \coloneqq \frac{c^4}{16\pi G(-g)}(\partial_\mu h^{\alpha\nu}\partial_\nu h^{\beta\mu} - h^{\mu\nu}\partial_{\mu\nu}h^{\alpha\beta})\,. \tag{2.11}$$

t_H is an additional (harmonic-gauge) contribution to the effective energy-momentum pseudotensor while the box operator is the d'Alambertian in flat spacetime. In formulae:

$$\Box \coloneqq \eta_{\mu\nu}\partial^{\mu\nu} = -\frac{1}{v^2}\frac{\partial^2}{\partial t^2} + \nabla^2\,, \tag{2.12}$$

v being the wave propagation speed in the theory. In GR, $v = c$. Enforcing the *harmonic gauge condition* is equivalent to imposing the conservation statement:

$$\partial_\beta \tau^{\alpha\beta} = 0\,. \tag{2.13}$$

Equations (2.9) and (2.13) together represent an exact reformulation of Einstein's field equations: up to now, no approximation was performed. Furthermore, Eq. (2.9) is a *wave equation* in "flat spacetime:" each component of the potential $h^{\alpha\beta}$ has a wave solution with $\tau^{\alpha\beta}$ acting as the source. To underline the high non-linearity of the wave equation, we have indicated explicitly in square brackets the dependency on the source (generically denotes as m) and on the gravitational field of each term. One of the possible procedures to compute the gravitational waveform involves solving iteratively the relaxed equation and is known as DIRE, *Direct Integration of Relaxed Einstein Equation*. The approach was elaborated by Will, Wiseman and Pati in [78, 52, 53] and it will be sketched in the next subsection.

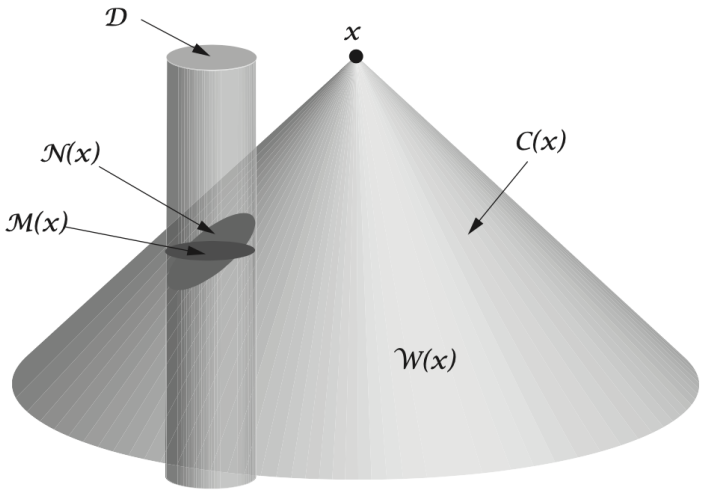

Figure 2.1. *The near-zone and the wave-zone domain.* Integration domains for the retarded solution of the wave equation with the field point in the wave zone: $\mathcal{C}(x)$ is the past "null" cone (with speed v) of the field point x; $\mathcal{D}$ is the world tube of the near zone of radius $\mathcal{R}$; $\mathcal{N}(x)$ is the intersection of $\mathcal{D}$ with $\mathcal{C}(x)$ and $\mathcal{W}(x)$ is the rest of the null cone; $\mathcal{M}(x)$ is a constant retarded-time hypersurface used for calculating multipole moments. (Reproduced from [76].)

2.1.3 The DIRE Approach for Solving the Relaxed Field Equations

The formal solution of Eq. (2.9) is given (using the retarded Green's function technique) by:

$$h^{\alpha\beta}(t,\mathbf{x}) = \frac{4G}{c^4}\int_{\mathcal{C}(x)} \frac{\tau^{\alpha\beta}(t-|\mathbf{x}-\mathbf{x}'|/v,\mathbf{x}')}{|\mathbf{x}-\mathbf{x}'|}\mathrm{d}^3x' \,, \tag{2.14}$$

where the integral is computed over $\mathcal{C}(x)$, the flat-spacetime *past null cone* (with speed v) of the field point $x=(t,\mathbf{x})$, and $|\mathbf{x}-\mathbf{x}'|$ is the Euclidean distance between the field point $\mathbf{x}$ and the source point $\mathbf{x}'$. We can split the integration domain into two different parts: the *near-zone domain* $\mathcal{N}(x)$ and the *wave-zone domain* $\mathcal{W}(x)$.

If we consider t_c to be the characteristic time scale of the source, we can define $\lambda_c = vt_c$ to be the characteristic wavelength of the source. We choose the boundary between the near and the wave zone at selected radius $\mathcal{R}$ from the source, taking $\mathcal{R}$ of the same order of magnitude as λ_c. This three-dimensional sphere of radius $\mathcal{R}$ identifies a world tube $\mathcal{D}$, whose intersection with $\mathcal{C}(x)$ determines $\mathcal{N}(x)$, as illustrated in Fig. 2.1. We can then write the solution $h^{\alpha\beta}(x)$ as the sum of two contributions depending on the domain chosen:

$$h^{\alpha\beta}(x) = h^{\alpha\beta}_{\mathcal{N}}(x) + h^{\alpha\beta}_{\mathcal{W}}(x)\,. \tag{2.15}$$

Although $h_{\mathcal{N}}$ and $h_{\mathcal{W}}$ will individually depend on $\mathcal{R}$, their sum (i.e. the total solution) will be $\mathcal{R}$-independent, as explicitly shown in [52].

A feasible way to solve the integral in Eq. (2.14) is to proceed by iteration, under the assumption of a *weak-field regime* ($\|h^{\alpha\beta}\| \ll 1$) and within a *slow-motion approximation*. The latter condition imposes that the characteristic velocity within the source v_c is much smaller than the speed of light ($v_c \ll c$) in order to keep the piece of the source function with compact support μ_c (usually the matter energy-momentum tensor) deep within the near zone ($v_c t_c = r_c \ll \lambda_c$). Notice that these two assumptions were already made in the definition of *post-Newtonian regime* in Sec. 1.4.

The *first iteration* consists in setting $h_0^{\alpha\beta} = 0$ in the right-hand side and solving the *relaxed* equation (2.9) for $h_1^{\alpha\beta}$, using the Minkowskian energy-momentum tensor $T^{\alpha\beta}[m, \eta]$. The equations of motion are not known, but the solution is found to be dependent on the matter variables m. From the solution $h_1^{\alpha\beta}$, we can form the inverse metric $g_1^{\alpha\beta}$ and we can construct an improved version of the effective energy-momentum pseudotensor:

$$\tau_0^{\alpha\beta} = (-g)(T^{\alpha\beta}[m, g_1] + t_{LL}^{\alpha\beta}[h_1] + t_H^{\alpha\beta}[h_1]) \,.$$

The *n-th iteration* is simply obtained (at least in principle) by the $(n-1)$-th pseudotensor, solving the relaxed field equation again for $h_n^{\alpha\beta}$. To find the equations of motion for the source at the n-th iteration, we can enforce the gauge condition $\partial_\beta \tau_n^{\alpha\beta} = 0$ on the effective pseudotensor computed at the corresponding order. Notice that to avoid contradictions, the enforcing of the gauge condition/conservation statement must be delayed at the very last step of the iterative process.

At fixed iteration order, the formal integral in Eq. (2.14) must be handled differently, according to the proximity of the field position x to the near zone. If we want to compute the waveform, the solution must be evaluated for points in the *far wave zone*, for which the only significant contributions to the integral comes from $1/R$ terms, where $R = |\mathbf{x} - \mathbf{x}'|$ is the distance from the source. Considering first the contributions given by the near-zone domain $h_{\mathcal{N}}^{\alpha\beta}(x)$, we can expand the integral in the following way:

$$h_{\mathcal{N}}^{\alpha\beta}(x)\big|_{\text{wave}} = \frac{4G}{Rc^4} \int_{\mathcal{N}} \tau^{\alpha\beta}\left(t - \frac{R}{v} + \frac{\mathbf{N}\cdot\mathbf{x}'}{v}, \mathbf{x}'\right) \mathrm{d}^3x' + \mathcal{O}\left(\frac{1}{R^2}\right), \tag{2.16}$$

where $\mathbf{N} \equiv \mathbf{x}/R$ and the subscript $\big|_{\text{wave}}$ stands for the fact that the solution is evaluated for far field points, with $|\mathbf{x} - \mathbf{x}'| \gg \mathcal{R}$. Within the approximations previously described, we can further develop the potential $h_{\mathcal{N}}^{\alpha\beta}(x)$ performing a *multipole expansion* in which each ℓ-pole moment of the source is differentiated ℓ times with respect to t:

$$h_{\mathcal{N}}^{\alpha\beta}(x)\big|_{\text{wave}} = \frac{4G}{Rc^4} \sum_{\ell=0}^{\infty} \frac{1}{\ell! v^\ell} \left(\frac{\partial}{\partial t}\right)^\ell \int_{\mathcal{M}} \tau^{\alpha\beta}\left(t - \frac{R}{v}, \mathbf{x}'\right) (\mathbf{N}\cdot\mathbf{x}')^\ell \mathrm{d}^3x' + \mathcal{O}\left(\frac{1}{R^2}\right). \tag{2.17}$$

Notice that we have changed the domain of integration into $\mathcal{M}$ since the temporal dependence of the source function no longer involves the integration variable $\mathbf{x}'$ making the new integration domain a surface of constant time (the constant equal to the retarded time $\tau = r - R/v$, see Fig. 2.1). Furthermore, there is an interesting

property that links time and space derivatives of the solution. Indeed, by inspection, it can be shown that:

$$\nabla h^{\alpha\beta}_{\mathcal{N}}(x)\big|_{\text{wave}} = -\mathbf{N}\frac{1}{v}\partial_t h^{\alpha\beta}_{\mathcal{N}}(x)\big|_{\text{wave}} + \mathcal{O}\left(\frac{1}{R^2}\right). \tag{2.18}$$

Since the approximations we have made are compatible with the *post-Newtonian* (PN) limit of the metric theory, to preserve consistency we ought to choose a specific PN order and solve each iteration with corrections at the corresponding order. As a result, the solution will be computed at nPN order, where $v_c \sim 0.5$PN[1]. In the *far wave zone*, to complete the solution we should add to Eq. (2.17) the result of the integral carried over the rest of the "null" cone, $h^{\alpha\beta}_{\mathcal{W}}(x)$. However, depending on the metric theory chosen, its contributions can be negligible at first PN order. In GR, it can be proved that $h^{\alpha\beta}_{\mathcal{W}}(x)$ contributions (known as *gravitational-wave tails*) occur at 1.5PN order at least.

To evaluate the multipole moments in Eq. (2.17), a PN description of the source is needed. We can obtain this from the near-zone solution for the field, carrying out a similar expansion of the integral, this time with $|\mathbf{x}-\mathbf{x}'| \ll \mathcal{R}$ (as indicated by the subscript $\big|_{\text{near}}$). Concerning the near-zone domain contribution to the integral, we have:

$$h^{\alpha\beta}_{\mathcal{N}}(x)\big|_{\text{near}} = \frac{4G}{c^4}\sum_{\ell=0}^{\infty}\frac{(-1)^\ell}{\ell! v^\ell}\left(\frac{\partial}{\partial t}\right)^\ell \int_{\mathcal{M}} \tau^{\alpha\beta}(t,\mathbf{x}')|\mathbf{x}-\mathbf{x}'|^{(\ell-1)}\mathrm{d}^3x' \,. \tag{2.19}$$

The first term is an instantaneous Poisson potential with source $\tau^{\alpha\beta}$, while the following terms are of $\ell \times 0.5$PN order, being $\partial_t \sim v_c/r_c \sim 0.5$PN. This last relation, valid for every multipole expansion, can also be used to count the order of each PN term in Eq. (2.17). The outer integral $h^{\alpha\beta}_{\mathcal{W}}(x)$ generally gives contributions only at very high PN orders (in GR, starting from 4PN) and it may be safely neglected.

2.1.4 The TT-Gauge and the Quadrupole Formula

We now apply the computational technique of the previous subsection to GR, where $v = c$. First of all, it is interesting to study how many independent components the $h^{\alpha\beta}$ potential has in the *far wave zone*. Its symmetric nature is inherited from the metric itself, so we are left with ten degrees of freedom. However, invariance under coordinate transformations (or *gauge transformation*, as they are called if they involve the $h^{\alpha\beta}$ potentials) allows us to reduce the degrees of freedom to six. A general proof of this fact, valid in any metric theory of gravity, will be provided in Sec. 2.3.1. For the moment, we can explicitly show this property within GR noticing that, given the definition of $h^{\alpha\beta}$ in Eq. (2.8), the harmonic gauge condition $\partial_\beta \mathfrak{g}^{\alpha\beta} = 0$ implies:

$$\partial_\beta h^{\alpha\beta} = 0 \quad \Rightarrow \quad \partial_j h^{\alpha j} = -c^{-1}\partial_t h^{\alpha 0} \,.$$

[1] Notice that the convention used in this context differs from the one adopted in Sec. 1.4, where $v_c \sim 1$PN.

This property combined with the result in Eq. (2.18) allows us to rewrite — up to a constant factor — all the metric components as functions of the spatial part of the $h^{\alpha\beta}$ tensor, reducing (as expected from the previous considerations) the degrees of freedom of the perturbation down to six (the number of free components in a symmetric 3×3 tensor):

$$h^{0j}_{\mathcal{N}} = N_k h^{kj}_{\mathcal{N}} + \mathcal{O}\left(\frac{1}{R^2}\right),$$
$$h^{00}_{\mathcal{N}} = N_k N_j h^{kj}_{\mathcal{N}} + \mathcal{O}\left(\frac{1}{R^2}\right). \tag{2.20}$$

Within GR, it is possible to specialize the harmonic gauge even further. Under a gauge transformation generated by a four-vector field $\zeta^\alpha(x)$, the potentials $h^{\alpha\beta}$ will transform as:

$$h^{\alpha\beta} \to h^{\alpha\beta} - \partial^\alpha \zeta^\beta - \partial^\beta \zeta^\alpha + (\partial_\mu \zeta^\mu)\eta^{\alpha\beta}, \tag{2.21}$$

and, consequently,

$$\partial_\beta h^{\alpha\beta} \to \partial_\beta h^{\alpha\beta} - \Box \zeta^\alpha. \tag{2.22}$$

If we choose ζ^μ such that $\Box\zeta^\mu = 0$ to preserve the harmonic gauge condition, we can eliminate another four degrees of freedom, which leaves us with only two radiative modes. Decomposing the perturbation into irreducible pieces, it can be shown that the gauge invariant part of the metric is the transverse-traceless (TT) spatial part h^{jk}_{TT}, such that $N_j h^{jk}_{TT} = 0 = \delta_{jk} h^{jk}_{TT}$. The gravitational potentials in this particular form are said to be in the *transverse-traceless gauge*, or *TT gauge*, a specialization of the harmonic gauge that can be achieved in the *far wave zone*.

If we want to compute a waveform in GR, we have to solve the multipole expansion of Eq. (2.17) in the far wave zone. Two iterations are required to obtain 1PN equations of motion or the gravitational waveform for a binary system. The first iteration is found by substituting $h^{jk}_0 = 0$ into the source term τ^{jk} and solving the relaxed equation for h^{jk}_1. The source term would receive a contribution only from the special relativistic limit of the energy-momentum tensor $T^{jk}_0 \sim \rho^* v^j v^k$ as defined in Eq. (1.17) (where v is the 3-velocity of the fluid/system). Stopping at the first iteration would have meant imposing the gauge condition directly on the energy-momentum tensor, leading to the Minkowskian conservation law $T^{\alpha\beta}{}_{,\beta} = 0$ which implies a flat spacetime with no gravitational interaction at all. Further, contributions from the Landau-Lifshitz pseudotensor $\tau^{\alpha\beta}_{LL}$ are at the *same* order as the purely kinetic terms T^{jk}_0 and must be taken into account for a consistent analysis. The Newtonian dynamics is indeed recovered at the second iteration of the procedure.

We can use some properties of the source term to avoid explicitly calculating the two iterations. As a consequence of the gauge condition $\partial_\beta \tau^{\alpha\beta} = 0$, we can show that, taking $\tau^{\alpha\beta}$ to be symmetric, which is always possible in fully-conservative theories such as GR:

$$\tau^{jk} = \frac{1}{2}(\tau^{00} x^j x^k)_{,00} + \left(\tau^{pj} x^k + \tau^{pk} x^j\right)_{,p} - \frac{1}{2}(\tau^{pq} x^j x^k)_{,pq}. \tag{2.23}$$

At the lowest multipole order in Eq. (2.17), we have:

$$h^{jk}_{\mathcal{N}} = \frac{4G}{Rc^4}\int_{\mathcal{M}} \tau^{jk}(t - R/c, \mathbf{x}')\mathrm{d}^3x' \,. \tag{2.24}$$

We can substitute the integrand in the previous equation with the right-hand side of Eq. (2.23), converting all the (spatial) divergence terms into surface integrals. Every $\mathcal{R}$-dependence must be dropped since it is cancelled from the opposite contribution in $h^{jk}_{\mathcal{W}}$. We are then left with the following relation:

$$h^{jk}_{\mathcal{N}} = \frac{2G}{Rc^4}\frac{\mathrm{d}^2}{\mathrm{d}t^2}\int_{\mathcal{M}} \tau^{00}(t - R/c, \mathbf{x}')x'^j x'^k \mathrm{d}^3x' \,. \tag{2.25}$$

At the lowest PN order $\tau^{00} = T^{00} = \rho^*$, and we finally obtain:

$$\begin{aligned} h^{jk}_{\mathcal{N}} &= \frac{2G}{Rc^4}\frac{\mathrm{d}^2}{\mathrm{d}t^2}\int_{\mathcal{M}} \rho^*(t - R/c, \mathbf{x}')x'^j x'^k \mathrm{d}^3x' \\ &= \frac{2G}{Rc^4}\ddot{I}^{jk} \,. \end{aligned} \tag{2.26}$$

where $\ddot{I}^{jk}$ is the second derivative in time of the *quadrupole moment* of the source. For a discrete set of bodies with masses m_i, this may be written classically as:

$$I^{jk} \equiv \sum_i m_i x_i^j x_i^k \,.$$

Equation (2.26) is the well known *quadrupole formula*, derived by Einstein in [27]. The fact that the result is the same whether the source is gravitationally bounded (a binary system) or not (Einstein's dumbbell) is a direct consequence of the Strong Equivalence Principle (SEP) described in Sec. 1.3.3. Finally, Eq. (2.26) can give us a rough estimate of the GW amplitude h_0. Given a mass M confined to a volume of radius r_c, being $v_c \sim r_c/t_c$ the characteristic velocity of the source, we can approximate $\ddot{I}^{jk} \sim Mr_c^2/t_c^2 = Mv_c^2$. Plugging in typical astrophysical parameters $M = 10M_\odot$ and $R = 1\mathrm{Mpc}$, we find:

$$h_0 \sim \frac{GM}{Rc^2}\left(\frac{v_c}{c}\right)^2 = 4.8 \times 10^{-19}\left(\frac{M}{M_\odot}\right)\left(\frac{1\mathrm{Mpc}}{R}\right)\left(\frac{v_c}{c}\right)^2 . \tag{2.27}$$

High speed phenomena produce the strongest waves. However, it is important to stress that v_c is the characteristic velocity of a source that *deviates from spherical symmetry*. Indeed, the only possible external solution to Einstein's equation for a spherical-symmetric system is necessarily static and given by the Schwarzschild metric. This statement is known as *Birkhoff's theorem*.

2.2 Wave Solutions in Metric Theories

In the previous section, we outlined a general procedure, the DIRE approach, to compute by subsequent iterations the predicted gravitational waveform from a *relaxed field equation* as Eq. (2.9). Throughout the calculation we did not use any specific GR property, keeping the propagation speed of the waves as a free

parameters of the theory. The same algorithm can be used to solve the wave problem in *any* metric theory of gravity, provided the field equations can be rewritten in a relaxed form. In the following, we will sketch the general procedure to find the waveform in a generic theories. Furthermore, specific examples of relaxed equations and their consequence on the propagation speed of the wave will be analyzed for some of the theories described in Sec. 1.5.

2.2.1 Waveform

Working in the universal rest frame, once we have chosen a specific theory for gravity and set the cosmological boundary conditions to agree with solar system experiments, it is sufficient to expand any gravitational fields (tensor, vector, scalar) about their asymptotic values:

$$\begin{aligned} g_{\mu\nu} &= g^{(0)}_{\mu\nu} + h_{\mu\nu}\,, \\ \phi &= \phi_0(1+\Psi)\,, \\ K^\mu &= (K + k^0, k^1, k^2, k^3)\,, \\ B_{\mu\nu} &= B^{(0)}_{\mu\nu} + b_{\mu\nu}\,. \end{aligned} \tag{2.28}$$

Then, using all available gauge freedom, we can express the field equations in a relaxed form, of the kind:

$$\Box\psi^A = -16\pi\tau^A\,, \tag{2.29}$$

where the $\Box$ operator is the one defined in Eq. (2.12). ψ^A is either one of the perturbation of the fields in Eq. (2.28), or a linear combination of them and τ^A is a source term involving the non-gravitational energy-momentum tensor as well as gravitational energy-momentum pseudo-tensors, quadratic in the fields.

A general result proved by Lee in [42] states that every Lagrangian-based metric theory admits a conserved pseudo-tensor $\tau^{\alpha\beta}$ such that:

$$\partial_\beta \tau^{\alpha\beta} = 0\,. \tag{2.30}$$

The pair of equations (2.29) and (2.30) is completely equivalent to the field equations for the theory as found using the variational principle (see Sec. 1.5). One can then bring all the computational machinery developed for GR in any alternative theory: first, the *relaxed* equation (2.29) can be solved formally as a function of the matter variables; then, Eq. (2.30) can be used to obtain the matter behaviour as a function of time to finally get the full solution for the fields of the theory.

2.2.2 Speed

As we saw in the previous subsection, obtaining a specific waveform for a given theory can be a lengthy procedure that involves a lot of computational power and mathematical subtleties. However, some properties of the waves in a generic metric theory can be predicted (and measured) without the full calculation of the waveform. Among them, the measurement of the propagation speed of GWs is

definitely one of the most stringent tests on GR that can be performed. The Einstein Equivalence Principle (Sec. 1.2) requires that in every frame the propagation speed of a *massless* non-gravitational field is c, the speed of light. However, it does not place any constraint on the speed of GWs that is ultimately determined by the detailed structure of the field equations.

To compute the expected speed of wave propagation in a generic metric theory of gravity, it is convenient to develop the formalism within the two following approximations:

- *Weak waves:* the perturbation amplitude $|h_{\mu\nu}|$ that characterize the wave is small with respect to the background metric $|g^{(B)}_{\mu\nu}|$, i.e.

$$\frac{|h_{\mu\nu}|}{|g^{(B)}_{\mu\nu}|} \ll 1 \,.$$

- *Short-wavelength:* the wavelength λ of the wave is small with respect to the radius of curvature of the background spacetime $\mathfrak{R}$, i.e.

$$\frac{\lambda}{\mathfrak{R}} \ll 1 \,,$$

  where $\mathfrak{R}$ can be thought of as the inverse square root of a typical component of the Riemann tensor as measured in a local Lorentz frame.

This regime is equivalent to the *geometrical optics limit* for an electromagnetic wave (see [48], Sec. 22.5 for further references). A simple method to the study GW propagation speed within the geometrical optics approximation is to solve the vacuum field equations of a specific metric theory, linearized about a background metric chosen to be locally Minkowskian. This is equivalent to studying GW propagation in a local Lorentz frame.

General Relativity — The vacuum linearized field equation in harmonic coordinates can be taken from Eq. (2.9), setting the right-hand side to zero:

$$\Box h^{\alpha\beta} = 0 \,. \tag{2.31}$$

This equation admits plane-wave solutions

$$h^{\alpha\beta} = \mathcal{A}^{\alpha\beta} e^{i\ell_\mu x^\mu} \,, \quad \eta_{\mu\nu}\ell^\mu\ell^\nu = 0 \,, \tag{2.32}$$

where $\mathcal{A}^{\alpha\beta}$ is a constant tensor amplitude and ℓ_μ is a constant wave-vector. From the second relation in Eq. (2.32), we see that the gravitational wave-vector is a null 4-vector in the local Lorentz frame: the electromagnetic and gravitational light cones coincide, i.e. GWs travel at the speed of light c.

Scalar-Tensor Theories — If we introduce a *conformal transformed* metric in the action in Eq. (1.39):

$$\tilde{g}_{\mu\nu} = \frac{\phi}{\phi_0} g_{\mu\nu} \,, \tag{2.33}$$

we can express Scalar-Tensor theories in a Landau-Lifshitz formalism analogous to the one developed in Sec. 2.1.2. If we define

$$\tilde{\mathfrak{g}}^{\alpha\beta} \equiv \sqrt{-\tilde{g}}\tilde{g}^{\alpha\beta} \,, \tag{2.34}$$

$$\tilde{h}^{\alpha\beta} \equiv \eta^{\alpha\beta} - \tilde{\mathfrak{g}}^{\alpha\beta} \,, \tag{2.35}$$

imposing the harmonic-gauge condition

$$\partial_\beta \tilde{h}^{\alpha\beta} = 0 \,,$$

we can rewrite the two field equations (1.40) and (1.41) (setting $c = 1$) as

$$\Box \tilde{h}^{\alpha\beta} = -16\pi\tilde{G}(-\tilde{g})(\tilde{T}^{\alpha\beta} + \tilde{t}^{\alpha\beta}_{\phi} + \tilde{t}^{\alpha\beta}_{LL} + \tilde{t}^{\alpha\beta}_{H}) \,, \tag{2.36}$$

$$\Box \phi = -8\pi\tilde{G}\tau^s \,, \tag{2.37}$$

where

$$(-\tilde{g})\tilde{t}^{\alpha\beta}_{\phi} = \frac{1}{16\pi\tilde{G}}\left[\frac{3+2w}{\phi^2}\left(\tilde{g}^{\alpha\mu}\tilde{g}^{\beta\nu} - \frac{1}{2}\tilde{g}^{\alpha\beta}\tilde{g}^{\mu\nu}\right)\phi_{,\mu}\phi_{,\nu} - \tilde{V}(\phi)\tilde{g}^{\alpha\beta}\right] , \tag{2.38}$$

$$\begin{aligned}\tau^s = &-\sqrt{-\tilde{g}}\frac{\phi}{3+2w}\left(\tilde{T} + \frac{\phi}{8\pi\tilde{G}}\frac{\mathrm{d}\tilde{V}}{\mathrm{d}\phi}\right) \\ &+ \frac{1}{16\pi\tilde{G}}\left\{\frac{\mathrm{d}}{\mathrm{d}\phi}\left[\ln\left(\frac{3+2w}{\phi^2}\right)\right]\tilde{\mathfrak{g}}^{\mu\nu}\phi_{,\mu}\phi_{,\nu} - 2\tilde{h}^{\mu\nu}\phi_{,\mu\nu}\right\} ,\end{aligned} \tag{2.39}$$

$\tilde{G} = G/\phi_0$, $\tilde{V}(\phi) = \phi_0 V(\phi)/\phi^2$, $\tilde{T}^{\alpha\beta} = (\phi_0/\phi)^3 T^{\alpha\beta}$, $\tilde{t}^{\alpha\beta}_{LL}$ and $\tilde{t}^{\alpha\beta}_{H}$ being the Landau-Lifshitz and harmonic pseudo-tensor as defined in Eqs. (2.4) and (2.11), but computed as functions of $\tilde{h}^{\alpha\beta}$.

Vacuum solutions in the linearized theory are easily found setting both source terms in Eqs. (2.36) and (2.37) to zero. For $\tilde{V}(\phi) = 0$ and expanding ϕ around its asymptotic value ϕ_0 as $\phi = (1 + \Psi)\phi_0$, we find:

$$\tilde{h}^{\alpha\beta} = \mathcal{A}^{\alpha\beta} e^{i\ell_\mu x^\mu} \quad , \quad \eta_{\mu\nu}\ell^\mu\ell^\nu = 0 \,, \tag{2.40}$$

$$\Psi = \mathcal{B} e^{i\ell'_\mu x^\mu} \quad , \quad \eta_{\mu\nu}\ell'^\mu\ell'^\nu = 0 \,, \tag{2.41}$$

where ℓ_μ and ℓ'_μ are two different wave vectors for the tensor and scalar wave respectively, both null. If we were to take $\tilde{V}(\phi) \sim m^2\phi^2$, providing the scalar field with a mass, we would obtain a *massive propagation relation* for the scalar field with a propagation speed of the correspondent wave lower than c, while the $\tilde{h}^{\alpha\beta}$ waves are still null.

Mode	v_g^2 and small c_i limit	$E(2)$ class
Pure metric	$\frac{1}{1-c_{13}} \to 1$	N_2
Transverse vector	$\frac{2c_1-c_1^2+c_3^2}{2c_{14}(1-c_{13})} \to \frac{c_1}{c_{14}}$	III_5
Longitudinal vector	$\frac{c_{123}}{c_{14}} \frac{2-c_{14}}{2(1+c_2)^2-c_{123}(1+c_2+c_{123})} \to \frac{c_{123}}{c_{14}}$	II_6

Figure 2.2. *Gravitational-wave speeds and polarization modes in Einstein-Æther theory.* For each propagating degree of freedom of the Einstein-Æther theory, the propagation speed squared v_g^2 and its limit for small c_i parameters are shown. The $E(2)$ classification of the polarization modes will be explained in Sec. 2.3.2 in some detail. (Reproduced from [76].)

Einstein-Æther Theory — Einstein-Æther theory has five propagating degrees of freedom. The two pure-metric waves, analogous to GR ones, with speed $(1-c_+)^{-1/2}$ are completely decoupled from the vector field. The remaining two transverse and one longitudinal æther-metric modes have speeds that depend on complicate functions of the c-parameters.

An elegant and straightforward method to obtain them can be found in [35]: it derives the linearized equations of motion around the flat spacetime background using the gauge invariant variables of the theory to easily separate physical degrees of freedom. This technique is used in Sec. 2.3.1 to identify the possible polarization modes of a GW within the metric tensor and it can be extended to the other gravitational fields of the theory.

For sake of completeness, in Fig. 2.2 speeds and polarization modes of Einstein-Æther waves are reported.

Massive Gravity — Massive gravity theories introduce a mass m_g for the "graviton," i.e. a massive vacuum equation for the linearized metric $h^{\alpha\beta}$ of the kind:

$$\Box h^{\alpha\beta} - \left(\frac{m_g}{\hbar}\right)^2 h^{\alpha\beta} = 0\,, \tag{2.42}$$

where $\hbar = h/2\pi$ is the *reduced Planck constant*. Substituting the plane-wave solution as in Eq. (2.32), we obtain for the ℓ_μ wave vector the following equation:

$$\eta_{\mu\nu}\ell^\mu\ell^\nu = -\left(\frac{m_g}{\hbar}\right)^2. \tag{2.43}$$

If we consider $\ell^0 = \omega$ and $\ell^i = k^i$, we find the dispersion relation:

$$\omega^2 - |\mathbf{k}|^2 = \left(\frac{m_g}{\hbar}\right)^2, \tag{2.44}$$

where $k = |\mathbf{k}|^2 = k^i k_i$. From Eq. (2.44), it is straightforward to derive the speed of propagation of the wave, in units of c:

$$v \equiv \frac{\mathrm{d}\omega}{\mathrm{d}k} = \left(1 - \frac{m_g^2}{E^2}\right)^{1/2} = \left(1 - \frac{\lambda^2}{\lambda_g^2}\right)^{1/2}, \tag{2.45}$$

where $E = \hbar\omega$ is the energy of the wave, λ its wavelength and $\lambda_g = h/m_g$ is the *Compton wavelength* of the graviton.

There are several ways to probe the graviton mass and place constraints on its value: a full review of the possible experimental tests and the most recent bounds can be found in [22]. Currently, GW detection is one of the most powerful instruments to constrain in a model-independent way gravitational wave speed and the graviton mass. From the combined observations by Advanced LIGO and Advanced Virgo in their first catalog GWTC-1 [5], a 90% credible bound was found on the graviton mass to be:

$$m_g \leq 4.7 \times 10^{-23} \, \frac{eV}{c^2} \, .$$

2.3 Gravitational-Wave Polarizations

Among the general properties of the wave in a generic Metric Theory of Gravity, polarization modes play a special role since, as we will see in Chapter 3, GW detectors responses to them are very specific.

GW polarization modes are the radiative degrees of freedom of the theory. As we have seen at the beginning of Sec. 2.1.4, in the context of GR the potentials $h^{\alpha\beta}$ in the *far wave zone* encode only two physical degrees of freedom. Indeed, we removed the redundant components by appealing to the harmonic gauge condition $\partial_\beta h^{\alpha\beta} = 0$ and its further refinement to the TT-gauge. In a generic metric theory, we cannot rely on the harmonic gauge condition. However, we can reduce the total degrees of freedom of the *far wave zone* metric down to six, using the standard freedom to transform the coordinates.

In the following, we will first provide a general proof of this property using the ppN form of the metric (as developed in Sec. 1.4) in the far wave zone. We will then explore an alternative demonstration based on more general arguments that allow for a group-theoretic classification of waves and metric theories.

2.3.1 Gravitational Potentials in the ppN Framework

Let's consider the form of the ppN metric for a stationary system in a frame in which the center-of-mass is at rest. The leading contribution at 1PN order ($\mathcal{O}(\epsilon^2)$) can be read from Eqs. (1.35):

$$g_{00} \simeq -1 + 2U + (\alpha_3 - \alpha_1) w^2 U + \alpha_2 w^j w^k X_{,jk} \, , \tag{2.46a}$$

$$g_{0j} \simeq -\frac{1}{2}\alpha_1 w_j U + \alpha_2 w^k X_{,jk} \, , \tag{2.46b}$$

$$g_{jk} \simeq (1 + 2\gamma U)\delta_{jk} \, , \tag{2.46c}$$

where $\mathbf{w}$ is the velocity of the frame with respect the universal rest frame. Using the relation (1.28), we can express the superpotential derivatives $X_{,jk}$ as a function of U and U_{jk}. Let $R \coloneqq |\mathbf{x}-\mathbf{x}'|$ and $\mathbf{N} \coloneqq \mathbf{x}/R$. Since we want to study the metric in the *far wave zone*, we can approximate the potentials neglecting contributions of order $\mathcal{O}(R^{-2})$, thus obtaining:

$$
\begin{aligned}
U &\equiv \int \frac{\rho^*(t,\mathbf{x}')}{|\mathbf{x}-\mathbf{x}'|}\mathrm{d}^3x' \simeq \frac{1}{R}\int \rho^*(t,\mathbf{x}')\mathrm{d}^3x' \equiv \frac{M}{R}\,,\\
U_{jk} &\equiv \int \rho^{*\prime}\ \frac{(x-x')_j(x-x')_k}{|\mathbf{x}-\mathbf{x}'|^3}\ \mathrm{d}^3x' \simeq UN_jN_k\,,\\
X_{,jk} &= U\delta_{jk} - U_{jk} = \frac{M}{R}(\delta_{jk}-N_jN_k)\,.
\end{aligned}
$$

where we implicitly defined M as the active gravitational mass of the source. We can rewrite the metric as:

$$
g_{00} \simeq -1 + \frac{M}{R}\left[2 + (\alpha_2+\alpha_3-\alpha_1)w^2 + \alpha_2(\mathbf{w}\cdot\mathbf{N})\right], \tag{2.47a}
$$

$$
g_{0j} \simeq \frac{M}{2R}w^k\left[(2\alpha_2-\alpha_1)\delta_{jk} - 2\alpha_2N_jN_k\right], \tag{2.47b}
$$

$$
g_{jk} \simeq \left(1+\frac{2\gamma M}{R}\right)\delta_{jk}\,. \tag{2.47c}
$$

From this metric, we can derive the potentials $h^{\alpha\beta} \coloneqq \eta^{\alpha\beta} - \mathfrak{g}^{\alpha\beta}$. After a straicght-forward calculation, we find that the potential are given by:

$$
h^{00} \simeq \frac{M}{R}(3\gamma+1)\,, \tag{2.48a}
$$

$$
h^{0j} \simeq \frac{M}{2R}w^k\left[(2\alpha_2-\alpha_1)\delta_{jk} - 2\alpha_2N_jN_k\right], \tag{2.48b}
$$

$$
h^{jk} \simeq \frac{M}{R}(1-\gamma)\delta_{jk}\,. \tag{2.48c}
$$

We now consider a time-dependent source that emits GWs: the stationary potentials are supplemented by the following time-dependent corrections $\Delta h^{\alpha\beta}$

$$
\Delta h^{00} = \frac{1}{R}C(\tau,\mathbf{N})\,, \tag{2.49a}
$$

$$
\Delta h^{0j} = \frac{1}{R}D^j(\tau,\mathbf{N})\,, \tag{2.49b}
$$

$$
\Delta h^{jk} = \frac{1}{R}A^{jk}(\tau,\mathbf{N})\,, \tag{2.49c}
$$

where $\tau \coloneqq t - R/v$ is the retarded time (v being the propagation speed of the wave) and C transforms as a scalar, D^j as a Cartesian vector and A^{jk} as a Cartesian symmetric tensor under rotation of the spatial axes. We can *uniquely* decompose these functions into irreducible pieces. The Cartesian vector field D^j can be written

in terms of a *longitudinal piece* ($N^j D$) and a *transverse piece* (D_T^j) as:

$$D^j = N_j D + D_T^j \quad , \quad N_j D_T^j = 0\,. \tag{2.50}$$

The Cartesian symmetric tensor A^{jk} can be decomposed into *trace* ($\delta^{jk}A$), *longitudinal-tracefree* ($N^j N^k - 1/3\delta^{jk}$), a *longitudinal-transverse* ($N^j A_T^k + N^k A_T^j$) and *transverse-tracefree* (A_{TT}^{jk}) pieces as:

$$A^{jk} = \frac{1}{3}\delta^{jk}A + \left(N^j N^k - \frac{1}{3}\delta^{jk}\right)B + N^j A_T^k + N^k A_T^j + A_{TT}^{jk}\,, \tag{2.51}$$

$$\text{where} \qquad N_j A_T^j = 0\,, \quad N_j A_{TT}^{jk} = \delta_{jk}A^{jk} = 0\,.$$

The ten independent components of $h^{\alpha\beta}$ are contained in the potentials C (one component), D_T^j (two components), D (one component), A (one component), B (one component), A_T^j (two components) and A_{TT}^{jk} (two components).

Now, we study how these potentials transform under a gauge transformation such that the form of $h^{\alpha\beta}$ is preserved. This requirement implies that the allowed transformations on coordinates are small deformations $x^\alpha \to x^\alpha + \zeta^\alpha(x)$ induced by a gauge 4-vector $\zeta^\alpha(x)$, whose general form we can write as:

$$\zeta^0 = \frac{1}{R}\alpha(\tau, \mathbf{N}) + \mathcal{O}\left(\frac{1}{R^2}\right), \tag{2.52a}$$

$$\zeta^j = \frac{1}{R}\beta^j(\tau, \mathbf{N}) + \mathcal{O}\left(\frac{1}{R^2}\right) \quad , \quad \beta^j = N^j\beta + \beta_T^j\,. \tag{2.52b}$$

The gauge vector field needs to be a harmonic function of the coordinates $\Box\zeta^\alpha(x) = \mathcal{O}(R^{-2})$ to preserve the form of the gravitational potentials. Using Eq. (2.21) and the derivation property for the far away zone of Eq. (2.18), the ten independent potentials will transform in the following way:

$$C' = C + \partial_\tau(\alpha + \beta)\,, \tag{2.53a}$$

$$D' = D + \partial_\tau(\alpha + \beta)\,, \tag{2.53b}$$

$$D_T'^j = D_T^j + \partial_\tau\beta_T^j\,, \tag{2.53c}$$

$$A' = A + \partial_\tau(3\alpha - \beta)\,, \tag{2.53d}$$

$$B' = B + 2\partial_\tau\beta\,, \tag{2.53e}$$

$$A_T'^j = A_T^j + \partial_\tau\beta_T^j\,, \tag{2.53f}$$

$$A_{TT}'^{jk} = A_{TT}^{jk}\,. \tag{2.53g}$$

We can rearrange the transformed potentials into *six gauge invariant quantities*:

$$A_S \coloneqq -\frac{1}{6}(A + 2B - 3C) \qquad \text{(one component)}\,, \tag{2.54a}$$

$$A_L \coloneqq \frac{1}{3}(A + 2B + 3C - 6D) \qquad \text{(one component)}\,, \tag{2.54b}$$

$$A_V^k \coloneqq A_T^k - D_T^k \qquad \text{(two components)}\,, \tag{2.54c}$$

$$A_{TT}^{jk} \qquad \text{(two components)}\,. \tag{2.54d}$$

These potentials represent the real physical six degrees of freedom encoded in $h^{\alpha\beta}$: we have indeed factor out the coordinate degrees of freedom from the perturbation by finding gauge independent potentials. The procedure illustrated in this section is completely general: if we have other gravitational fields, we can build gauge invariant quantities studying how they change under gauge transformations. Field equations, written in an appropriate form, will then provide constraints to distinguish between radiative and non-radiative (solution of Poisson like equations, for example) degrees of freedom.

In GR, the harmonic gauge condition $\partial_\beta h^{\alpha\beta}$ (which can be viewed as a consequence of the conservation of the pseudotensor $\tau^{\alpha\beta}$ via Einstein's equations) implies that:

$$C = D\,, \tag{2.55a}$$

$$D = \frac{1}{3}A + \frac{2}{3}B\,, \tag{2.55b}$$

$$A_T^k = D_T^k\,, \tag{2.55c}$$

making $A_S = A_L = A_V^k = 0$. Therefore, we correctly recover the two radiative degrees of freedom encoded in the transverse-tracefree part of the metric A_{TT}^{jk}.

2.3.2 The E(2) Framework and Classification

In the previous subsection, we showed that the total number of independent degrees of freedom for a GW in a generic theory of gravity is six. We provided a general proof that is essentially based on the gauge invariance of the ppN approximation applicable in every metric theory. However, there is a more general and interesting demonstration of this property that relies on the *Newman-Penrose (NP) formalism* [49] of curved spacetime, a result that was first obtained by Eardley *et al.* in [24, 23]. It is possible to prove that the most general null or nearly null wave has six independent polarization modes, which can be classified according to their behavior under Lorentz transformations. This fact leads to a group-theoretic classification of metric theories of gravity and it allows to place observational constraints on the correct one. In this subsection, we will summarise the argument of the original paper. Some of the obtained results will be useful in Sec. 3.2 for considerations on GW detector responses.

The Geodesic Deviation Equation

Einstein's Equivalence Principle (Sec. 1.2) establishes that it is always possible to choose a locally inertial frame where the Christoffel symbols vanish and the metric becomes locally flat. Consequently, it is not possible to define the absolute acceleration of a test mass at one point. However, it is still possible to have information on the curvature of spacetime. The Riemann tensor encodes such information, being zero if and only if the gravitational field is constant and uniform everywhere. Its components can be written as functions of Christoffel symbols:

$$R^{\mu}{}_{\nu\alpha\beta} = \Gamma^{\mu}_{\nu\beta,\alpha} - \Gamma^{\mu}_{\nu\alpha,\beta} + \Gamma^{\lambda}_{\nu\beta}\Gamma^{\mu}_{\alpha\lambda} - \Gamma^{\lambda}_{\nu\alpha}\Gamma^{\mu}_{\beta\lambda} \,. \tag{2.56}$$

It is possible to show that mutual tidal acceleration between two test masses depends only on the Riemann tensor itself, thus it is the only possible local observable that may be defined. Consider two particles moving along two nearby geodesics $x^{\mu}(\tau)$ and $x^{\mu}(\tau) + S^{\mu}(\tau)$, where τ is the *affine parameter* of the geodesics and $S^{\mu}(\tau)$ is the separation vector between the two. If spacetime is curved, initially parallel geodesics will eventually cross. It can be shown (see, e.g., Sec. 3.10 in [17] for a straightforward demonstration) that the *relative acceleration* between two geodesics A^{μ} can be written as:

$$A^{\mu} := \nabla_{\vec{t}}\left(\nabla_{\vec{t}}\, S^{\mu}\right) \equiv \frac{D^2 S^{\mu}}{d\tau^2} = R^{\mu}{}_{\nu\alpha\beta} t^{\nu} t^{\alpha} S^{\beta} \,, \tag{2.57}$$

where $\vec{t}$ is the tangent vector of the geodesics. Equation (2.57) is known as the *Geodesic Deviation Equation*. If we choose the affine parameter τ to be the proper time of two massive bodies with negligible self-gravitational energy, expressing the previous relation in a local Lorentz frame $\xi^{\mu} = (t, \boldsymbol{\xi})$ with its origin centered in one of the two, we can recognize in the right-hand side of Eq. (2.57) the acceleration between the two masses:

$$\frac{D^2 \xi^{\mu}}{d\tau^2} = -R^{\mu}{}_{\nu\alpha\beta} u^{\nu} \xi^{\alpha} u^{\beta} \,, \tag{2.58}$$

where u^{α} is the 4-velocity of the moving mass. For slowly moving particles, we can rewrite the previous equation as:

$$\frac{d^2 \xi_j}{dt^2} = -c^2 R_{0j0k} \xi^{k} \,. \tag{2.59}$$

We see that the relative acceleration depends only on the *electric* components of the Riemann curvature tensor. In this chapter, we have found that gravitational waves are perturbations of the metric field $g^{\alpha\beta}$ as well as of other fields of the theory. However, the resulting Riemann tensor (which is derived from the metric alone) is the only measurable field: this is the reason why we can define a "gravitational wave" in terms of the Riemann tensor it produces in *any metric theory*. In the limit of weak, plane, null wave propagating in vacuum, the linearized Riemann tensor depends only on the retarded time $R_{\mu\nu\alpha\beta} = R_{\mu\nu\alpha\beta}(u)$, where $u = t - r$ (from now on, $c = 1$). All the possible polarization modes of generic GWs follow immediately from the independent components of the Riemann tensor.

Riemann tensor in Newmann-Penrose formalism

The key idea of the NP formalism is to rewrite GR (and consequently every metric theory) in an coordinate-independent framework. Instead of choosing a coordinate frame, every tensor of the theory is projected onto a complete four null vector basis at each point in spacetime, called *null tetrad*. The basis used is usually chosen to reflect some symmetries of the curved spacetime, leading to simplified expressions for physical variables.

To treat gravitational radiation, a good choice of basis is the following:

$$\mathbf{n} = \frac{1}{\sqrt{2}}(\hat{t} + \hat{r})\,, \tag{2.60a}$$

$$\boldsymbol{\ell} = \frac{1}{\sqrt{2}}(\hat{t} - \hat{r})\,, \tag{2.60b}$$

$$\mathbf{m} = \frac{1}{\sqrt{2}}(\hat{\theta} + i\hat{\phi})\,, \tag{2.60c}$$

$$\bar{\mathbf{m}} = \frac{1}{\sqrt{2}}(\hat{\theta} - i\hat{\phi})\,, \tag{2.60d}$$

where $(\hat{t}, \hat{r}, \hat{\theta}, \hat{\phi})$ are the four versors of the ξ^μ system in spherical coordinates and $\mathbf{n}$ is aligned with the direction of propagation of the wave ($\mathbf{n}$ can be thought as the wave vector). In other terms, if we express $\mathbf{n}$ in the local Lorentz frame, we choose $n_\mu = u_{,\mu}$, where $u = t - r$ is the aforementioned retarded time. Being null vectors, their self-normalization vanishes. Furthermore, the tetrad vectors obey the following relations:

$$-\boldsymbol{\ell} \cdot \mathbf{n} = \mathbf{m} \cdot \bar{\mathbf{m}} = 1\,.$$

Each tensor of the theory can be locally projected along these four vectors, and its components can be written as:

$$R_{abc\ldots} \equiv R_{\mu\nu\alpha\ldots} a^\mu b^\nu c^\alpha \ldots\,,$$

where $a, b, c, \ldots$ run over $(n, \ell, m, \bar{m})$.

The Riemann curvature tensor has a total of 20 independent components. If we split the tensor in its irreducible parts under Poincaré transformations (Lorentz plus translation), we obtain three objects: the *Weyl tensor* $C_{\mu\nu\alpha\beta}$ (10 independent components), the *traceless Ricci tensor* $\tilde{R}_{\mu\nu}$ (9 independent components), and one *Ricci scalar* R (for definitions, see [48], Sec. 13.5). In the NP formalism, one encodes the 10 algebraic independent components of the Weyl tensor in five complex *Weyl-NP scalars*

$$\begin{aligned} \Psi_0 \coloneqq -C_{nmnm}\,,\ \Psi_1 \coloneqq -C_{n\ell nm}\,,\ \Psi_2 \coloneqq -\frac{1}{2}(C_{n\ell n\ell} - C_{n\ell m\bar{m}})\,, \\ \Psi_3 \coloneqq -C_{n\ell\bar{m}\ell}\,,\ \Psi_4 \coloneqq -C_{\bar{m}\ell\bar{m}\ell}\,, \end{aligned} \tag{2.61}$$

while the full Ricci tensor $R_{\mu\nu}$ has 10 components that are encoded into 4 *real scalars*

$$\Phi_{00} \coloneqq -\frac{1}{2}R_{nn}\,, \quad \Phi_{11} \coloneqq -\frac{1}{4}(R_{n\ell} + R_{m\bar{m}})\,, \quad \Phi_{22} \coloneqq -\frac{1}{2}R_{\ell\ell}\,, \quad \Lambda \coloneqq -\frac{R}{24}\,, \tag{2.62}$$

and 3 *complex scalars*

$$\Phi_{01} := -\frac{1}{2}R_{nm}\,, \quad \Phi_{02} := -\frac{1}{2}R_{mm}\,, \quad \Phi_{12} := -\frac{1}{2}R_{\ell m}\,. \tag{2.63}$$

For a weak, plane, null wave the Riemann tensor depends only on the retarded time: thus, every derivative with respect to the vectors $(n, m, \bar{m})$ is seen to vanish. Let $p, q, r, \ldots$ run over $n, m, \bar{m}$ only, we have that:

$$R_{abcd,p} = 0\ . \tag{2.64}$$

Furthermore, we can apply the *linearized Bianchi identities* $R_{ab[pq,\ell]} = 0$ to obtain:

$$R_{abpq} = 0\ . \tag{2.65}$$

Considering its symmetries, we see that the only non-vanishing components of the Riemann tensor for a weak, plane, null wave are of the kind $R_{p\ell q\ell}$, for a total of *six independent components*, that can be expressed as functions of $\{\Psi_2, \Psi_3, \Psi_4, \Phi_{22}\}$ as:

$$\Psi_2 = -\frac{1}{6}R_{n\ell n\ell}\,, \tag{2.66a}$$

$$\Psi_3 = -\frac{1}{2}R_{n\ell\bar{m}\ell}\,, \tag{2.66b}$$

$$\Psi_4 = -R_{\bar{m}\ell\bar{m}\ell}\,, \tag{2.66c}$$

$$\Phi_{22} = -R_{m\ell\bar{m}\ell}\,, \tag{2.66d}$$

where Ψ_2 is a real scalar. These amplitudes are related to the "electric" components of the Riemann tensor, which govern relative acceleration via Eq. (2.59), by:

$$\Psi_2 = -\frac{1}{6}R_{z0z0}\,, \tag{2.67a}$$

$$\Psi_3 = -\frac{1}{2}(R_{x0z0} - iR_{y0z0})\,, \tag{2.67b}$$

$$\Psi_4 = -R_{x0x0} + R_{y0y0} + 2iR_{x0y0}\,, \tag{2.67c}$$

$$\Phi_{22} = -R_{x0x0} - R_{y0y0}\,, \tag{2.67d}$$

where we assumed that the wave to be propagating along the z-axis ($\hat{r} \equiv \hat{z}$), without loss of generality.

$E(2)$ classification

We now attempt to classify the waves and their polarization modes by identifying some properties that are observer-independent. However, we choose to restrict our attention to a subgroup of "standard" observers such that:

- each observer agrees on the propagation direction of the wave (no pure rotation of the wave vector $\mathbf{n}$);
- each observer measures the same wave frequency (same Doppler effect).

The "standard" observers with the constraints we have just defined are connected by a subgroup of Lorentz transformations such that the wave vector $\mathbf{n}$ is kept fixed. The subgroup of Lorentz transformations that leaves a 4-vector unchanged is called *little group* (for details on the group-theoretic foundations, see [73]). If the 4-vector is null (like $\mathbf{n}$), its *little group* coincides with the $E(2)$ Euclidean group of rotations and translations on the plane: hence, the name of the classification.

The most general of this restricted class of transformations acts on the tetrad defined in Eqs. (2.60) as follows:

$$\mathbf{n}' = \mathbf{n}\,, \tag{2.68a}$$
$$\boldsymbol{\ell}' = \boldsymbol{\ell} + \bar{\alpha}\mathbf{m} + \alpha\bar{\mathbf{m}} + \alpha\bar{\alpha}\mathbf{n}\,, \tag{2.68b}$$
$$\mathbf{m}' = e^{i\phi}(\mathbf{m} + \alpha\mathbf{n})\,, \tag{2.68c}$$
$$\bar{\mathbf{m}}' = e^{-i\phi}(\bar{\mathbf{m}} + \bar{\alpha}\mathbf{n})\,, \tag{2.68d}$$

where α is an arbitrary complex number that produces null rotations (peculiar combination of boosts and rotations, also called *parabolic* Lorentz transformations) while ϕ is a real-valued phase that generates rotations about the propagation direction in space (the spacial part of $\mathbf{n}$). Under $E(2)$ transformations, the amplitudes of GWs will change accordingly:

$$\Psi_2' = \Psi_2\,, \tag{2.69a}$$
$$\Psi_3' = e^{-i\phi}(\Psi_3 + 3\bar{\alpha}\Psi_2)\,, \tag{2.69b}$$
$$\Psi_4' = e^{-2i\phi}(\Psi_4 + 4\bar{\alpha}\Psi_3 + 6\bar{\alpha}^2\Psi_2)\,, \tag{2.69c}$$
$$\Phi_{22}' = \Phi_{22} + 2\alpha\Psi_3 + 2\bar{\alpha}\bar{\Psi}_3 + 6\alpha\bar{\alpha}\Psi_2\,. \tag{2.69d}$$

Setting $\alpha = 0$, we recognize that the amplitudes $\{\Psi_2, \Psi_3, \Psi_4, \Phi_{22}\}$ are helicity eigenstates because they transform under a rotation of an angle ϕ with a phase factor $e^{is\phi}$, s being the helicity eigenvalue that can be read from Eqs. (2.69):

$$\begin{aligned} s(\Psi_2) &= 0\,, & s(\Phi_{22}) &= 0\,, \\ s(\Psi_3) &= -1\,, & s(\bar{\Psi}_3) &= +1\,, \\ s(\Psi_4) &= -2\,, & s(\bar{\Psi}_4) &= +2\,. \end{aligned} \tag{2.70}$$

Although the amplitudes are observer-dependent quantities, we can make certain frame-invariant statements about the presence or absence oof each amplitude, classifying the most general GW in 6 different categories. Each class is identified by a string, representing the Petrov type (see [55]) of their non-vanishing Weyl tensor, and a subscript, corresponding to the maximum number of non-vanishing amplitudes as seen by any observer. We have the following classification:

- Class II_6: $\Psi_2 \neq 0$;
- Class III_5: $\Psi_2 = 0$ and $\Psi_3 \neq 0$;
- Class N_3: $\Psi_2 = 0$, $\Psi_3 = 0$, $\Phi_{22} \neq 0$, $\Psi_4 \neq 0$;
- Class N_2: $\Psi_2 = 0$, $\Psi_3 = 0$, $\Phi_{22} = 0$, $\Psi_4 \neq 0$;
- Class O_1: $\Psi_2 = 0$, $\Psi_3 = 0$, $\Phi_{22} \neq 0$, $\Psi_4 = 0$;
- Class O_0: $\Psi_2 = \Psi_3 = \Phi_{22} = \Psi_4 = 0$. (No wave.)

Classes II_6 and III_5 belong to non-unitary and indecomposable representations. It is not possible for such theories to describe their waves through a massless particle field and they cannot be quantized in a way that is Poincaré-invariant with respect to the local Lorentz metric. Although the classification was developed for exactly null-waves, the considerations we made can be generalized for nearly-null waves (with propagation speeds close to c), apart from replacing the vanishing of the modes with corrections of order $\mathcal{O}(\epsilon)$, where $\epsilon = (c/v)^2 - 1$.

Each different theory of gravity makes different predictions, and this is one of the reasons why GW polarizations are among the strongest GR test we can perform. We now list results for a few metric theories.

General Relativity — In vacuum, Einstein's field equations lead to $R_{\mu\nu} = 0$. As a consequence, from Eqs. (2.66), we have that:

$$\Psi_2 = \Psi_3 = \Phi_{22} = 0\,. \tag{2.71}$$

Therefore, General Relativity is an N_2 class theory that predicts only two polarizations encoded in the complex amplitude Ψ_4.

Scalar-Tensor Theories — For a massless scalar field, the vacuum linearized field equations can be written from Eqs. (1.40) and (1.41) as:

$$G_{\mu\nu} = \frac{1}{\phi_0}(\phi_{,\mu\nu} - \eta_{\mu\nu}\Box_\eta\phi)\,, \tag{2.72}$$

$$\Box_\eta\phi = 0\,. \tag{2.73}$$

The solution to Eq. (2.73) is given by the plane null wave in Eq. (2.40). Then, from Eq. (2.72), we can write the Ricci tensor as:

$$R_{\mu\nu} = -\mathcal{B}e^{i\ell^\mu x_\mu}\ell_\mu\ell_\nu\,. \tag{2.74}$$

We then obtain

$$\Psi_2 = \Psi_3 = 0\,, \quad \Phi_{22} \neq 0\,, \ \Psi_4 \neq 0 \tag{2.75}$$

for the wave amplitudes. Consequently, Scalar-Tensor Theories are of class N_3.

Einstein-Æther Theory — Three different modes are present in this theory that belongs to different classes, with different propagation speeds, as reported in Fig. 2.2.

Chapter 3

Gravitational-Wave Detection

This chapter provides an overview on interferometric techniques used in GW detectors and then analyzes in detail the response of an interferometer to a spacetime perturbation. Particular attention will be paid to how the GW polarization mode content is measured by the detector. A first new quantitative study on the sensitivity to specific polarization modes of a network of interferometers is performed. In the last section, two model-independent methods of polarization reconstruction are presented.

3.1 Gravitational-Wave Interferometers

In Chapter 2, we showed that Metric Theories of Gravity generally predict the existence of GWs. However, as discussed in Sec. 2.1.4, Eq. (2.27), the amplitude of the predicted perturbation is usually so small that GW detection is a real experimental challenge. The first attempts to GW detection were made by Joseph Weber in the 60s using resonant bar detectors, but their sensitivity was not enough to detect the small ripples in spacetime. The revolution was brought by the use of *interferometers*, optical instruments which use the principle of superposition to combine electromagnetic waves and to extract physical information from the apparatus.

Interferometric techniques are based on the *interference principle*, a consequence of the wave nature of light. The classic experiment that demonstrates interference of light was performed by the English scientist *Thomas Young (1773-1829)* in 1802. His *double slits experiment* has a simple setup: light is passed through a pinhole so as to illuminate an aperture consisting of two narrow slits. On a screen placed beyond the slits, a pattern of bright and dark interference bands (called *interference pattern*) is seen to form. Indeed, if we mix two waves with the same frequency, the resulting intensity pattern is determined by the phase difference between the two waves. This is related to the *superposition principle*. The linearity of Maxwell's equations implies that electromagnetic fields add up at a fixed point in empty space. Thus, waves that are in phase will undergo constructive interference, while waves that are out of phase will undergo destructive interference. Waves which are not completely in phase nor completely out of phase will have an intermediate intensity pattern, which can be used to determine their relative phase difference.

3.1.1 The Michelson Interferometer

Although several configurations of interferometers were developed along the years, one of the most versatile devices was invented by the American physicist *Albert Abraham Michelson (1852-1931)*, and was called in his honor *Michelson's interferometer*. The 1881 version scheme, as it appeared in his article *"The relative motion of the Earth and the Luminiferous ether"* [45], is reported in Fig. 3.1. Its basic design was very simple: light from a lamp (a) passed through a lightly silvered glass plate or a *beam splitter* (b): part of it went to the mirror c, and part of it was reflected towards the mirror d. The two separated beams, reflected at the end of each arm, are then recombined on a screen (e). Usually a compensating plate (g) is inserted in one beam in order to have the two optical paths include the same thickness of glass. If δ is the path difference between the two rays reaching e, then it is possible to show (see [34]) that the irradiance I is proportional to

$$I \propto 1 + \cos\frac{2\pi\delta}{\lambda} \equiv 1 + \cos\Delta\varphi\,, \tag{3.1}$$

where λ is the wavelength of the light used and $\Delta\varphi$ the phase difference of the two beams at recombination. In other terms, a simple interferometer is sensitive to variation of length of its arms comparable to the wavelength of light.

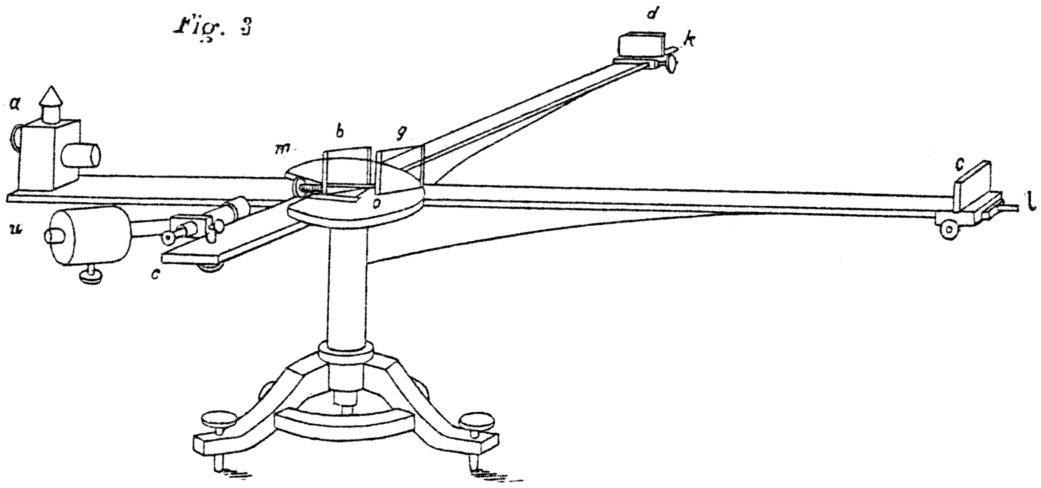

Figure 3.1. *Michelson's interferometer in his perspective drawing as published in [45].* Although ultimately incapable of distinguishing between differing theories of aether-dragging, it provided important lessons for the design of Michelson and Morley's 1887 instrument.

Michelson's interferometer was created to measure the dragging-effect of the *luminiferous aether* due to earth's motion around the Sun. The wave nature of light, understood as a classic wave, required the existence of a medium, called the *aether*, whose vibrations produce the electromagnetic waves, and which is supposed to fill space. During its revolution around the Sun, the Earth would have faced an "aether's wind" along its direction of motion: this effect would have slowed down the light travelling along the arm aligned with the motion, without altering the speed in the other arm, perpendicular to it. By the simple use of Euclidean geometry, first Alfred Potier (1882) and then Hendrick Lorentz (1886) had shown that this effect would have been equivalent to a path difference δ of:

$$\delta \simeq \frac{2Lv^2}{c^2} \tag{3.2}$$

where L was the interferometer arms length and v the velocity of Earth with respect to the aether. Therefore, a shift of the *fringes* (bright bands of the interference pattern) was expected.

Michelson's 1881 experiment was inconclusive, mainly for the reduced length of the apparatus that limited the sensitivity of the experiment. In 1887, Michelson and Morley repeated the experiment [46], using multiple reflected beams, increasing the equivalent length of the arms up to 11 m. A shift of ~ 0.5 of the fringes was expected, but no effect was seen. The experiment became what has been called the most famous failed experiment in history of Physics. However, it was dramatically fruitful: it was the first strong proof against the existence of aether, which leads the path to a new comprehension of the world.

3.1.2 Interaction of a Gravitational Wave and an Interferometer

An apparatus with Michelson's interferometer at its heart was used almost 130 years later to detect GWs. Before developing the maths to fully describe the interaction of an interferometer with a GW, it is interesting to follow a heuristic description based on Rainer Weiss's review in [72] to gain intuition on how interferometers can interact with spacetime perturbations. In Chapter 2, we saw that far from the source GWs can be thought of as distortions of the spatial geometry (only transverse to the propagation direction if we are in GR). These small perturbations of a locally flat metric $\eta^{\alpha\beta}$ can be written as:

$$g_{ij} = \eta_{ij} + h_{ij} \,. \tag{3.3}$$

where gauge freedom allows us to set h^{00} and h^{0i} to zero, as we showed in Sec. 2.3.

We can describe the propagation of light along an interferometer arm in the local Lorentz frame (t, ξ^i) with the origin placed at the beam splitter with a null spacetime interval Δs^2:

$$\Delta s^2 = 0 = g_{ij} d\xi^i d\xi^j = (1+h) L_0^2 - \Delta t^2 \,, \tag{3.4}$$

where h is a mean (diagonal) perturbation and L_0 is the arm spatial length. The "real" distance L between the end points of the arm is determined by the ligth travel time Δt as measured by local synchronized clocks, which are not affected by the perturbation:

$$L = \Delta t \simeq \left(1 + \frac{h}{2}\right) L_0 \,. \tag{3.5}$$

Therefore, substituting the estimated value for h from Eq. (2.27), the path difference produced in a 4 km interferometer arm by a GW is:

$$d \simeq h L_0 \simeq 10^{-19} \times 4\,\mathrm{km} \simeq 10^{-16}\,\mathrm{m} \,, \tag{3.6}$$

much smaller than any feasible wavelength. From Eq. (3.5), it is clear that if we want to have any hope to detect GWs using an interferometer, we have to increase the arm length by thousands of times.

3.1.3 Fabry-Pérot Cavities

The winning idea is to modify the Michelson setup to so that it includes two resonant *Fabry-Pérot cavities*, one in each arm, as in Fig. 3.2. A Fabry-Pérot cavity is an optical device made by two parallel reflecting mirrors. Electromagnetic waves can pass through it only if a resonant condition is verified. Indeed, the electric field will transmit through the cavity and build up inside only if the length of the mirrors separation is an integer number of half wavelengths. Once the beams are inside the cavity, they are reflected multiple times and partially transmitted outside, where they add up together in a geometrical series. The parameter that regulates the sharpness of the interference fringes is called *finesse* F and it is related to the reflectance R of the mirrors as:

$$F = \frac{4R}{(1-R)^2} \,. \tag{3.7}$$

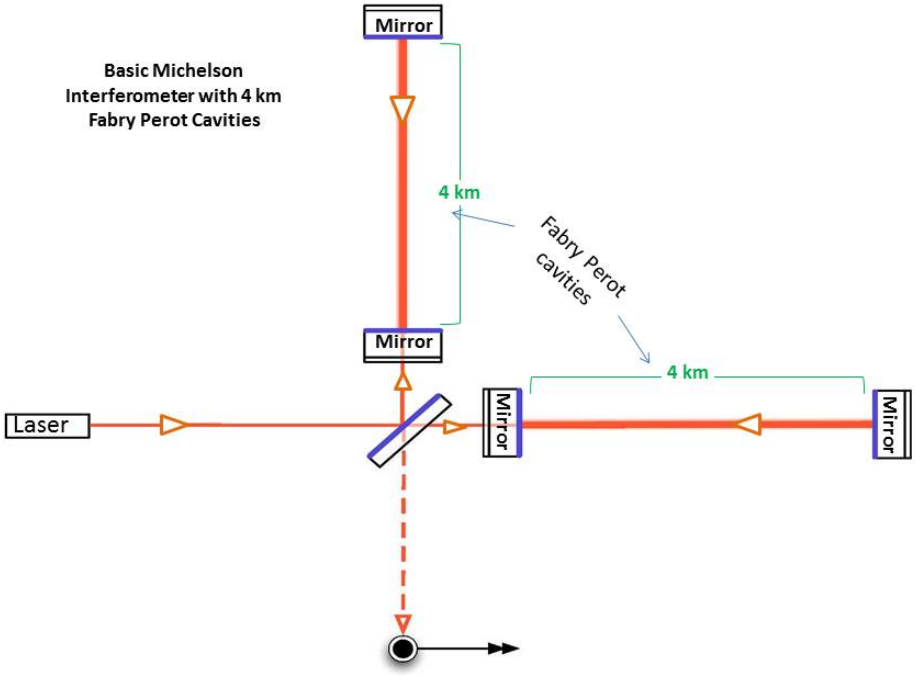

Figure 3.2. *Fabry-Pérot interferometer.* This scheme represents the core of any gravitational-wave interferometric detector. Each of the the two arms is filled with a Fabry-Pérot resonant cavity, which increase both the effective length of the arms and the sensitivity to small mirror displacements. [Reproduced from `https://www.ligo.caltech.edu/page/ligos-ifo`.]

The transmitted intensity is proportional to the *Airy function* (see [34] for a detailed derivation):

$$\frac{1}{1 + F \sin^2\left(\dfrac{\Delta\phi}{2}\right)}\,, \tag{3.8}$$

where $\Delta\phi$ is the total phase accumulated in a *round trip* (a complete travel back and forth in the cavity). If the argument $\Delta\phi/2$ of the sine term is an integer multiple of π, the Airy function is equal to unity, regardless of the finesse value. This creates concentric interference fringes at the output of the system. If the reflectance is very small (low finesse), the interference fringes are broad and indistinct; whereas if R is close to unity (high finesse), the fringes are very sharp. The phase, apart from a constant factor due to the reflection δ_r, can be related to the geometry of the interferometer. If we call L the length of the cavity, θ the incoming wave incidence angle, and λ the wavelength, assuming the rays propagate in vacuum, we find:

$$\Delta\phi = \frac{4\pi}{\lambda} L \cos\theta + \delta_r\,. \tag{3.9}$$

Fabry-Pérot cavities in GW interferometers provide a double advantage. Firstly, they allow laser light to build up within the interferometer. A high number of cycling photons increases the detector sensitivity. Secondly, folding the path of light multiple times allows the effective length of the interferometer arms to be much longer, increasing their sensitivity to perturbations brought by GWs. After entering the instrument via the beam splitter, the laser in each arm bounces between its two mirrors about 300 times prior to being merged with the beam from the other arm. This feature results in an effective length of almost 1200 km for each arm, making the detectability of GWs possible.

3.2 Full Analysis of the Interferometer Response to a Gravitational Wave

This section carries out a detailed analysis of the interferometer *differential arm (DARM) response* to GWs. Relations between different frames of reference will be used to find the *antenna patterns*, angular sensitivity functions of the instrument which are seen to depend only on the polarization of the incoming wave. The antenna patterns for both a two-arm and a three-arm interferometer are reported. These are obtained from the code fully reported in App. B written to develop the phenomenological part of this thesis (described in Ch. 5) and constitute a first independent result to validate the approach.

3.2.1 Test Mass Displacement

We want to describe the Fabry-Pérot Michelson interferometer hit by a (plane) GW as two pairs of test masses (at the ends of the two resonant cavities situated in the two arms of the detector) subject to a metric perturbation: the response of the detector depends on the difference in travel time along the two arms. In a local Lorentz frame, the behavior of the separation vector ξ^α between the two ends of the same arm is given by the equation of geodesic deviation in its slow-motion limit (2.59), which we repeat here for convenience:

$$\frac{d^2\xi_j}{dt^2} = -c^2 R_{0j0k}\xi^k \ .$$

The components R_{0j0k} of the linearized Riemann tensor are given as functions of the $h^{\alpha\beta}$ potentials by:

$$R_{0j0k} = -\frac{1}{2}\left(\partial_{00}h^{jk} - \frac{1}{2}\partial_{00}h\delta_j k + \partial_{jk}h^{00} + \frac{1}{2}\partial_{jk}h + \partial_{0j}h^{0k} + \partial_{0k}h^{0j}\right), \qquad (3.10)$$

where $h \coloneqq \eta_{\alpha\beta}h^{\alpha\beta}$ and D is the distance from the GW source. In GR, R_{0j0k} may be expressed completely in terms of the transverse-traceless part of the metric h^{jk}_{TT}. However, if we are in a generic metric theory, exploiting the relations we found in Sec. 2.3.1, we can express the potentials as functions of the six gauge invariant

quantities in Eqs. (2.54). Therefore, we have:

$$\frac{d^2\xi_j}{dt^2} = -\frac{G}{2c^4 D}\frac{\partial}{\partial\tau^2}S_{jk}(\tau,\mathbf{N})\xi_k\,, \tag{3.11}$$

where

$$S^{jk} \coloneqq (\delta^{jk} - N^j N^k)A_S + N^j N^k A_L + 2(N^j A_V^k + N^k A_V^j) + A_{TT}^{jk}\,. \tag{3.12}$$

Here, $\mathbf{N} = (\cos\phi\sin\theta, \sin\phi\sin\theta, \cos\theta)$ is a unit 3-vector which points towards the direction of the source in the sky, identified by the two polar angles (θ,ϕ) on the celestial sphere (the wave propagation direction), τ is the retarded proper time and the tensor S_{ij} contains time-dependent amplitudes of the perturbation. Integrating over time, we obtain the equation of motion for the displacement of one test mass with respect to the other at first order:

$$\xi^j(t) = \xi^j(0) + \frac{G}{2c^4 D}S^{jk}(\tau,\mathbf{N})\xi_k(0)\,. \tag{3.13}$$

Therefore, the single test mass displacement depends on which GW modes are impinging onto the detector.

3.2.2 Polarizations

To understand in concrete terms and visualize GW polarizations, it is interesting to examine the geodesic deviations they generate on a ring of free-falling particle. To do this, we must first choose a convenient basis to write the S^{jk} tensor explicitly. A *transverse frame* is conventionally chosen, in which the basis vectors $(\mathbf{N}, \mathbf{e_X}, \mathbf{e_Y})$ can be expressed as functions of the polar angle θ and the azimuthal angle ϕ, introduced to describe the direction of propagation on the celestial sphere, as:

$$\mathbf{N} \coloneqq [\sin\theta\cos\phi, \sin\theta\sin\phi, \cos\theta]\,, \tag{3.14}$$

$$\mathbf{e_X} \coloneqq [\cos\theta\cos\phi, \cos\theta\sin\phi, -\sin\theta]\,, \tag{3.15}$$

$$\mathbf{e_Y} \coloneqq [-\sin\phi, \cos\phi, 0]\,. \tag{3.16}$$

The basis provides the following *completeness relation*:

$$\delta^{jk} = N^j N^k + e_X^j e_X^k + e_Y^j e_Y^k\,. \tag{3.17}$$

We then define the six *gravitational-wave polarizations* from the gauge independent potentials of Eqs. (2.54) to be:

$$A_b \coloneqq A_S\,, \tag{3.18a}$$

$$A_l \coloneqq A_L\,, \tag{3.18b}$$

$$A_x \coloneqq e_X^j A_V^j\,, \tag{3.18c}$$

$$A_y \coloneqq e_Y^j A_V^j \tag{3.18d}$$

$$A_+ \coloneqq \frac{1}{2}(e_X^j e_X^k - e_Y^j e_Y^k)A_{TT}^{jk}\,, \tag{3.18e}$$

$$A_\times \coloneqq \frac{1}{2}(e_X^j e_Y^k + e_Y^j e_X^k)A_{TT}^{jk}\,. \tag{3.18f}$$

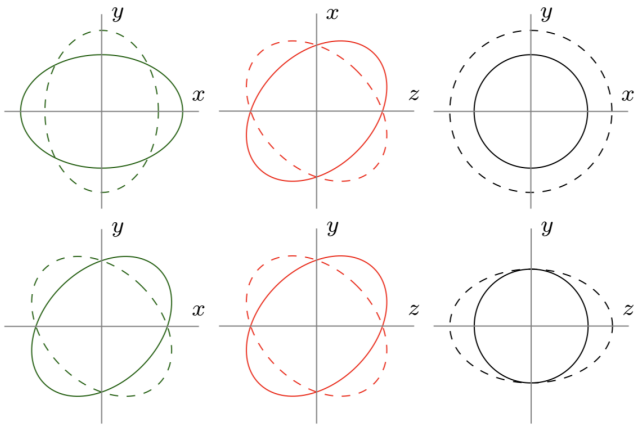

Figure 3.3. *Effect of different GW polarizations on a ring of free-falling test particles.* Plus (+) and cross (×) tensor modes (green); vector-x (x) and vector-y (y) modes (red); breathing (b) and longitudinal (l) scalar modes (black). In all of these diagrams, the wave propagates in the z direction. This decomposition into polarizations was first proposed for generic metric theories in [23], as discussed in Sec. 2.3.2. [Reproduced from [38].]

We can finally rewrite S^{jk} using the polarizations just defined and the completeness relation Eq. (3.17) as:

$$\begin{aligned} S^{jk} &= (e_X^j e_X^k + e_Y^j e_Y^k)A_b + N^j N^k A_l \,, \\ &+ (e_X^j N^k + e_X^k N^j)A_x + (e_Y^j N^k + e_Y^k N^j)A_y \,, \\ &+ (e_X^j e_X^k - e_Y^j e_Y^k)A_+ + (e_X^j e_Y^k + e_Y^j e_X^k)A_\times \,. \end{aligned} \tag{3.19}$$

Assuming that the wave travels along the z-direction, we therefore have:

$$S^{jk} = \begin{pmatrix} A_b + A_+ & A_\times & A_x \\ A_\times & A_b - A_+ & A_y \\ A_x & A_y & A_l \end{pmatrix} . \tag{3.20}$$

On a circular ring of free-falling particles, the perturbation produces a displacement given by Eq. (3.13) that, in terms of the (x, y, z) components of the vector ξ^j, is written as:

$$\begin{aligned} x(t) &= x_0 + \frac{G}{2c^4 D}\Big[(A_b + A_+)x_0 + A_\times y_0 + A_x z_0\Big] \,, \\ y(t) &= y_0 + \frac{G}{2c^4 D}\Big[A_\times x_0 + (A_b - A_+)y_0 + A_y z_0\Big] \,, \\ z(t) &= z_0 + \frac{G}{2c^4 D}\Big[A_x x_0 + A_y y_0 + A_l z_0\Big] \,, \end{aligned}$$

with $\xi(0) = (x_0, y_0, z_0)$. We have a total of six different modes, the specific action of which is illustrated in Fig. 3.3. Two scalar modes A_b and A_l, called *breathing* and *longitudinal* mode, respectively, one of which (A_b) is transverse to the wave propagation direction. Two vector modes A_x and A_y, partly longitudinal and partly transverse. Finally, two tensorial transverse modes $A_\times$ and A_+. GR allows for $A_\times$ and A_+ only.

With this last particular choice of wave direction, we can compare the amplitudes with Eqs. (2.67) by using Eq. (2.59) and find the following useful relation between the polarization amplitudes A_P and the Newman-Penrose quantities:

$$\begin{aligned}
\mathrm{Re}\Psi_4 &= \frac{G}{2c^4 D}\ddot{A}_+ \,, & \mathrm{Im}\Psi_4 &= -\frac{G}{2c^4 D}\ddot{A}_\times \,, \\
\mathrm{Re}\Psi_3 &= \frac{G}{4\sqrt{2}c^4 D}\ddot{A}_x \,, & \mathrm{Im}\Psi_3 &= -\frac{G}{4\sqrt{2}c^4 D}\ddot{A}_y \,, \\
\Phi_{22} &= \frac{G}{2c^4 D}\ddot{A}_b \,, & \Psi_2 &= \frac{G}{12c^4 D}\ddot{A}_l \,.
\end{aligned} \tag{3.21}$$

As seen in Sec. 2.3.2, from a field-theoretic point of view polarizations are strictly related to the helicity (projection of the spin along the motion) of the *graviton*: a massless graviton has only ± 2 helicity, which correspond to the two tensorial polarizations of GR. However, having extra polarizations does not necessarily imply a *massive* graviton. Indeed, as we saw in Sec. 2.2.2, Scalar-Tensor theories allow for a scalar breathing mode carried by the scalar field perturbation Ψ, since the physical waveform $h^{\alpha\beta}$ is related to $\tilde{h}^{\alpha\beta}$ by the relation:

$$h^{\alpha\beta} = \tilde{h}^{\alpha\beta} + \Psi\eta^{\alpha\beta} \,.$$

Massive Scalar-Tensor theories can have also a longitudinal mode, suppressed by a factor of $(\lambda/\lambda_c)^2$ with respect to the breathing one. More general theories of gravity can present up to six polarizations: Einstein-Æther theory predicts all six modes (see [40] or Fig. 2.2).

3.2.3 Differential Arm Response Function

While the amplitudes and the phases of GWs depend crucially on the source dynamics, the response of a quadrupolar antenna to them is determined by the geometry of the system source-detector (up to an overall normalization), as we will see in the following. Let $\mathbf{e_1}$ and $\mathbf{e_2}$ be the unit vectors aligned with the two arms of the interferometer, of equal length L_0. If we place the origin of the local Lorentz frame at the beam splitter, the test mass at the end of the first arm will be at a position $\boldsymbol{\xi}_1 = L_0\mathbf{e_1}$, while the other will be at at $\boldsymbol{\xi}_2 = L_0\mathbf{e_2}$. Assuming that the armlength is much shorter than the wavelength of the GW, the displacement of each test mass is given by Eq. (3.13):

$$\xi_1^j = L_0\left(e_1^j + \frac{G}{2c^4 D}S^{jk}e_1^k\right) , \tag{3.22a}$$

$$\xi_2^j = L_0\left(e_2^j + \frac{G}{2c^4 D}S^{jk}e_2^k\right) . \tag{3.22b}$$

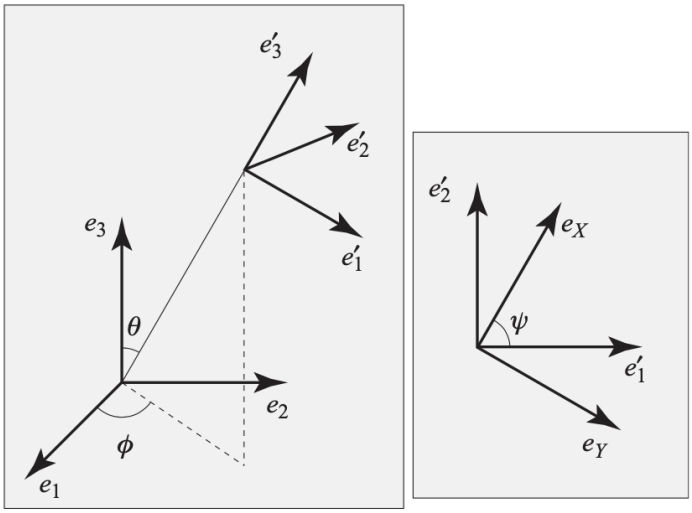

Figure 3.4. *Detector frame and transverse frame comparison.* The various polarization degrees of the wave, according to Sec. 3.2.3, are projected onto a transverse basis that is aligned with its direction of propagation. We can determine the relative position with respect to the detector using the three angles θ, ϕ and ψ shown above. Therefore, three rotations are necessary to transform the components of a vector from one frame to the other. [Reproduced from [56].]

The length of each arm at first order in the perturbation is given by

$$L_1 = L_0\left(1 + \frac{G}{2c^4 D} S_{jk} e_1^j e_1^k\right), \tag{3.23a}$$

$$L_2 = L_0\left(1 + \frac{G}{2c^4 D} S_{jk} e_2^j e_2^k\right). \tag{3.23b}$$

The response of the interferometer is regulated by the phase difference $\Delta\varphi$ at beam recombination, i.e. the argument of the cosine function in Eq. (3.1). Being $\delta = 2(L_1 - L_2)$, we have that:

$$\Delta\varphi = \frac{4\pi}{\lambda}\frac{G}{c^4 D}\frac{1}{2}(e_1^j e_1^k - e_2^j e_2^k) S_{jk}(\tau, \mathbf{N}) \equiv \frac{4\pi}{\lambda}\frac{G}{c^4 D} S(t)\,, \tag{3.24}$$

where $S(t)$ is known as the *differential arm* (DARM) response function.

To understand the behavior of the interferometer response function, we have to express all quantities in Eq. (3.24) in the same reference frame. As shown in Fig. 3.4, two different 3-vector bases are involved here. The polarization degrees of the wave, components of the tensor S_{jk}, are usually projected onto the orthonormal basis $(\mathbf{N}, \mathbf{e_X}, \mathbf{e_Y})$ we defined back in Sec. 3.2.2, aligned with the direction of propagation of the wave $\mathbf{N}$, called the *transverse frame*. On the other hand, the interferometer *DARM* response depends on a *detector tensor*, linear combination of the versors aligned with the antenna arms, which is therefore conveniently written in the *detector frame* basis, $(\mathbf{e_1}, \mathbf{e_2}, \mathbf{e_3})$. Three degrees of freedom are needed to link the two basis. We first generically assume that $(\mathbf{e_X}, \mathbf{e_Y})$ are rotated by the *polarization angle* ψ

around $\mathbf{N}$ with respect to the basis $(\mathbf{e_1'}, \mathbf{e_2'})$. These primed vectors are obtained by two subsequent rotations of $(\mathbf{e_1}, \mathbf{e_2})$ performed to align $\mathbf{e_3}$ with $\mathbf{N}$. We can write the total response as a function of three angles (θ, ϕ, ψ):

$$S(t) = F_P(\theta, \phi, \psi) A_P \tag{3.25}$$

where a sum runs over all polarizations $P = \{b, l, x, y, +, \times\}$. The F_P's are called *antenna pattern functions*. Their explicit computation for a two-arm interferometer yields the following relations:

$$F_b = -\frac{1}{2} \sin^2\theta \cos 2\phi \,, \tag{3.26a}$$

$$F_l = \frac{1}{2} \sin^2\theta \cos 2\phi \,, \tag{3.26b}$$

$$F_x = -\sin\theta (\cos\theta \cos 2\phi \cos\psi - \sin 2\phi \sin\psi) \,, \tag{3.26c}$$

$$F_y = -\sin\theta (\cos\theta \cos 2\phi \sin\psi + \sin 2\phi \cos\psi) \,, \tag{3.26d}$$

$$F_+ = \frac{1}{2}(1 + \cos^2\theta) \cos 2\phi \cos 2\psi - \cos\theta \sin 2\phi \sin 2\psi \,, \tag{3.26e}$$

$$F_\times = \frac{1}{2}(1 + \cos^2\theta) \cos 2\phi \sin 2\psi + \cos\theta \sin 2\phi \cos 2\psi \,. \tag{3.26f}$$

As a first step to validate our code (fully reported in Appendix B), a complete study of the antenna patterns for a two-arm and a three-arm interferometer was performed. The results are reported in Figs. 3.5 and 3.6. For a detailed description of the simulated three-arm interferometer, see [59]. As seen from Eqs. (3.26), the detector response to the scalar polarizations (apart from a sign) is completely degenerate; this holds even in the three-arm interferometer configuration. Therefore, the two polarizations cannot be distinguished from one another and from now on we will consider only a single scalar mode S, with corresponding antenna response F_S. Furthermore, the sensitivity of a three-arm detector is — on average — greater than the two-arm configuration, presenting also a peculiar azimuthal symmetry in the detector frame.

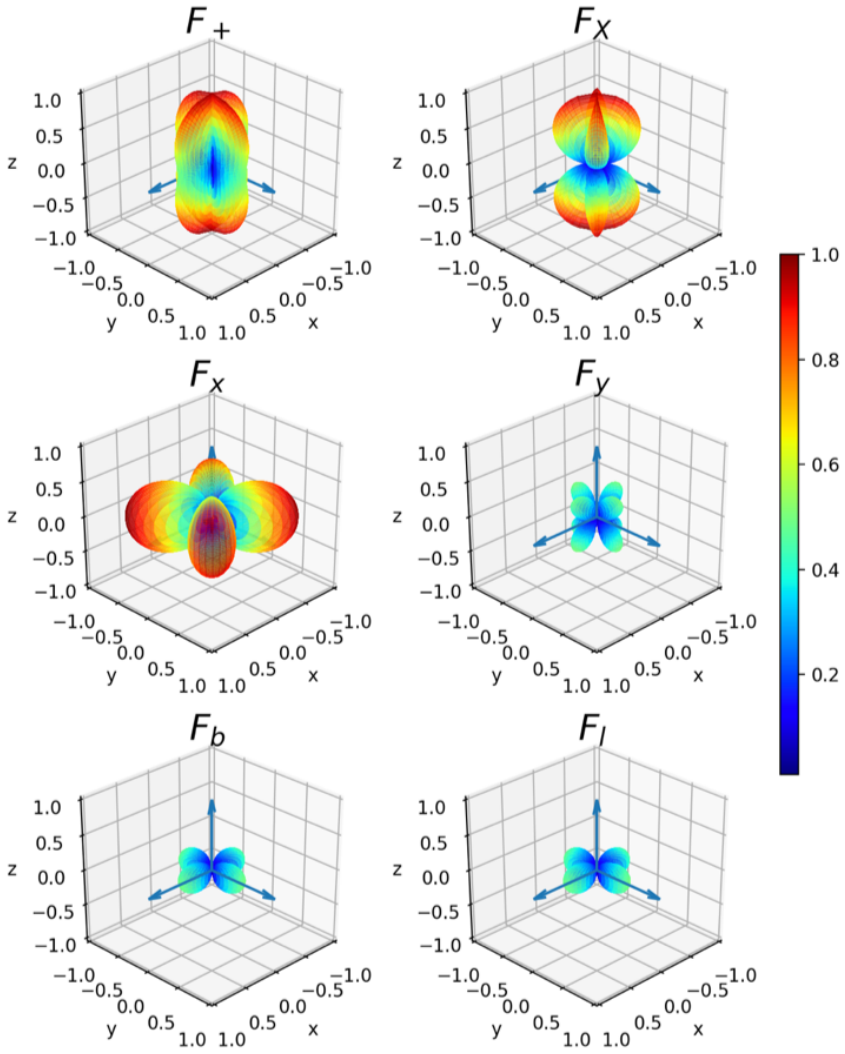

Figure 3.5. *Angular response of a two-arm interferometer to each GW polarization.* The radial distance represents the response of a single two-arm quadrupolar antenna to a unit-amplitude gravitational signal of a tensor (top), vector (middle), or scalar (bottom) polarization, i.e. $|F_P|$ for each polarization P for $\psi = 0$. The polar and azimuthal coordinates correspond to the source location with respect to the detector, which is to be imagined as placed with its vertex at the center of each plot and arms along the x and y-axes. The response is plotted to scale, such that the blue lines representing the detector arms have unit length in all plots.

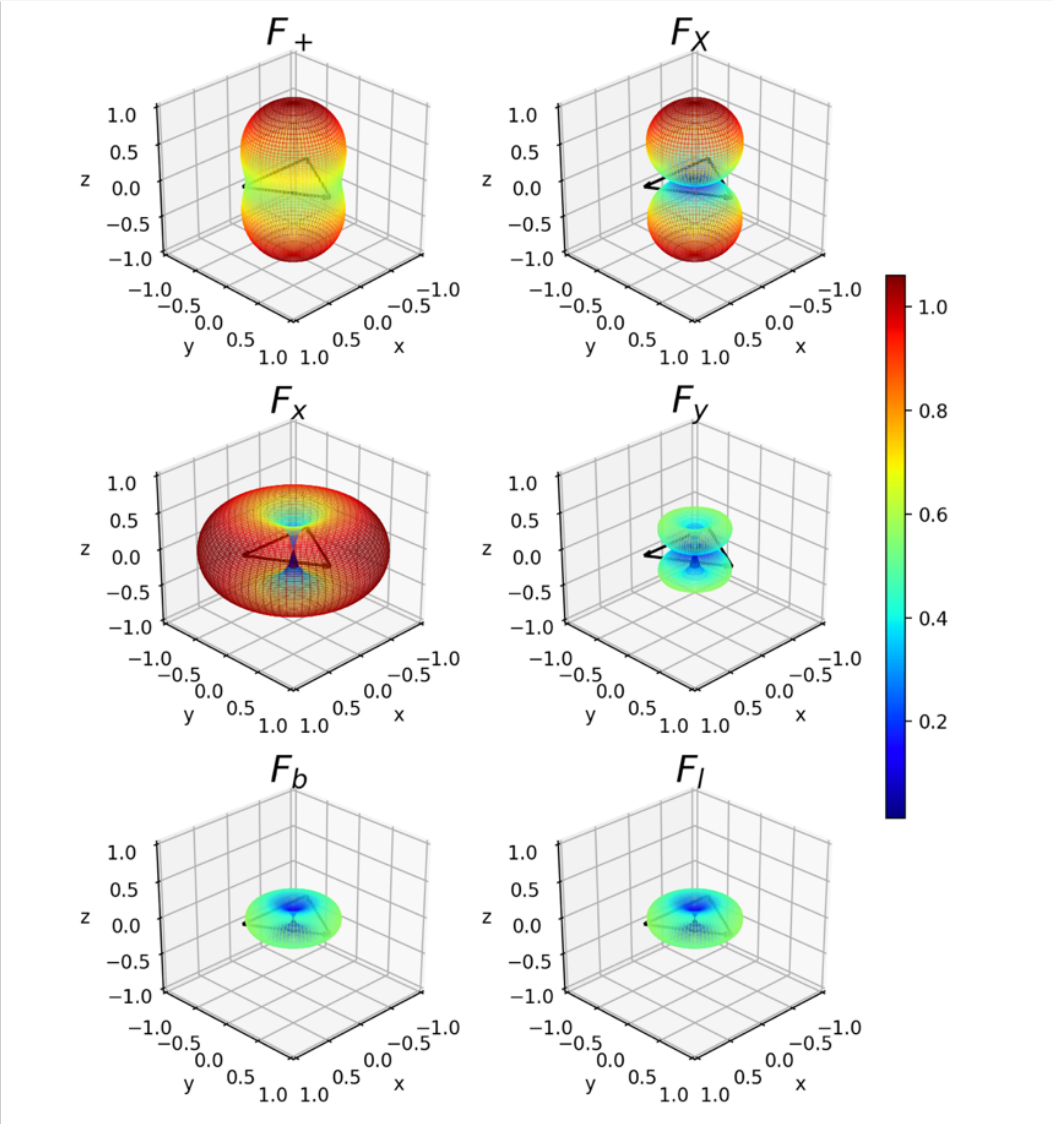

Figure 3.6. *Angular response of a three-arm interferometer to each GW polarization.* The radial distance represents the response of a system with a triangular topology, where the arms of the equilateral triangle are each used twice to form three Michelson interferometers. One can show analytically that the response to the different GW polarizations is equivalent to that of two L-shaped detectors with arm length 3L/4. In the figure, the response to a unit-amplitude gravitational signal of a tensor (top), vector (middle), or scalar (bottom) polarization is shown, i.e. $|F_P|$ for each polarization P for $\psi = 0$. The polar and azimuthal coordinates correspond to the source location with respect to the detector, which is to be imagined as placed with its center in the origin of each frame. The response is plotted to scale, such that the black lines representing the detector arms have unit length in all plots.

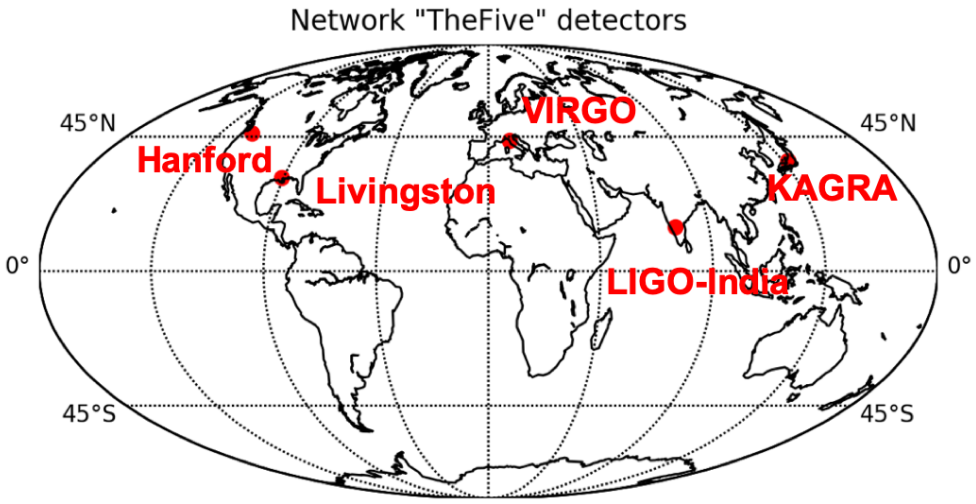

Figure 3.7. *The five-interferometer GW network available in the near future, used for this research.*

3.3 Network of Interferometers and Overlaps

In the measurement of GW polarizations, eight different unknowns play a role: the six polarization modes and the two angles that identify the position of the source in the sky. However, as mentioned earlier, the DARM response functions of a laser interferometer to the two scalar modes are completely degenerate, and we are therefore left with five independent polarization modes. The number of available quadrupolar antennas is then crucial in fully measuring the polarization content of GW signals. Further, the relative orientations of the arms of the instruments plays a fundamental role. While aligning the arms of a pair of interferometers maximises the probability of coincident (between detectors) detection, it hampers the possibility of distinguishing between different polarizations because the antenna pattern functions of the two detectors will be the same.

The location of the instruments of the GW detector network is shown in Fig. 3.7. Other than Virgo and the two LIGO interferometers in Hanford (USA) and Livingston (USA), two other detectors are shown: KAGRA, the Kamioka Gravitational Wave Detector, which started taking data on February 25, 2020, and LIGO-India, a third LIGO instrument that is expected to be completed in ∼2025. Additionally, the prospect of building a new generation of detectors, the so called 3G detectors, is under discussion and investigation by the international scientific community [36, 57]. This is the network used to produce the studies reported in this thesis.

If we are interested in the sensitivity of a network of N detectors, it is useful to define the effective response vector as:

$$\vec{F}_H(\theta,\phi) := (|F_H^1(\theta,\phi)|, ..., |F_H^N(\theta,\phi)|)\,, \tag{3.27}$$

where we set $\psi = 0$ since we are not dealing with any specific source, and where the F_H^i's are the sums in quadrature of the two *antenna patterns* of the i-th detector for each polarization $H = \{s, v, t\}$ (scalar, vector, tensor). With these quantities in hand, we can determine the effective sensitivity of the network to non-tensorial polarizations with respect to tensorial ones by computing the *overlap* factor:

$$\mathcal{F}_{H/t} = \frac{\vec{F}_H(\theta,\phi)\cdot\vec{F}_t(\theta,\phi)}{\vec{F}_t(\theta,\phi)\cdot\vec{F}_t(\theta,\phi)}\,, \tag{3.28}$$

where $H \neq t$.

It is essential to quantify in advance, through simulations, how GW detector configuration choices affect our ability to measure the GW polarization content, as this measurement can place strong, fundamental constraints on theories of gravity. From the definition of *overlap* given in Eq. (3.28), we can draw skymaps of relative sensitivity. This has been done in [38] for the three-detector LIGO-Virgo network. We extended the study to the five-interferometer network described previously.

To allow for a comparison with the LIGO-Virgo three-interferometer network, results for both networks are shown in Figs. 3.8 (LIGO-Virgo network) and 3.9 (five-detector network). These are skymaps color coded to highlight regions of the sky in which the tensor and the non-tensor responses are highly distinguishable. Notice that the patterns are anchored to angular locations with respect to Earth (not the fixed stars): in other terms, the shown sensitivity depends only on the the specific location and orientation of the detectors in the considered network. To find the correspondent sky location in the celestial sphere, the sidereal time of arrival of the signal must be taken into account.

For a more detailed quantitative study of the overlap factor, the probability distribution function (over all sky locations) of each overlap is plotted in Figs. 3.10a and 3.10b. The extended network of five detectors (that from now on will be referred as *the network*) is still less sensitive to scalar with respect to vector modes, since the interferometers are individually less sensitive to these; but the sensitivity to the scalar polarization is improved with respect to the three-detector configuration, as it can be seen from the left tail of the distribution that ends one order of magnitude before the other. From this first quantitative analysis, which is exclusively based on the reciprocal position and orientation of detectors, it is already possible to infer that with the addition of two interferometers, the response to non-GR polarization is mostly improved.

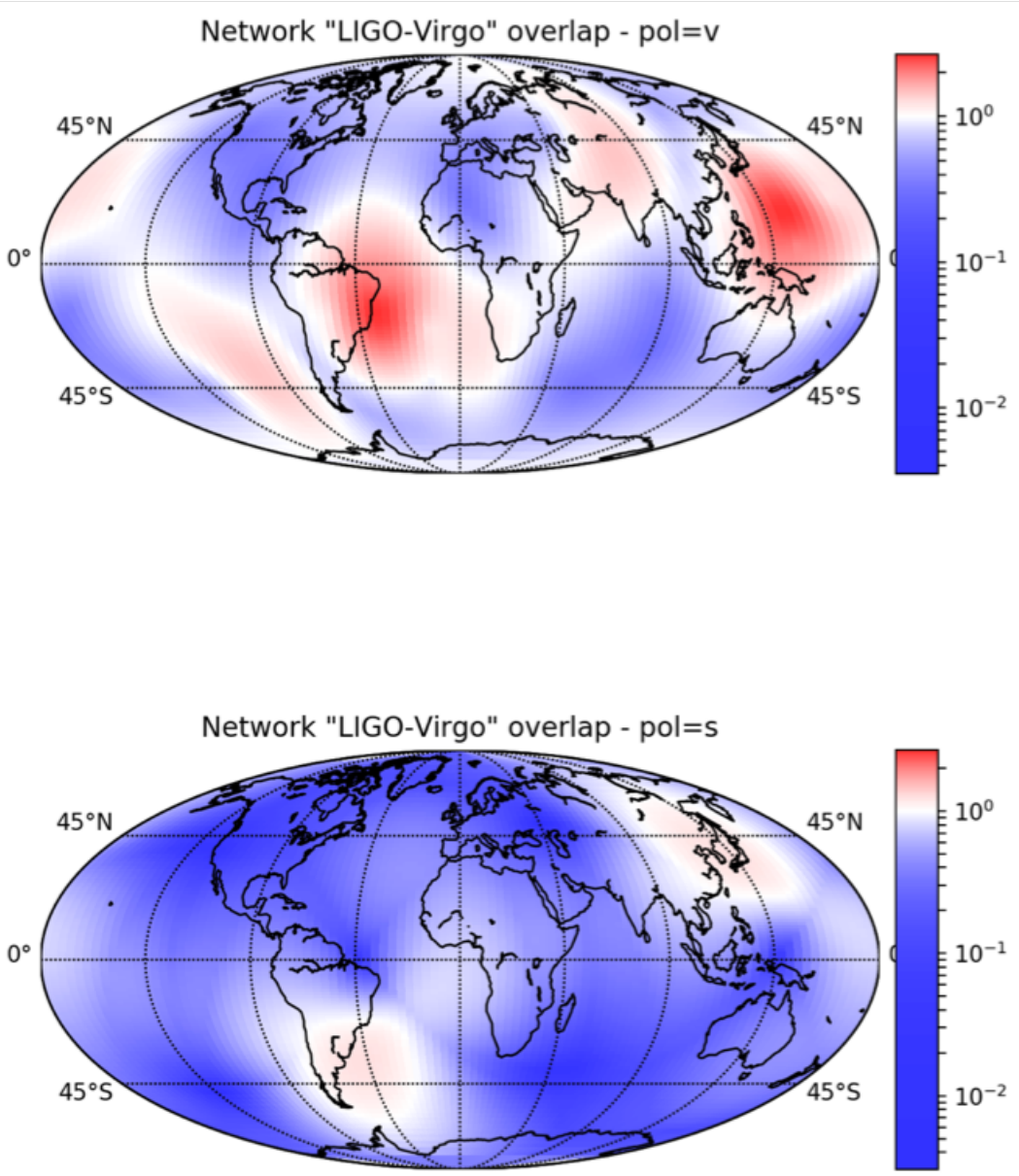

Figure 3.8. *Overlaps of LIGO-Virgo network effective antenna patterns.* The normalized inner-products of Eq. (3.28) for the three-instrument network. The top (bottom) plot compares vector (scalar) to tensor polarizations via the quantity $\mathcal{F}_{v/t}$ ($\mathcal{F}_{s/t}$). Red (blue) marks regions for which the effective non-tensor response is greater (less) than the tensor one. A map of Earth is overlaid for reference.

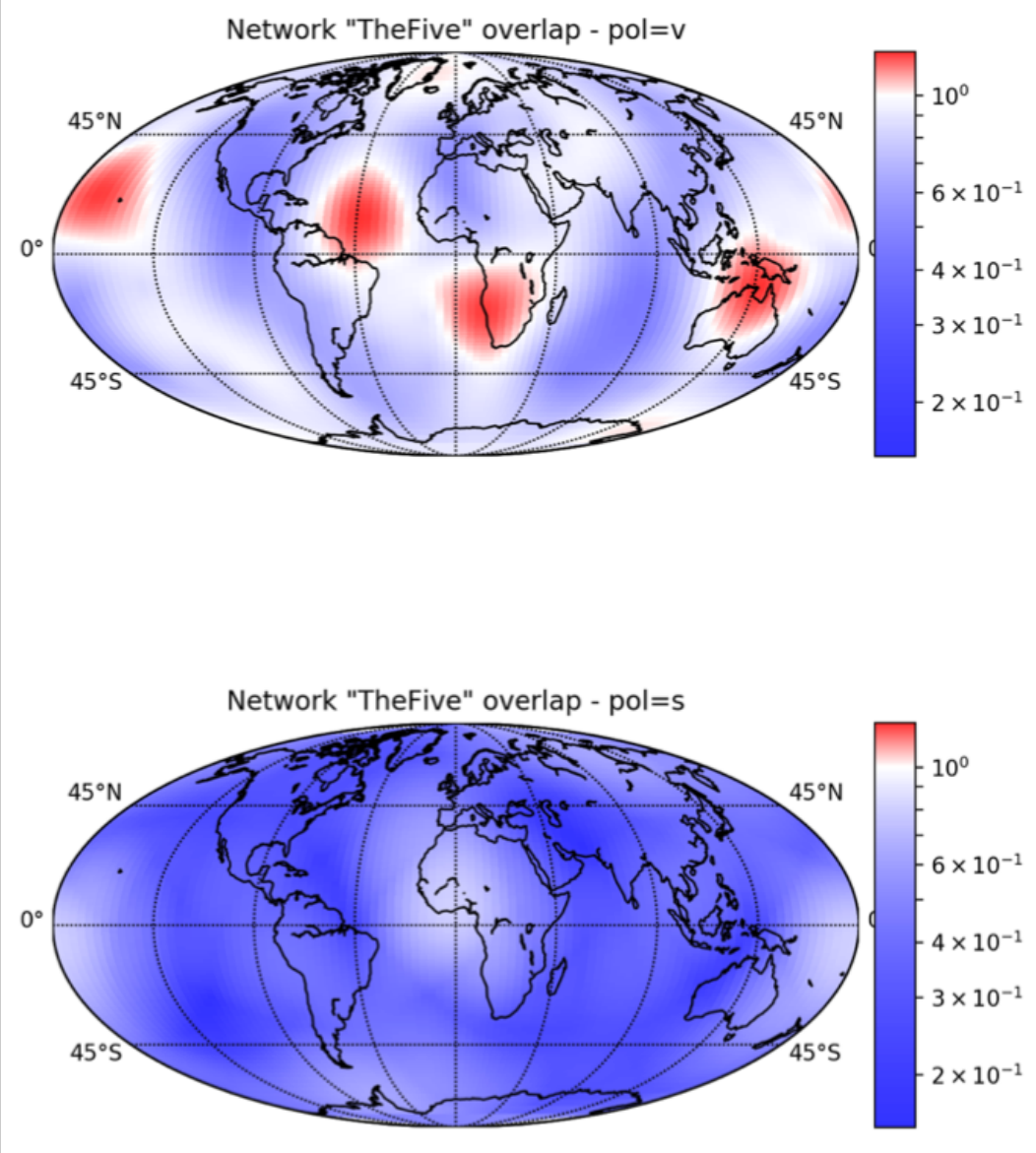

Figure 3.9. *Overlaps of the five-detector network effective antenna patterns.* These plots are equivalent to the ones in Fig. 3.8 but for a GW network that includes KAGRA and LIGO-India.

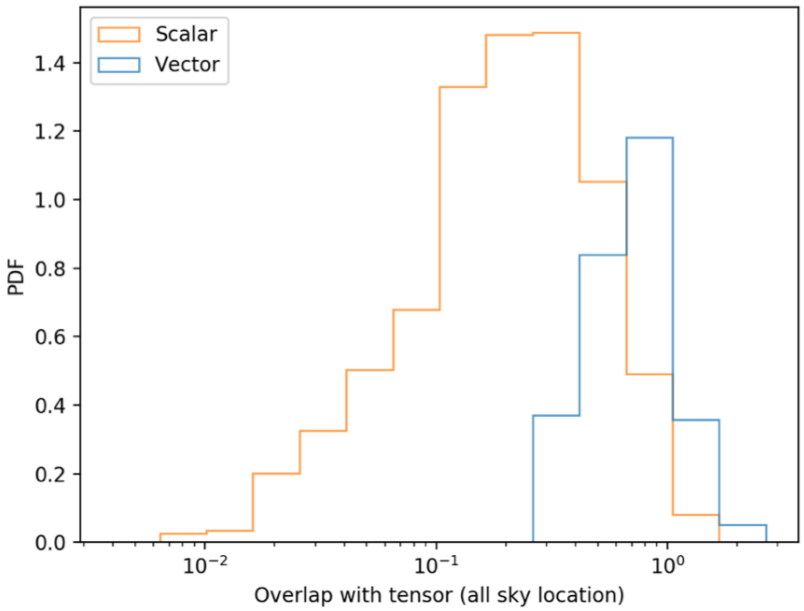

(a) LIGO-Virgo Network

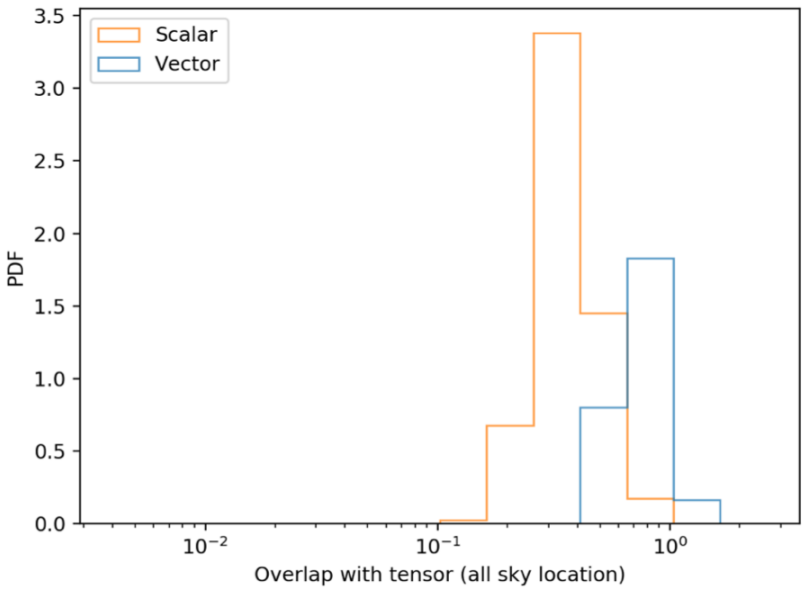

(b) Five-detector Network

Figure 3.10. *Histograms of the probability distribution functions (PDFs) of the overlaps factor.* As it can be seen by the comparison, although the overall scalar sensitivity is still less than the vector one also for the five-detector network (b), it is improved with respect to the LIGO-Virgo network (a) by almost one order of magnitude.

3.4 Model-Independent Polarization Reconstruction

As seen in Sec. 3.2.3, antenna patterns are a direct manifestation of local geometry only (polarizations and detector geometry), independent of the physical details of the source or the underlying theory. We may thus exploit the difference in the response of the network to the various polarizations to infer the polarization content of the wave. There are two ways to extract polarizations from antenna patterns for transient GW signals. We discuss these in the next two subsections.

3.4.1 Null Streams

In the first scenario, the GW signal has an optical counterpart that allows for an accurate determination of its sky position [7]. In this case, it is particularly convenient to look for non-GR signal content by constructing one or more *GR null streams*. These are *directions* in the multidimensional space of the network response (the dimensionality of which is set by the number of detectors) in which there should be no signal if the wave is tensor-only polarized. Indeed, for N detectors, the signal manifold is N-dimensional with N bases vectors, five of which can be chosen along the independent antenna patterns $\{F^i_+, F^i_\times, F^i_x, F^i_y, F^i_s\}$, where the Latin index runs over the N detectors. The remaining $N-5$ vectors will give us null streams, regardless of the polarizations of the wave. The j-th detector datastream can be written in tensor notation as:

$$S^j = F^j_P h^P + n^j \,, \tag{3.29}$$

where n^j is the noise content in the j-th detector. In the case of three detectors, we can define a *GR null stream*, i.e., a stream without tensor modes, in the following way [19]:

$$S_{GR-null} = \frac{e_{ijk} F^j_+ F^k_\times}{|\delta_{ij} F^i_+ F^j_\times|} S^i \,, \tag{3.30}$$

where δ_{ij} is the *Kronecker Delta*, different from zero and equal to one only for $i = j$ while e_{ijk} is the *Levi-Civita Symbol*, different from zero and equal to one only for $e_{123} = 1$ and even permutations of the three indices. Depending on the number of interferometers, we can have more than one null stream, and with more than five, one can construct a complete set of null streams that covers all metric theories of gravity. This method is model independent, but it has the disadvantage of requiring an electromagnetic counterpart.

3.4.2 Sine-Gaussian Expansions

A second method, developed in [20], which does not necessarily require an electromagnetic counterpart is the following: using a sine-Gaussian analysis to reconstruct the waveform, one may infer from the time delays the source location and then the best fitting combination of antenna patterns for the peak in amplitude. This analysis is independent from the phase evolution and it only needs a well-defined

peak (as shown in [38], Sec. III A). A similar approach was recently used in [1] to extract unbiased information from the signal and perform a model-independent GR test. With three interferometers, it is already possible to infer the direction $\mathbf{N}$ of the source in the sky just measuring time delays. It is given by the formula:

$$\delta t_i = \mathbf{N} \cdot \mathbf{x}_i / c \,, \tag{3.31}$$

where δt_i is the time delay with respect to the geocenter and $\mathbf{x}_i$ joins the geocenter to the i-th detector. With four interferometers, constraints on the propagation velocity of GWs can be placed, providing information about the mass of the graviton and, indirectly, on GW polarizations. The key idea is that, in such test, *no polarization information is extracted from the phase evolution*: in other terms, the sine-Gaussian template is only used to infer the source location from the time lag between detectors, and the best-fitting combination of antenna patterns from the amplitudes and phases at peak energy. We chose to adopt this methodology for our research.

Chapter 4

Data Analysis Techniques

This chapter focuses on the most updated data analysis techniques applied to GW Physics. First, a general introduction on random processes and noise is provided, with particular focus on the main sources of disturbance in GW interferometric detectors. In the second section, linear signal processing is described in some detail, and the role of matched filtering for a given-form signal detection is emphasized. The last part is devoted to the development of a Bayesian Inference Framework to deal with GW polarization hypotheses.

4.1 Noise

Chapter 3 introduced the working principles of interferometers: they ought to be extremely sensitive instruments to effectively detect GW. There are many non-gravitational effects that can move the mirrors or affect the laser beam, mimicking a GW detection. Everything that can alter or disturb the interferometer response impeding GW detections is generally called *noise*, as opposed to the *signal*, the GW effect on the instrument.

4.1.1 Random Processes

In most cases, noise is generated by *random processes* that can be controlled in their intensity, but never completely removed. A random process is an *ensemble* of *random variables* $y(t)$ that represent the same physical entity. The $y(t)$, called a *realization* of the process, can be thought of as a (scalar) function of time the future evolution of which cannot uniquely determined *a priori* from any set of initial data. For example, if we take the random walk process in one dimension, each single walker is a realization of it. To make predictions on a random process evolution, we need to know the complete set of *probability distribution functions* $\{p_1(y_1, t_1), \ldots, p_n(y_n, t_n; \ldots; y_1, t_1)\}$, where the subscript n is the number of independent values of y that appear in p_n. The following quantity

$$p(y_n, t_n; \ldots; y_1, t_1) dy_n \ldots dy_1$$

represents the probability that one of the realizations $y(t)$ of the process takes a value in the range $(y_i, y_i + dy_i)$ at each time t_i. To have a complete probabilistic knowledge of the random process, in principle we need an infinite number of probability distribution functions. However, some restrictive hypotheses on the nature of the random process render the computation of the probability distributions a feasible task that involves only a small amount of information.

We define a random process to be *stationary* if and only if the probability distributions depend on time difference, i.e.

$$p(y_n, t_n; \ldots; y_1, t_1) = p(y_n, t_n + \tau; \ldots; y_1, t_1 + \tau)\,. \tag{4.1}$$

This property does not imply a probability distribution *constant in time*, but only that p is independent from any *absolute clock*.

Many (stationary) random processes in Physics are often assumed to be *ergodic*, such that their statistical properties can be deduced from a single, sufficiently long, random sample of the process. In other terms, each specific $y(t)$ of the ensemble, when viewed for sufficiently long times, is representative of the entire process. As a corollary, when the ergodic hypothesis is satisfied, time averages of a random process obtained using a realization $y(t)$ are equal (for sufficiently long times) to ensembles averages (average on the possible realizations of the process). In formulae:

$$\bar{F} \equiv \lim_{T\to\infty} \frac{1}{T} \int_{-T/2}^{T/2} F(y(t)) dt = \langle F(y) \rangle \equiv \int F(y) p_1(y) dy\,, \tag{4.2}$$

where $p_1(y,t_1) = p_1(y,0) \equiv p_1(y)$ for a stationary process.

Another recurrent (but somewhat more restrictive) assumption made to model a random process in Physics comes as a result of one of the most famous theorems in probability theory, the *central limit theorem*. When we have a random process that is the sum of a large number of statistically independent random influences, its probability distribution function becomes *Gaussian*. For a *Gaussian random process*, we can consequently write:

$$p_n(y_n,t_n;\ldots;y_1,t_1) = N\exp\left[-\sum_{j=1}^{n}\sum_{k=1}^{n}A_{jk}(y_j-\bar{y})(y_k-\bar{y})\right], \tag{4.3}$$

where N is a positive renormalization constant, A_{jk} are the elements of a *positive-defined symmetric* matrix, and $\bar{y}$ is the ensemble average of y:

$$\bar{y} = \langle y\rangle = \int y p_1(y)dy\,.$$

We can define $P_n(y_n,t_n|y_{n-1},t_{n-1};\ldots;y_1,t_1)$ as the *conditional probability* of obtaining a value y_n at time t_n if $y(t)$ took the values y_i at times t_i. We can relate it to the absolute probability distribution p, by writing:

$$\begin{aligned} &p_n(y_n,t_n;\ldots;y_1,t_1) = \\ &\qquad = P(y_n,t_n|y_{n-1},t_{n-1};\ldots;y_1,t_1)p_{n-1}(y_{n-1},t_{n-1};\ldots;y_1,t_1)\,. \end{aligned} \tag{4.4}$$

Finally, a random process is said to be *Markov* (or *Markovian*) if and only if all of its future probabilities are determined by its most recently known value, i.e.,

$$P_n(y_n,t_n|y_{n-1},t_{n-1};\ldots;y_1,t_1) = P_2(y_n,t_n|y_{n-1},t_{n-1})\,. \tag{4.5}$$

4.1.2 Power Spectral Density and Noise Classification

Let us define the *power spectral density* (PSD) $S_y(f)$ of a generic random process $y(t)$ as the convergent integral, for positive frequency f:

$$S_y(f) \equiv \lim_{T\to\infty}\frac{2}{T}\left|\int_{-T/2}^{T/2}[y(t)-\bar{y}]e^{2\pi ift}dt\right|^2 \equiv \lim_{T\to\infty}\frac{2}{T}|\tilde{y}_0(f)|^2\,. \tag{4.6}$$

Inside the absolute value we recognize the *Fourier transform*

$$\tilde{y}_0(f) = \int_{-\infty}^{\infty} y_0(t)e^{2\pi ift}dt \tag{4.7}$$

of the zero-mean random variable $y(t)-\bar{y}$, assuming a truncation in the time domain of the function to regularize divergences in the Fourier integral computation, i.e.

$$y_0(t) \equiv \begin{cases} y(t)-\bar{y} & \text{if } -T/2 < t < +T/2\,, \\ 0 & \text{otherwise.} \end{cases} \tag{4.8}$$

The mean value was subtracted to avoid a delta function in $S_y(f)$ at zero frequency.

Let σ_y^2 be the *variance* of the random variable $y(t)$, defined as the average value (on time) of the squared deviations with respect to its mean value $\bar{y}$. Using the definition of average value on time given in Eq. (4.2) and the definition of $y_0(t)$ of Eq. (4.8), it follows that:

$$\sigma_y^2 \equiv \overline{(y(t)-\bar{y})^2} \equiv \lim_{T\to\infty} \frac{1}{T}\int_{-T/2}^{T/2} (y(t)-\bar{y})^2 dt = \lim_{T\to\infty} \frac{2}{T}\int_0^{\infty} |y_0(t)|^2 dt\,. \tag{4.9}$$

By the virtue of Plancherel's theorem (see [12] for details), the integral of the squared modulus of a function is equal to the integral of the squared modulus of its Fourier transform. Therefore, from Eqs. (4.6) and (4.9) we can write:

$$\int_0^{\infty} S_y(f)df = \lim_{T\to\infty} \frac{2}{T}\int_0^{\infty} |\tilde{y}_0(f)|^2 df = \lim_{T\to\infty} \frac{2}{T}\int_0^{\infty} |y_0(t)|^2 dt = \sigma_y^2\,. \tag{4.10}$$

Thus, the integral of the power spectral density of y over all positive frequencies is equal to the variance of y. The PSD has units of

$$[S_y(f)] = \frac{[y^2]}{[f]} = \frac{[y^2]}{\mathrm{Hz}} = [y^2]\cdot \mathrm{Hz}^{-1}\,.$$

To grasp the physical meaning of the object just defined, it is useful to illustrate its application to GW detection. Interferometers are capable of very sensitive measurements of length variation: their output can be thought of in units of length. However, a lot of phenomena different from GWs can produce similar output, generally called *noise*. As we said at the beginning of this section, *noise* is the outcome of many random processes that add up together. A brief overview of the noise sources in a typical GW detector is given in the following subsection.

Let assume that the noise can be described by a random variable $n(t)$, expressed in units of length (as the signal we want to measure). We usually consider data on a finite interval of time. Subtracting the mean value from the noise — usually connected to some systematic — we find a variable which has all the characteristics of $y_0(t)$ we defined earlier. We can then name the PSD of the detector as the Power Spectral Density of its noise, $S_n(f)$. When there is no signal, the PSD can be measured from the Fourier transform of the interferometer response function, applying Eq. (4.6).

If we now filter the interferometer response Fourier transform so that only a specific portion at frequency f, in a very narrow bandwidth Δf, gets through the filter, then the variance of the filtered response will be the portion of integral of Eq. (4.10) coming from this frequency band, i.e. $S_n(f)\Delta f = \sigma_n^2(f)$. In other terms, the *root mean square* of the noise oscillations at frequency f in a very narrow bandwidth Δf is given by $\sqrt{S_n(f)\Delta f}$. The PSD gives us a *colored noise*: it measures noise in the frequency space and it allows us to distinguish between background and signal.

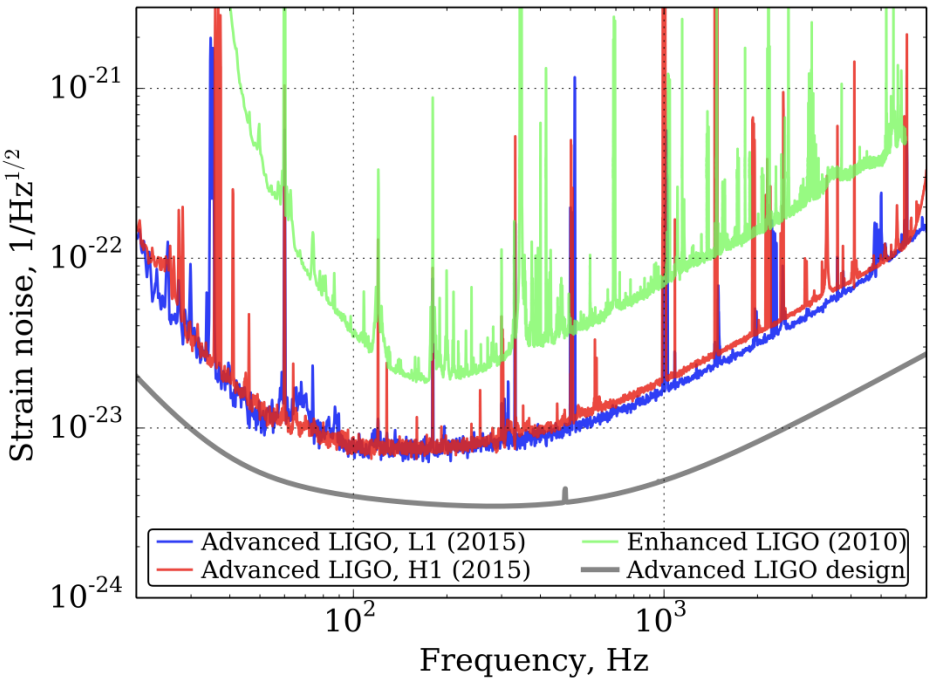

Figure 4.1. *Amplitude Spectral Density of LIGO detectors noise.* Gravitational wave signals with amplitudes lower than this noise floor are too quiet for the interferometers to detect. The sensitivity of the Advanced LIGO detectors in the first observing run (September 2015 to January 2016) was about a factor of three better than the instruments that collected data, in 2010. In the next few years, LIGO scientists will work to reduce the detector noise to the lowest achievable level with the current hardware (the *design sensitivity* of the detectors). The narrow spectral lines (sharp spikes in the spectrum produced by internal resonances in the instrument) contain negligible power, and so can be ignored for our purposes. At high frequencies, $f \gtrsim 150\,\mathrm{Hz}$, the noise is due to randomness in arrival times of photons used to measure the mirror motions (*photon shot noise*). At intermediate frequencies, $40\,\mathrm{Hz} \lesssim f \lesssim 150\,\mathrm{Hz}$, it is primarily *thermal noise*. At low frequencies, $f \lesssim 40\,\mathrm{Hz}$, it is primarily due to mechanical vibrations that sneak through The vibration isolation system (*seismic noise*). (Reproduced from [43].)

In GW detectors, what is commonly used to model the instrumental noise is the *Amplitude Spectral Density* (ASD), which is equal to the square root of the PSD normalized over the length of the effective path travelled by laser beams. It is measured in $1/\sqrt{\text{Hz}}$ units and it can be directly compared with the Fourier transform of the dimensionless perturbation of the metric $\tilde{h}(f)$ at a specific frequency, often called the *strain* of the incoming GW. At a given frequency, the predicted GW perturbation could be seen by the detector only if it were greater than the ASD. In Fig. 4.1 we report the measured and designed sensitivity of the LIGO interferometers at different stages of their evolution.

In experimental Physics, noise usually takes a specific name based on the shape of its spectrum (the f dependence of $S_n(f)$). Some of the most common behaviour often encountered in experiments are the following:

- *White Noise:* S_n is independent of f. It is called *white* because it has equal amounts of power per unit frequency at all frequencies, just like white light that is the result of the combination of equally intense different colors (frequencies). A quasi-white noise source is given by *thermal noise* (also called *Johnson–Nyquist noise*), the electronic noise generated by the thermal agitation of the charge carriers (usually the electrons) inside an electrical conductor at equilibrium, which happens regardless of any applied voltage.
- *Pink Noise* or *Flicker Noise:* $S_n \propto 1/f$. It takes its name from the fact that at any time scale, the noise seems to be periodic with one, two, or three oscillations , with amplitudes independent of the chosen time interval. This kind of noise is very common in Physics: it mainly occurs at low frequency in electronics, geophysics and astrophysics.
- *Random-walk Noise:* $S_n \propto 1/f^2$. A Gaussian-Markov process such *Brownian Motion*, i.e. the time evolving position $x(t)$ of a dust particle buffeted by air molecules in a large, constant-temperature room has this kind of spectrum.

4.1.3 Typical Noise Sources for Gravitational-Wave interferometers

We now give some examples of the main sources of noise in a GW detector, following [43].

- *Seismic noise.* Mainly due to ground vibrations generated by earthquakes, wind, ocean waves, and human activities. Several techniques were developed to insulate the mirror system from the ground motion, but this is still one of the greatest sensitivity limitations for ground-based interferometers.
- *Thermal noise.* Caused by microscopic fluctuations of the individual atoms in the mirrors and their suspensions. Cryogenic techniques were implemented to limit this source in the KAGRA detector (see [10] for a detailed overview).

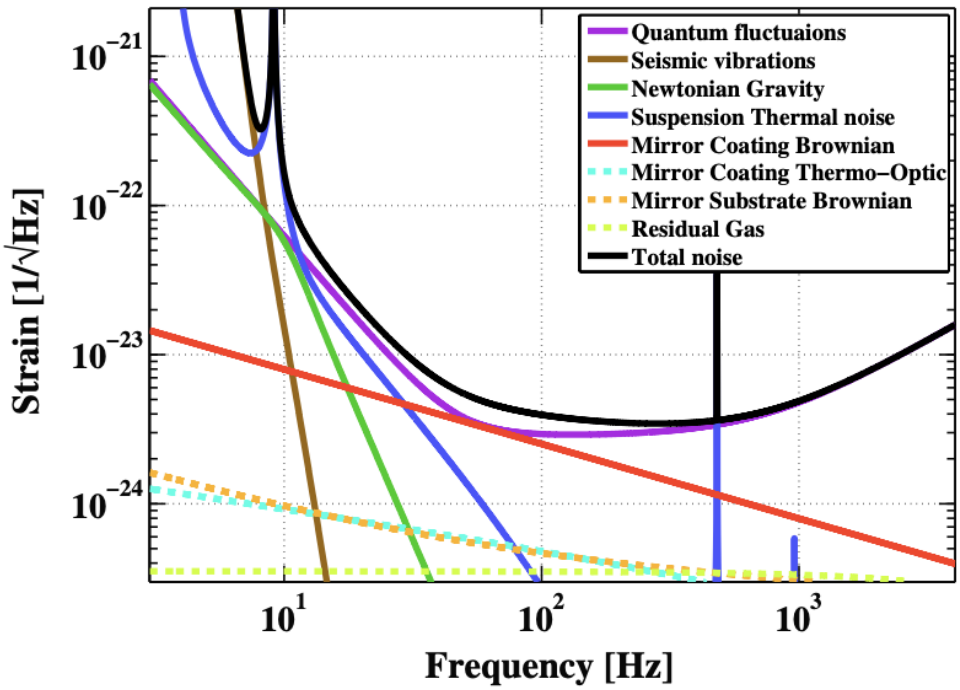

Figure 4.2. *ASD of Advanced LIGO noise budget.* (Reproduced from [9].)

- *Quantum noise.* The intrinsically statistical uncertainty due to the discrete nature of photons (light quanta) prevents from an exact measure of the transmitted light by photodetectors.
- *Gas noise.* Although the arms of the interferometers operate under a full vacuum, there can be residual gas particles in the vacuum enclosure and these may interact with the mirrors and the laser light producing disturbances in the response.
- *Charging noise.* Static electric charges on the glass mirror and their interactions with the metal of the vacuum enclosures and the mirror supports are another source of noise.
- *Laser noise.* Laser stability plays a significant role in limiting small variations of intensity and frequency, that can be misinterpreted as potential signals.
- *Auxiliary degree-of-freedom noise.* Mainly due to position and alignment of the various mirror in the detectors.
- *Oscillator noise.* Generated by the radiofrequency modulation of the laser light.
- *Beam jitter.* Slight variations in the position and angle of the laser beam in the tube can cause a misalignment of the laser beam with respect to the optical cavities.

- *Scattered light.* Spurious signals in the photodetectors can be generated by the light scattered by imperfections in the mirrors.
- *Electronics noise.* Every analog measurement is converted into a digital signal through a huge electronics sector which can give contributions to the noise budget.

Figure 4.2 reports the Advanced LIGO noise budget (its ASD). Single contributions from some of the sources we discussed are superimposed.

4.2 Matched Filter and Signal-to-Noise Ratio

In experimental physics, as well as in engineering, very often a random process is mixed with the signal we want to measure. Therefore, we need to apply some strategy to isolate the signal within the raw data, distinguishing it from the noisy background. In this Section, we develop the fundamental tools that allow for a *filtering* of the noisy data, in order to make the detection of a signal buried in noise possible. These techniques are encompassed in the theory of *linear signal processing*.

4.2.1 Filters, Kernels and Signal-to-Noise Ratio

Given a *realization*) $y(t)$ of a *stationary* random process, we define a *filter* to be a *linear functional* $W(t)$ of the variable $y(t)$ such that:

$$W(t) = \int_{-\infty}^{+\infty} K(t-t')y(t')\mathrm{d}t' \,, \tag{4.11}$$

where $K(t-t')$ is the *stationary* filter's *kernel*. Using the *convolution theorem*, we can write the Fourier transform of the filter — which is technically a convolution integral — as the pointwise product of the variable and the kernel Fourier transforms, $\tilde{y}(f)$ and $\tilde{K}(f)$. In formulae,

$$\tilde{W}(f) = \tilde{K}(f)\tilde{y}(f) \,. \tag{4.12}$$

If we now compute the PSD of the filter functional, applying Eq. (4.6), we find that:

$$S_W(f) = |\tilde{K}(f)|^2 S_y(f) \,, \tag{4.13}$$

where $S_y(f)$ is the PSD of the random variable $y(t)$. Applying a filter modifies the PSD of the response, allowing us to remove noise in favor of the signal. The choice of the kernel is crucial for the purposes of every specific analysis.

As an example, we can examine the *band-pass filter*. Suppose we have a monochromatic weak signal of frequency f_0 buried in some noise $n(t)$. The total process will be described by

$$r(t) = \sqrt{2}A_s \sin(2\pi f_0 t + \delta_0) + n(t) \,, \tag{4.14}$$

where A_s is the signal amplitude, δ_0 its phase offset and the factor $\sqrt{2}$ is added for later convenience. Although the noise is an impediment to the signal detection, we can send $r(t)$ through a *band-pass filter* centered in f_0 and with bandwidth

$$\Delta f \equiv \frac{\int_0^\infty |\tilde{K}(f)|^2 \mathrm{d}f}{|\tilde{K}(f_0)|} \ll f_0 \,. \tag{4.15}$$

The output of a band-pass filter has the general form:

$$W(t) = \sqrt{2}|\tilde{K}(f_0)|A_s \sin(2\pi f_0 t + \delta_1) + w(t) \,, \tag{4.16}$$

where the first term is the filtered signal, still monochromatic but with a re-scaled amplitude and a different phase δ_1, while the second term is the filtered noise. If we suppose that the noise PSD fluctuates negligibly over the small bandwidth, i.e. $S_n(f) = S_n(f_0)$, using Eq. (4.13), we find that:

$$S_w(f) = |\tilde{K}(f)|^2 S_y(f_0) \,. \tag{4.17}$$

The filtered noise $w(t)$ is then a superposition of sinusoids all with nearly the same frequency f_0, with a frequency spread large as the bandwidth Δf. This kind of functions is known from acoustic to produce *beats*: the sum of two sinusoids with a small difference in frequency Δf around f_0 is an f_0 sinusoid with amplitude modulated over a period of $\Delta t = 1/\Delta f$. Consequently, the filtered noise will be of the form:

$$w(t) = w_0(t)\cos[2\pi f_0 t + \phi(t)] \,, \tag{4.18}$$

a sinusoidal function at frequency f_0 but with amplitude $w_0(t)$ and phase $\phi(t)$ randomly fluctuating on timescales Δt. This makes the signal distinguishable from the noise.

In the context of filters, the *Signal-to-Noise Ratio* (SNR) plays a special role. This is a mathematical object that tells us how strong the signal is compared to the noise it sits in. It is defined as the ratio between the *root mean square* of the filtered signal over the root mean square of the noise. For a band-pass filter, we have a root mean square output signal equal to

$$S \equiv |\tilde{K}(f_0)|A_s \,,$$

(the factor $\sqrt{2}$ simplifies with the root mean square of the sine function) and a root mean square output noise of

$$N \equiv \left[\int_0^\infty S_w(f)\mathrm{d}f\right]^{\frac{1}{2}} = |\tilde{K}(f_0)|\sqrt{S_n(f_0)\Delta f} \,.$$

Consequently, the SNR will be:

$$\frac{S}{N} = \frac{A_s}{\sqrt{S_n(f_0)\Delta f}} \,. \tag{4.19}$$

Therefore, the narrower the filter bandwidth is, the more accurate the measurement of the signal will be (provided that the bandwidth includes the frequency f_0 of the signal).

4.2.2 Matched Filter

Often the signal one seeks amidst noise is not sinusoidal but has some other known form $h(t)$. In this case, the optimal way to search for it is with a so-called *Matched filter* (or *Wiener filter*, a generalization of the band-pass filter), which will be described in the following subsection.

We can imagine our response $d_I(t)$ at each detector I as a superposition of a pure signal $h(t)$ and the noise $n_I(t)$, described by a specific power spectral density $S_n^I(f)$ at each detector. In formulae:

$$d_I(t) = h_I(t) + n_I(t)\,, \tag{4.20}$$

$$S_n^I(f) = \lim_{T\to\infty} \frac{2}{T}\left| \int_{-T/2}^{T/2} n_I(t) e^{2\pi i f t} dt \right|^2 . \tag{4.21}$$

We are looking for a filter $W(t)$ that can isolate the signal from the noisy background. Let's suppose we have the *template*, that is, the predicted waveform, for $h(t)$. It can be shown (for details, see [66], Ex. 6.12) that W will be maximally sensitive to the signal if we use as the filter kernel $K(t)$ the inverse Fourier transform of the following:

$$\tilde{K}(f) = \frac{4\tilde{h}(f)}{S_n(f)}\,, \tag{4.22}$$

where $\tilde{h}(f)$ is the Fourier transform of the signal template.

This last object is called *Matched Filter* or *Wiener's optimal filter*. By virtue of Plancherel's theorem, we can compute integral norms both in time and in frequency domain, obtaining the same result, since the Fourier transform is a unitary linear operator. We can now define the SNR of this filter to be:

$$\rho(t) = \frac{\langle h|d\rangle}{\sqrt{\langle h|h\rangle}}\,, \tag{4.23}$$

where we used the notation $\langle h|s\rangle$ for the following scalar product (Re stands for the real part)

$$\langle h|d\rangle = 4\mathrm{Re}\int_0^\infty \frac{\tilde{h}^*(f)\tilde{d}(f)e^{2\pi i f t}}{S_n(f)} df\,. \tag{4.24}$$

As already stated, the SNR, which is a function of time, measures how well we can distinguish the signal (and then extrapolate its waveform) from a noisy background. From Eq. (4.24), it seems necessary to know in advance the *template* $h(t)$ for the signal in order to recover the highest possible SNR value and to see the signal itself. However, it is worth pointing out that this analysis can be carried out also in a model-independent way, using for example a basis of sine-gaussian waveforms to reconstruct the signal (see Sec. 3.4.2).

An example of a noisy response for the simulated signal described in the next chapter is shown in Fig. 4.3a and the SNR time series $\rho(t)$ is shown in Fig. 4.3b. In the following, we will call the maximum of the function $\rho(t)$ for each signal the SNR of the event. Notice that for a pure noise signal, $\rho(t)$ oscillates randomly in the interval $[0, 3]$. Usually, an event is considered a signal candidate when it has a SNR of at least 8.

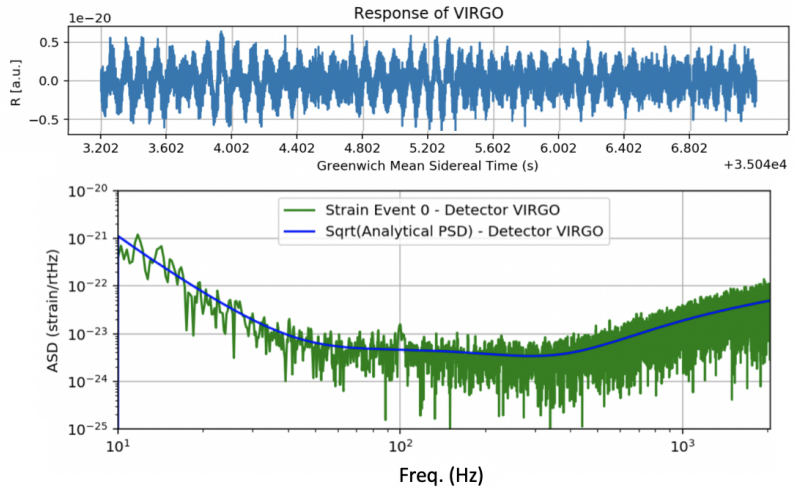

(a)

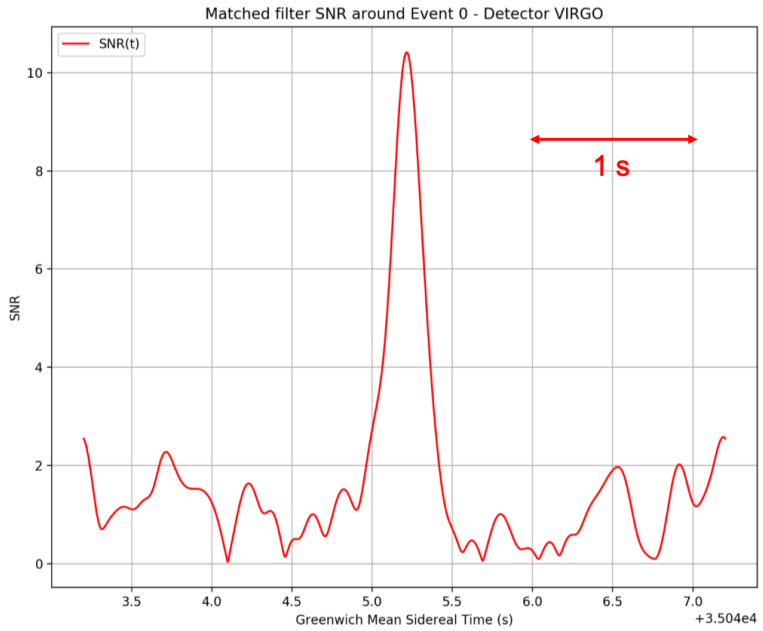

(b)

Figure 4.3. *Example of a simulated GW noisy response of the Virgo detector with its strain in frequency space (a) and time evolution of the SNR of the response (b).* The waveform used is described in the next chapter. The signal is not distinguishable by eye in time domain, but its strain in the frequency domain (the square root of the PSD of the full response) reported in the second plot shows a little bump at $100\,Hz$, the frequency chosen for the sine-gaussian. As a comparison, we also plot the square root of the analytical PSD used to generate the noise. Notice that, since the total length of the signal in time is $4\,s$, the Discrete Fourier Transform has a maximum resolution in frequency of $T^{-1} = 0.25\,Hz$. As expected, the SNR shows a peak for the time of arrival of the wave.

4.3 Bayesian Framework

In this section, we develop the tools that are necessary to analyze GW signals within a *Bayesian framework*. After a brief introduction on the two most used statistical inference methods in Physics, the Bayesian approach is presented in depth. We then specialize it to the problem of our interest, namely the measurement of GW polarizations, finding the explicit general form of the likelihood for a network of interferometers. Finally, we provide details on the algorithm used to efficiently explore the parameter space.

4.3.1 Statistical Inference Methods

In Science, a variety of *statistical inference methods* are used to extract from the data the properties of underlying probability distributions and, ultimately, to test theoretical hypotheses in light of the experimental evidence. One of the fundamental principles of experimental Science is the *reproducibility* (also called *test-retest reliability*) of an experiment, which is the closeness of the agreement between the results of successive measurements of the same observable carried out under the same conditions. This axiom, which relies on the existence and persistence of laws of Physics, led to the development of *frequentist inference*, a framework in which statistical hypotheses are tested and *confidence* intervals are determince. The core of this method can be summarized as follows. Through the conduction of a set of experiments, multiple random samples can be taken from the underlying probability distribution. If the underlying probability distribution depends on a set of parameters, then these parameters are considered to be fixed quantities that remain constant during the experiments. It is simply because we can only sample noisy instances of the truth that the true parameters remain hidden from our eyes. A large number of experiments will remove this noise and allow us to estimate the underlying parameters.

However, in GW Physics we do not have the power to set the parameters at the beginning of our experiment, so it is impossible to conduct the same experiment with similar initial conditions. Then, to handle this kind of problems, a different and more flexible framework is of paramount importance: the *Bayesian inference method*. One of the main differences between the two methods is its ability of the latter to include *prior* beliefs (in the form of probability distributions) about the parameter values that reflects a previous knowledge of the phenomenon. The probability distributions are then updated in light of the (new) data: the outputs of a Bayesian inference method are probability distributions (called *posteriors*) for the parameters of the model. Furthermore, one of the greatest advantages of this method is that, instead of yielding a discrete "true/false" value for the initial hypothesis within a certain confidence interval as the frequentist method does, it can be used to quantitatively compare different hypotheses and operate a model selection, assigning to each one a continuous probability of being the correct one. In summary, Bayesian statistics views the data as fixed and the underlying parameters as variable while frequentist statistics assumes that the underlying parameters are fixed and various experiments with a random component can be conducted.

4.3.2 Bayes' Theorem

The term *Bayesian* refers to the English statistician *Thomas Bayes (1702–1761)*, who proved that probabilistic limits could be placed on an unknown event. However, the probability theorem that takes his name was formally introduced by the French scholar *Pierre-Simon Laplace (1749–1827)* in his 1812 book *Théorie analytique des probabilités*. At the core of Bayesian inference is *Bayes' theorem*, which can be written as the following equation:

$$P(A|B) = \frac{P(B|A)P(A)}{P(B)}\,. \tag{4.25}$$

It states that the *conditional probability* $P(A|B)$ for the event A given the event B (i.e., the likelihood of event A occurring given that B is true) is given by the inverse conditional probability $P(B|A)$ multiplied by the ratio of the *marginal probabilities* $P(A)$ and $P(B)$ of observing A and B, respectively.

We can divide the task of using Bayes' Theorem to analyze a set of data $\mathbf{D}$ into two problems: parameters estimation and model selection.

Parameters estimation — Given a specific model $\mathcal{H}$ of our data which depends on a set of parameters $\boldsymbol{\theta}$, we can recover the joint *posterior* probability distribution function on the multidimensional space of parameters $P(\boldsymbol{\theta}|\mathcal{H}, \mathbf{D})$ as:

$$P(\boldsymbol{\theta}|\mathcal{H}, \mathbf{D}) = \frac{P(\mathbf{D}|\mathcal{H}, \boldsymbol{\theta})P(\boldsymbol{\theta}|\mathcal{H})}{P(\mathbf{D}|\mathcal{H})}\,. \tag{4.26}$$

This is an application of Bayes' Theorem, where:

- $P(\mathbf{D}|\mathcal{H}, \boldsymbol{\theta})$ is the *likelihood*, the core of the computation, a measure of how well our model with chosen parameters can describe the data observed;
- $P(\boldsymbol{\theta}|\mathcal{H})$ is the (multidimensional) *prior* of our model, a joint probability distribution function that weighs the parameter space according to our previous knowledge on the phenomenon;
- $P(\mathbf{D}|\mathcal{H}) = \int_{\boldsymbol{\Theta}} P(\mathbf{D}|\mathcal{H}, \boldsymbol{\theta})P(\boldsymbol{\theta}|\mathcal{H})d\boldsymbol{\theta}$, often indicated by $\mathcal{Z}$, is the *evidence*, the likelihood integrated over the whole parameter space (weighted by the prior), which works as a normalization factor in this context, but is crucial in the context of model selection, as we will see shortly.

Model selection — We can also use Bayes' theorem to assign a statistical significance to a model compared with another, deciding which of several models is more probable in light of the observed data $\mathbf{D}$, and by how much. This may be done by considering the ratio of posterior probabilities obtained using two different models $\mathcal{H}_i$ and $\mathcal{H}_j$, defining the *odds* for $\mathcal{H}_i$ versus $\mathcal{H}_j$ as:

$$\mathcal{O}^i_j = \frac{P(\mathcal{H}_i)}{P(\mathcal{H}_j)}\frac{P(\mathbf{D}|\mathcal{H}_i)}{P(\mathbf{D}|\mathcal{H}_j)} = \frac{P(\mathcal{H}_i)}{P(\mathcal{H}_j)}\mathcal{B}^i_j\,. \tag{4.27}$$

In the last equation, we introduced the definition of *Bayes factor* $\mathcal{B}^i_j$, which is the ratio of the two evidence integrals for $\mathcal{H}_i$ and $\mathcal{H}_j$.

Since the XIV century, a problem-solving principle has driven the progress of rational thinking: *Occam's razor*. The idea is attributed to the English scholastic philosopher *William of Ockham (c. 1287–1347)*, whose words are:

> *Entia non sunt multiplicanda præter necessitatem*,
> (Entities should not be multiplied without necessity.)

This philosophical razor advocates that, when presented with competing hypotheses about the same prediction, one should select the solution with the fewest assumptions. In other words, simple models must be favored over more complex ones. Bayesian model selection automatically takes into account an intrinsic *Occam factor* via the Bayes odds we just defined. Simple models tend to make precise predictions. Complex models, by their nature, are capable of making a greater variety of predictions. So, if $\mathcal{H}_i$ is a more complex model, it must spread its predictive probability $P(\mathbf{D}|\mathcal{H}_i)$ more thinly over the data space compared to $\mathcal{H}_j$, reducing the evidence normalization integral with respect to the $\mathcal{H}_j$. Thus, when the data are compatible with two theories, the simpler one will turn out to be more probable, without the need of expressing our subjective dislike for complex models.

4.3.3 Bayesian Hypotheses on the Gravitational-Wave Polarization Content

Summarizing the work carried out by Isi and collaborators in [37], given a vector of responses $\mathbf{D}$ of our network, we want to test seven possible Bayesian hypotheses regarding the polarization content of $\mathbf{D}$: it is purely tensor ($\mathcal{H}_t$), it is purely vector ($\mathcal{H}_v$), it is purely scalar ($\mathcal{H}_s$), it is a scalar-tensor combination ($\mathcal{H}_{st}$), it is a vector-tensor combination ($\mathcal{H}_{vt}$), it is a scalar-vector ($\mathcal{H}_{sv}$) combination, it is a scalar-vector-tensor ($\mathcal{H}_{svt}$) combination. Using Bayes's theorem, we can expand the probability $P(\mathcal{H}_S|\mathbf{D})$ that, given the data, a signal hypotheses S can be accepted:

$$P(\mathcal{H}_S|\mathbf{D}) = \sum_m \frac{P(\mathcal{H}_m)P(\mathbf{D}|\mathcal{H}_m)}{P(\mathbf{D})}\,, \tag{4.28}$$

where $m \in \{t, v, s, st, vt, sv, svt\}$, $P(\mathcal{H}_m)$ is a prior on the model, $P(\mathbf{D}|\mathcal{H}_m)$ is the marginalized likelihood, and $P(\mathbf{D})$ is an overall normalization constant. We can then define the *odds* of detecting a non purely tensor signal as:

$$\mathcal{O}^{nt}_t = \sum_{m\neq t} \frac{P(\mathcal{H}_m)}{P(\mathcal{H}_t)}\mathcal{B}^m_t \tag{4.29}$$

There is a subtle difference between a generic tensor signal and a GR signal for a compact binaries coalescence, which is relevant only if we know *a priori* the inclination of the source within the tri-axial GR model. An extended study of this difference can be found in Appendix A of [37]. Besides choosing among different models, we can use Bayesian statistics to obtain the posterior probability density function on the parameters of a given template for the waveform, provided that we define correctly all the contributions that appear in Eq. (4.26).

4.3.4 The likelihood

The function we choose to be our *likelihood* plays a crucial role. This has to be maximized in order to find the most suitable values for the model parameters to reflect the data. The two following assumptions on the noise (as described in Sec. 4.1) must be made for each detector:

- *it is stationary:* the PSD $S_n(f)$ is constant in time;
- *it is Gaussian:* in each frequency bin, noise is characterized by a zero mean normal distribution with known variance, estimated from $S_n(f)$.

Then, following [69], the *likelihood* function for the model $\mathcal{H}$ of parameters $\boldsymbol{\theta}$, given the detector response as in Eq. (4.20), is simply the product of Gaussian distributions in each frequency bin with adjusted mean value due to the presence of the signal:

$$P(d|\mathcal{H},\boldsymbol{\theta};S_n(f)) = \exp\sum_j \left[-\frac{2\left|\tilde{h}_j(\boldsymbol{\theta}) - \tilde{d}_j\right|^2}{TS_n(f_j)} - \frac{1}{2}\log\frac{\pi T S_n(f_j)}{2}\right], \tag{4.30}$$

where

$$\tilde{d}_j(f) = \frac{T}{N}\sum_k d_k e^{-2\pi i j k f}\,. \tag{4.31}$$

is the Discrete Fourier Transform (DFT) of the response (the index k runs over time and depends on the chosen sampling frequency, N is the total number of samples, T is the total length in time of the response) and $\tilde{h}$ is the discrete Fourier transform of the template, at given parameters $\boldsymbol{\theta}$. To understand the meaning of this functional form, we first point out that the likelihood is *maximized* in correspondence of the most probable values for the parameters of the model in light of the data. Assuming the parameters we choose to fix when building the template correctly reproduce the data, when we subtract in the frequency domain the template of the signal from the data, we should recover in each specific bin only the noise contribution (Fourier transformed). We assumed that the noise is both stationary and Gaussian. Then, using Eq. (4.6), we observe that the fraction in the first term is minimized (maximizing the exponential) when a pure Gaussian noise of variance $S_n(f_j)$ is left in each bin. The procedure of dividing by the PSD in the frequency domain is sometimes called *data whitening*.

To analyze a network of detectors *coherently*, we make the additional assumption that the noise in the detectors is uncorrelated. This allows us to write the coherent network likelihood for data obtained from each detector as the product of the likelihoods in each detector I:

$$P(\mathbf{d}|\mathcal{H},\boldsymbol{\theta}) = \prod_I P(d_I|\mathcal{H},\boldsymbol{\theta};S_n^I(f)) \tag{4.32}$$

4.3.5 Exploring the Parameter Space: the Nested-sampling Algorithm

One of the main challenges of Bayesian inference, that constituted for decades an obstacle for the development of the framework, resides in the high computational cost of the objects we defined as its ingredients, which are integrals over the multidimensional parameter space. An efficient way to explore the parameter space is therefore needed, the so-called *Bayesian sampler*. This is an algorithm that progressively maximizes the likelihood, avoiding local maxima. One of the algorithms used for GW data analysis is Skilling's *Nested-sampling* [62]. The key idea of Nested-sampling is to numerically compute the evidence, by reducing it to a one-dimensional integral, defining the variable change in a proper way. Posteriors on parameters can then be determined with a minimal computational cost. We now summarize the main features of this algorithm.

As the prior and posterior are by definition normalized (since they are probability distributions), the magnitude of the evidence is governed by the likelihood function, that can be thought of as a measure of how well the data fits the hypothesis $\mathcal{H}$. We recall this quantitiy is defined by the multi-dimensional integral

$$\mathcal{Z} \equiv P(\mathbf{D}|\mathcal{H}) = \int_{\mathbf{\Theta}} P(\mathbf{D}|\mathcal{H}, \boldsymbol{\theta}) P(\boldsymbol{\theta}|\mathcal{H}) d\boldsymbol{\theta} \,. \tag{4.33}$$

Although we assume the parameter space $\mathbf{\Theta}$ to be a continuous manifold, and the likelihood to be a smooth function of the parameters $\boldsymbol{\theta}$, if the integral is not solvable analytically, we can approximate its value using a finite set of points. The Nested-sampling algorithm is actually a general method of numerical integration that can be applied to other continuous integrals. A stochastic sample of N *live points*, denoted by $\boldsymbol{\theta}_a$ ($a \in \{1, \ldots, N\}$) is chosen such that the evidence integral can be approximated as the following:

$$\mathcal{Z} \simeq \sum_{i=1}^{N} L_i w_i \,, \tag{4.34}$$

where $L_a \equiv P(\mathbf{D}|\mathcal{H}, \boldsymbol{\theta}_a)$ is the likelihood value at $\boldsymbol{\theta}_a$, and the *weight*

$$w_a = P(\boldsymbol{\theta}_i|\mathcal{H}) \mathrm{d}\boldsymbol{\theta} \tag{4.35}$$

is the fraction of the prior distribution represented by the a-th sample.

The key passage in Nested-sampling is the computation of such weights for stochastic samples. Each starting point $\boldsymbol{\theta}_a$ is thought to be lying on a contour of equal likelihood in parameter space. If we consider each contour as delimiting the part of the parameter space with greater likelihood, we have sliced $\mathbf{\Theta}$ into *nested* volumes of increasing likelihood. We now proceed by following iterations. We first define the *prior mass* X_i to be the fraction of the total prior volume enclosed by the i-th contour. Since the likelihood is maximized (if data are present) in a small part of the parameter space, the lowest likelihood line will enclose the largest volume. By definition, $X_0 = 1$. We can then think of a mapping between the contour lines in $\mathbf{\Theta}$ and the prior masses X_i, such that the likelihood $L(X)$ increases toward smaller

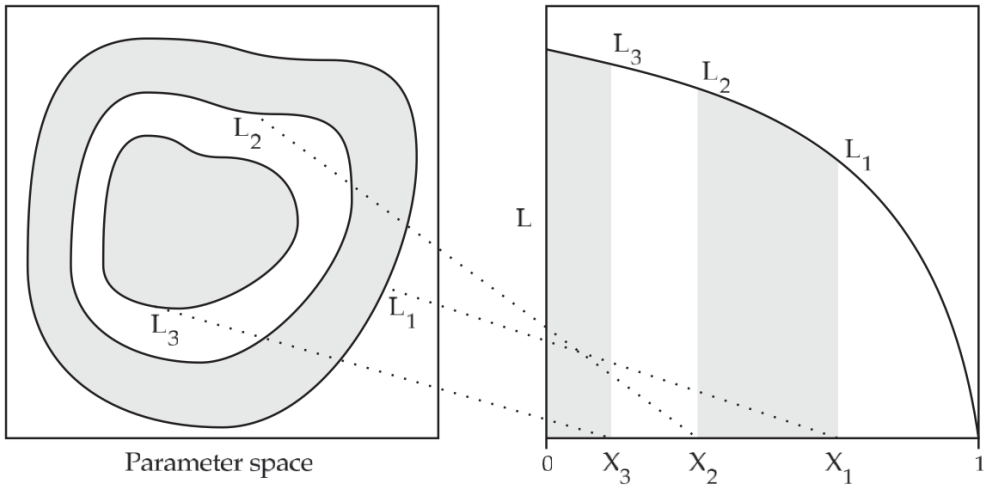

Figure 4.4. *Conversion of the multi-dimensional evidence integral to a mono-dimensional one.* The mapping between the contour lines in the physical parameter space and the prior masses allows for the change of variables. Each live point is thought to be lying on a constant likelihood contour. (Reproduced from [61].)

value of X, as shown in Fig.4.4. Consequently, we can express the evidence as the one-dimensional integral:

$$\mathcal{Z} \simeq \sum_{i=1}^{N} L(X_i)\Delta X_i \,, \tag{4.36}$$

where $\Delta X_i = X_{i+1} - X_i$. Comparing Eqs. (4.34) and (4.36), we have found that the weight we need to assign to each stochastic sample can be estimated from the variation of the prior mass between successive contours.

The crucial idea is to extract from the prior's new points so that progressively smaller contour lines can be assigned to each of them, maximizing the likelihood. To achieve this, the likelihood value for each *live point* at the i-th iteration is computed. Then, the point with the least likelihood $L_i^{\min}$ is saved and removed from the set of active points: we will call it a *dead point*. The point in substitution of it can be extracted randomly via a simple Markov chain Monte Carlo step (see [16] for a thorough introduction) according to the prior, accepting only steps that keep the likelihood above the minimum previously found. These samples are drawn from the prior distribution within the likelihood contour of the dead point (i.e., they are extracted inside a fraction X_i of the full prior). It can be shown that the volume enclosed at each iteration shrinks geometrically, ensuring the speedy convergence of the integral [64]. We can then the assign a weight $w_i = X_i - X_{i-1}$ to the i-th iteration's dead point, where the (log-)prior volume at each iteration changes by a factor:

$$\mathrm{E}[\ln X_i - \ln X_{i-1}] = -N^{-1} \,, \tag{4.37}$$

E[·] being the expected value and N the number of live points. We can use Eq. (4.34) to update the evidence at each step as:

$$Z_i = Z_{i-1} + L_i^{\min} w_i \,, \tag{4.38}$$

where an explicit computation from Eq. (4.37) gives $w_i = \exp(-i/N)$. Iterations continue until a termination condition is met, usually when the total evidence that would be left if all the remaining points lay at the maximum likelihood so far discovered $L^{\max}$ becomes less than a certain fraction of the total evidence so far accumulated, e.g., $L_{\max} w_f < Z_f e^{-5}$, where f is the number of the final iteration. The residual live points are then recycled and included in the evidence computation with equal weight w_f, giving:

$$\mathcal{Z} \simeq Z_f = Z_{f-1} + \sum_{a=1}^{N} L_a w_f \,. \tag{4.39}$$

Extracting the posterior from the evidence is a simple task, with negligible computational costs. For further details on its application to inspiral GW signals with a detector network, see [68].

Chapter 5

A Phenomenological Study

This chapter presents the results of an original and independent research that aims at assessing with software simulations the possibility of inferring the polarization content of a transient GW within a Bayesian framework, given the extended network of five ground-based interferometric detectors available in the near future. In the first section, an overview of the goals and methodology adopted for the study is given. Then, the network response to a fully-polarized transient GW is described. Finally, the polarization content for simulated signals is inferred, with particular attention to the relation between the precision/accuracy of the reconstruction and the SNR of the signal. Further, systematics relating the reconstruction of the modes and the specific polarization content of the wave is investigated at different SNRs.

A technical note on this phenomenological study is publicly available on the LIGO Document Control Center [54].

5.1 Motivation, Methods and Goals

This section introduces the research question this thesis aims to answer. We then make some considerations about the methods to best address the goals of this phenomenological study. The second subsection is devoted to a discussion of the possible gravitational waveforms we can use and some arguments are presented in favor of the simplified toy model we describe in the following.

5.1.1 Research Question and Methodology

The main goal of this study can be summarized in the following *research question*, which constitutes our starting point:

> *How well can we constrain admixtures of scalar and/or vector polarizations in a transient Gravitational-Wave signal, given the extended network of five ground-based interferometers available in the near future?*

In other words, we want to quantitatively study the accuracy at which we can recover non-GR polarization modes in a GW signal, using a network of five interferometers (three LIGO instruments, Virgo, and KAGRA).

Let's assume that GR is not our ultimate theory of gravity. As we saw in Sec. 2.3, different theories make different predictions on the possible polarization modes, and GR is the more restrictive one, admitting only two tensorial polarizations. Therefore, polarization tests are among the strongest tests on GR one may perform.

The approach we will adopt consists in simulating the network response to a transient GW signal in the most generic theory of gravity, equipped with all six polarization degrees of freedom. Once the waveform is chosen, we add noise to the signal to make it more realistic and use the techniques described earlier in Ch. 4 to recover the injected value for the wave polarization content. Since the polarization modes are encoded in some observables (variables we effectively measure), the Bayesian Inference methodology described in Sec. 4.3 is the most adequate tool to analyze their values, providing probability distribution functions (what we called *posteriors*) for each parameter of the model. The shape expected for each *posterior* is Gaussian, since we are injecting the signal in a stationary Gaussian noisy background, and the distribution we obtain from statistical inference will carry all the information we need. In particular, we focus on:

- *Accuracy* — The closeness of the mean value for each distribution to the injected value chosen for the simulation is a measurement of the precision at which we can recover the polarization content of the wave from the noisy data.
- *Precision* — The width of the distribution represents how well the polarization content is recovered. If the tail of the distribution is well detached from zero, it means that the polarization component related to that specific variable has been detected.

Further, the Bayesian approach can also be used in *model selection* to compute the odds for a non-GR description of the signal.

The outcome of our study is a Python code (fully reported in Appendix B) that generates and analyzes GW signals with generic polarization content, within a Bayesian framework. Most of the code is written from scratch by the author. Noise generation and matched filtering algorithms are both implemented using the PyCBC Python open-software package [50], while the inference code is built upon the Dynesty package [64], a free Pure Python, MIT-licensed Dynamic Nested Sampling package for estimating Bayesian posteriors and evidences.

The preliminary part of this original study was already examined in Ch. 3. In Sec. 3.2.3, we recovered the *antenna patterns* for a two-arm and a three-arm interferometer. In Sec. 3.3, we extended the study of the *overlaps factor* as defined in Eq. (3.28) from the three interferometers network (performed in [38]) to the future five-detector network of Fig. 3.7. In this chapter, we focus our attention to polarization reconstruction from simulated data, as we will see in the following.

This research is motivated by several reasons. First of all, as we showed in Ch. 3, the response in amplitude of a single interferometer (as well as the one of the entire network) to different GW polarizations is peculiar of the geometry of the source-detector and independent from the specific metric theory within the waveform is computed and generated. As already stressed before, the key idea is that, in such tests, *no polarization information is extracted from the phase evolution*, which strictly depends on the theory we choose to describe the coalescence of the binary. As in Sec. 3.4, this allows for model-independent strategies to reconstruct the polarization content of the wave, e.g. the *null stream approach* described in [19]. However, it is crucial to quantify in advance (even before the construction of the detectors) the sensitivity of the network because it does depend on the position and orientation of the detectors. Our code is very flexible and new ground-based interferometers with two or three arms can be easily added to (or removed from) the network. Such studies can provide strong evidence in support of some particular configurations for future detectors.

Furthermore, testing a methodology to extract polarization content is crucial for implementing these techniques in *data analysis pipelines*. Since the two scalar polarizations are completely degenerate for ground interferometers, we have a total of five (distinguishable) modes. If the direction on the sky is known, for example via the observation of ah electromagnetic counterpart, we have a total of five degrees of freedom (up to an overall amplitude) for the polarization content of the wave. To completely disentangle the polarizations, at least five interferometers are needed. This is the reason why the future five-detector network was chosen for our study. Some initial tests within a Bayesian framework on polarizations has already been made in [8] (the first GW with a strong electromagnetic counterpart that allowed for a precise determination of the position), where an overwhelming evidence in favor of pure tensor polarization modes in comparison to pure vector and pure scalar modes was found. However, no constraints can yet be placed on small admixtures of non-GR modes with tensorial ones, due to the limited number of available detectors

and to Virgo's low SNR for this specific event. This will be possible in the range of 5-10 years, when the five detectors network will be operating at full sensitivity. In conclusion, our phenomenological study can provide a foretaste of near future fundamental tests of gravity.

5.1.2 Preliminary Considerations on the Waveform

During the first observing run (O1), from September 12, 2015 to January 19, 2016, and the second observing run (O2), which ran from November 30, 2016 to August 25, 2017, the LIGO-Virgo Collaboration achieved several GW detections (for the most recent catalog, see [4]). They were all *transient* (limited in time) GWs coming from Compact Binaries Coalescence events. Such waves are emitted when two compact bodies (neutron stars or black holes) orbit one around the other faster and faster, bound by their reciprocal gravitational attraction, until they collapse into each other. The remnant static body has often a mass lower then the sum of the progenitor ones. Part of the total mass of the two original bodies is indeed converted into energy and released as gravitational radiation. The GWs emitted by inspiralling binaries systems can be accurately modelled using a high-order PN GW generation formalism, as we saw in Ch. 2. The gravitational waveform and energy flux are then obtained to high PN order and the binary orbital phase evolution is determined from an energy balance argument (see [14] for a thorough review).

Within GR, from Eq. (2.26), we can compute the inspiral gravitational waveform for a binary system of two bodies of mass m_1 and m_2 in quasi-circular orbit at leading PN order, expressing the quadrupole moment as a function of $(\hat{x}^j, \hat{v}^j)$, the orbital trajectory and orbital velocity unit vectors. The calculation leads to the following equation for the potentials (in geometrized units):

$$h^{jk} = \frac{4\mu M}{Dr}(\hat{v}^j\hat{v}^k - \hat{x}^j\hat{x}^k)\,, \tag{5.1}$$

where $M \coloneqq m_1 + m_2$ is the total mass, $\mu \coloneqq m_1 m_2/M$ the reduced mass, r the orbital separation, and D the (luminosity) distance of the source. Let $\Phi(t)$ be the orbital phase and ι the inclination angle of the system, from Eq. (3.25) we may write the response function of an interferometer $h(t)$ in time domain as:

$$h(t) = A_{\rm GR}\frac{\mathcal{M}^{5/3}}{D}\dot{\Phi}^{2/3}e^{-i2\Phi} + \text{c.c.}\,, \tag{5.2}$$

where

$$A_{\rm GR} \equiv -F_+(1+\cos^2\iota) - 2iF_\times\cos\iota\,, \tag{5.3}$$

$\mathcal{M} = \mu^{3/5}M^{2/5}$ is the *chirp mass* and we have used Kepler's third law to simplify the result. The response function is composed by a slowly varying amplitude and a rapidly varying phase Φ. The phase evolution in time is usually computed from the balance law that relates the rate of change in binding energy to the GW luminosity. From Eq. (5.2), the Fourier transform $\tilde{h}(f)$ of the waveform is then computed (often in a Stationary Phase Approximation (SPA), see e.g. [19], Sec. IIB) and it is used to filter experimental data.

As discussed in Sec. 4.2.2, data analysis techniques generically use the template of the waveform to detect the wave, introducing what Yunes and Pretorius in [80] called a *fundamental bias* in GW astrophysics: the assumption that GR is the correct theory of gravity during the entire wave-generation and propagation regime. So far, only GR templates have been used to detect GWs. Although the experimental data seems to fit well with GR templates, systematic errors in the detection and parameter estimation of signals can arise, leading to a mischaracterization of the Universe through incorrect inferences about source event rates and populations. The key point is that the GR limit (or better, the GR limit within the ppN framework) is valid in the *weak field* regime, as verified by precision experiments and observations, but it need not to hold in the dynamical strong-field regime where tests are lacking (and where GWs are generated). In the aforementioned work, Yunes and Pretorius proposed a remedy through the introduction of the *parameterized post-Einsteinian* (ppE) framework, which consists of the enhancement of waveform templates via the inclusion of extra-parameters, called *ppE parameters*. These modified templates are *deformations* of the GR waveform achieved by introducing extra phases and amplitudes terms which depend on ppE parameters. In the standard ppE framework, only deformations of the two GR polarizations are considered. These are induced by corrections to the frequency evolution equation only, and can arise from modifications of the binding energy or energy flux carried by the wave. The simplest ppE template for the inspiral stage may be written as:

$$\tilde{h}(f) = \tilde{h}^{(\mathrm{GR})}(f) \cdot (1 + \alpha u_2^a) e^{i\beta u_2^b}\,, \tag{5.4}$$

where

$$u_\ell = \left(\frac{2\pi \mathcal{M} f}{\ell}\right)^{1/3} \tag{5.5}$$

is the reduced ℓ-harmonic frequency, $\tilde{h}^{(\mathrm{GR})}(f)$ the Fourier-domain GR template, and (α, a, β, b) the four ppE parameters. This modified template takes into account possible variations from GR. Furthermore, Sampson *et. al.* have shown in [58] that ppE parameters can be put in relation to ppN parameters (see Ch. 1), making it possible to specify the model for (almost) every metric theory. Chatziioannou *et. al.* in [19] have extended the ppE framework to include all harmonics (since the previous template is adequate to describe the $\ell = 2$ harmonic only) and all polarizations. The templates obtained are essentially modifications of the GR template with additive amplitudes and phase factors for each polarization degree.

Motivated by this analytic results, we tried to build a similar waveform for our study: a superposition of different amplitudes, one per polarization mode. However, as we already stressed previously, all the information regarding GW polarizations does not depend on the phase evolution of the wave. This is a crucial property of GW detection that allows for a further simplification. Since we aim to perform a phenomenological test on the possibility of inferring GW polarization content for a generic wave, we do not need the full description provided by the ppE scheme. This will be useful in a future GR test on real experimental data, providing a model-independent template to filter the signal, at the price of expanding the parameter space. Additionally, the ability to reconstruct polarization content is a property

of the detector network itself and it is almost independent from the metric theory we used to compute the waveform. Our final goal is indeed to show that, if *any* extra-polarization signal other than tensorial is present in the wave (as allowed by other metric theories of gravity, as we showed in Sec. 2.3.2), the five-interferometer network is able to detect it and disentangle it from the tensorial ones. Inspired by the approach illustrated in Sec. 3.4.2, which constitutes a model-independent way of reconstructing the GW signal and its polarization content, we decided to use monochromatic sine-Gaussians as our candidate transient waveform. A full description of the waveform and its network response in simulations is provided in the following section.

5.2 Fully Polarized Gravitational Wave: the Network's Response

In this section, we describe in detail the waveform used in this phenomenological study and the five-detector network response to it.

5.2.1 The Waveform

A specific source of gravitational waves is generically identified by the following astrophysical parameters:

- Sky coordinate location: (δ,α);
- Polarization angle: ψ;
- Geocentric sidereal time of arrival: t_0;
- Luminosity distance of the source: d_L.

For what we said in Sec. 5.1.2, it is reasonable to build a simplified toy model of the response at each two-arm detector I using a single sine-Gaussian wavepacket with given frequency Ω and relaxation time τ:

$$h_I(t) = A_I \cos(\Omega t + \phi_I) \exp\left[- \frac{(t - t_0 - \delta t_I)^2}{2\tau^2} \right], \tag{5.6}$$

where

$$A_I = \frac{|A|}{d_L} |\tilde{A}_I| \,, \tag{5.7}$$

$$\tilde{A}_I = \sum_{p \in \{+,\times,x,y,s\}} \epsilon_p F_p^I \,. \tag{5.8}$$

We implicitly defined the following quantities:

- the complex coefficients
$$\epsilon_p = \frac{a_p}{|A|} e^{i\phi_p} \tag{5.9}$$
which depend exclusively on the unknown underlying properties of the GW generation mechanism (e.g., the tensor ones, within a tri-axial emission model, are functions of the inclination angle ι) and are also coordinate frame dependent quantities. Since we pick $|A|$ to be the total amplitude, we expect $|\epsilon_p| \in [0, 1]$;
- $|A| = \sqrt{\sum_p a_p^2}$ is the overall amplitude of the wave;
- $F_p^I = F_p^I(\alpha, \delta, \psi = 0, t_0)$ are the antenna patterns for the detector I. By setting $\psi = 0$, we are choosing a specific polarization frame: we can arbitrarily fix the polarization angle thanks to the degeneracy between ψ and the two pairs of parameters $(\epsilon_+, \epsilon_\times)$ and (ϵ_x, ϵ_y), consequence of the rotational property of antenna patterns (see Appendix A in [37]);
- the measured phase at the detector I is:
$$\phi_I = \arctan \frac{\mathrm{Im}[\tilde{A}_I]}{\mathrm{Re}[\tilde{A}_I]} - \Omega(t_0 + \delta t_I) \tag{5.10}$$

Following [37], we can also define the *normalized effective strain amplitudes* as:

$$h_t = \sqrt{|\epsilon_+|^2 + |\epsilon_\times|^2}\,, \tag{5.11a}$$

$$h_v = \sqrt{|\epsilon_x|^2 + |\epsilon_y|^2}\,, \tag{5.11b}$$

$$h_s = |\epsilon_s|\,. \tag{5.11c}$$

We can introduce two (coordinate independent) hyper-parameters λ_v and λ_s to quantify how much of the wave is tensor, vector or scalar polarized, so that:

$$h_t^2 = 1 - \lambda_v - \lambda_s\,, \tag{5.12a}$$

$$h_v^2 = \lambda_v\,, \tag{5.12b}$$

$$h_s^2 = \lambda_s\,. \tag{5.12c}$$

The main goal of this research is to establish how well we can infer the two hyper-parameters λ_v and λ_s from signals with different SNR.

5.2.2 Simulated Network Response

An example of the pure signal as seen in each detector of the network can be found in Fig. 5.1. The effective time of arrival of the signal (i.e., the time at which the perturbation reaches its peak in each detector) is shifted with respect to t_0, the sidereal time of arrival at the center of the Earth, due to signal propagation through the Earth. In this study, the propagation speed is assumed to be equal to c, the speed of light, for every polarization mode. Although this property does not hold true for some theories, as we showed in Sec. 2.2.2, this simplification does not have any consequence on polarization reconstruction, apart for some extra degrees of freedom (the speed of each wave mode) that should be taken into account in parameter estimation. The overall amplitude and the luminosity distance are two degenerate parameters that cannot be distinguished in principle, since at farther distance equal sources will result in weaker waves due to the d_L^{-1} dependence of the metric in the *far wave zone* [see Sec. 2.1.3, Eq. (2.16) in which we neglected $R^{-2} \equiv d_L^{-2}$ terms].

To provide a realistic simulation of the network response, Gaussian colored noise (weighted in frequency space) was added to the signal timeseries. To generate the noise, we used the designed analytical PSD $S_n(f)$ for each detector, in the most optimistic prevision, called *designed sensitivity*. As seen in Sec. 4.1.2, the PSD can be interpreted as the variance of the Gaussian instrument noise (with zero mean) in each frequency bin. Noise generation was implemented using PyCBC [50]. The noise is then added to the pure signal, yielding the response as shown in Fig. 5.2. The signal is completely buried into noise.

If, however, we apply the matched filter we described in Sec. 4.2.2, we find that the mean SNR around the peak of the signal is about 8, just enough to make it a candidate. The response strain in frequency space as well as the SNR of the signal for the detector LHO, obtained using the matched filtering technique, are reported in Fig. 5.3. We recall that in this study we want to relate the ability of reconstructing polarization modes of the wave to the SNR of the signal, trying to determine whether any systematics are present. We do not aim to put any lower bound limit on the overall amplitude of the wave that can be detected and disentangled. This is the reason why we used the most optimistic PSD available for each detector, instead of realistic ones. The disentanglement power of the network in separating polarization modes depends on the overall amplitude of the wave only via the SNR of the signal, as we will see in the following.

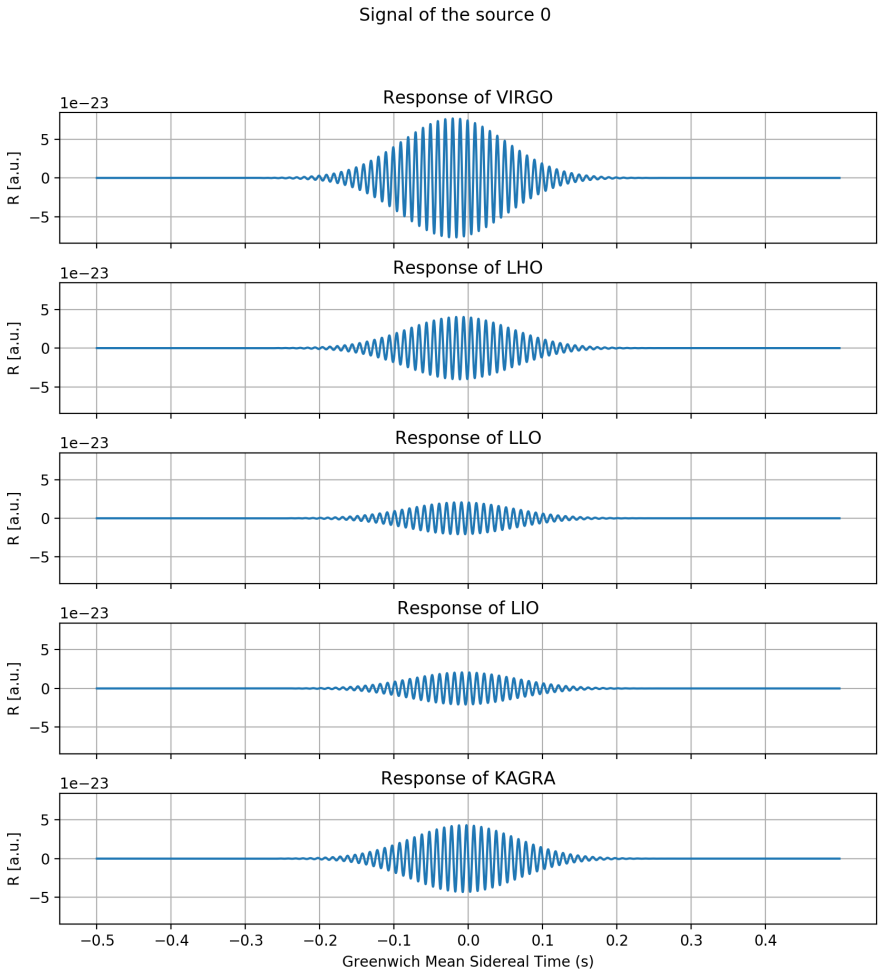

Figure 5.1. *Example of a simulated GW signal as seen by the network.* The signal shown was generated with random sky location (α,δ), random polarization angle ψ, sidereal time of arrival at the center of the earth $t_0 = 0\,\mathrm{s}$, unitary luminosity distance $d_L = 1$. Both λ_v and λ_s were set to 0.1 with fixed overall amplitude $|A| = 10^{-22}$, randomly choosing the remaining amplitude parameters (the two ϵ's and the five phases ϕ_p). The total duration of the segment is 1 s and the sine-Gaussian was chosen with frequency $\Omega = (2\pi)100\,\mathrm{Hz}$ and damping time $\tau = 0.1\,\mathrm{s}$. Time shifts between signals of several tens of ms are due to the signal propagation (assumed to happen at the speed of light) through the Earth, while amplitude changes are a direct consequence of the various detector antenna response functions (see Sec. 3.2.3). The polarization analysis is based on these last amplitude (and phase) differences.

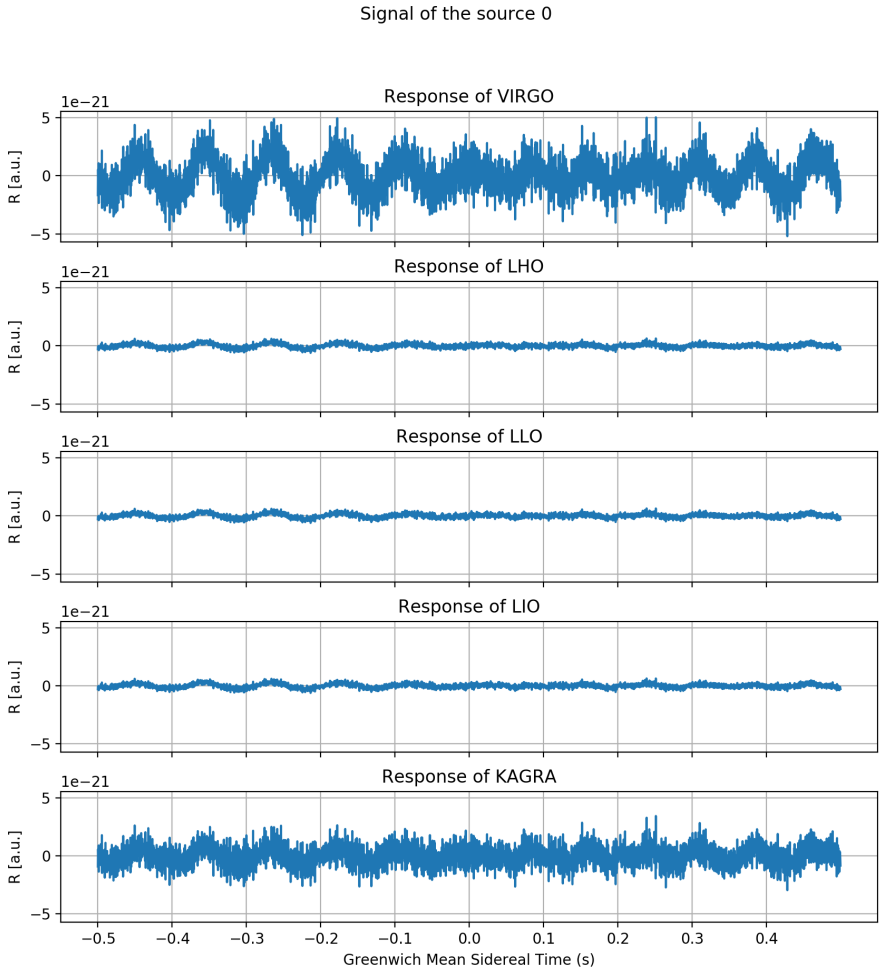

Figure 5.2. *Example of a simulated noisy GW signal as seen by the network.* The noisy response of the network is shown for the pure signal of Fig. 5.1. The GW signal is buried into Gaussian colored noise, that is more than one order of magnitude greater than the signal amplitude itself. Low frequency noise content is seen to dominate. In this figure, we can appreciate differences in the *design sensitivity* of the five detectors: the PSD used for the LIGO detectors is indeed the most optimistic version for the aLIGO+ update [13], which is almost half an order of magnitude lower (in its most sensitive part) than Virgo and KAGRA ones.

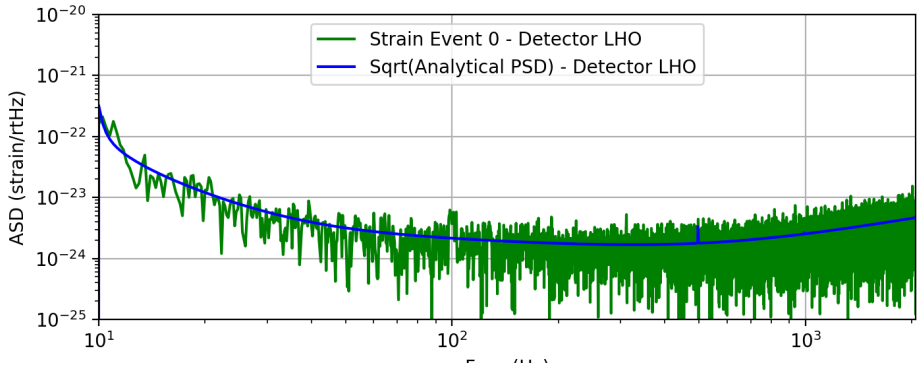

(a)

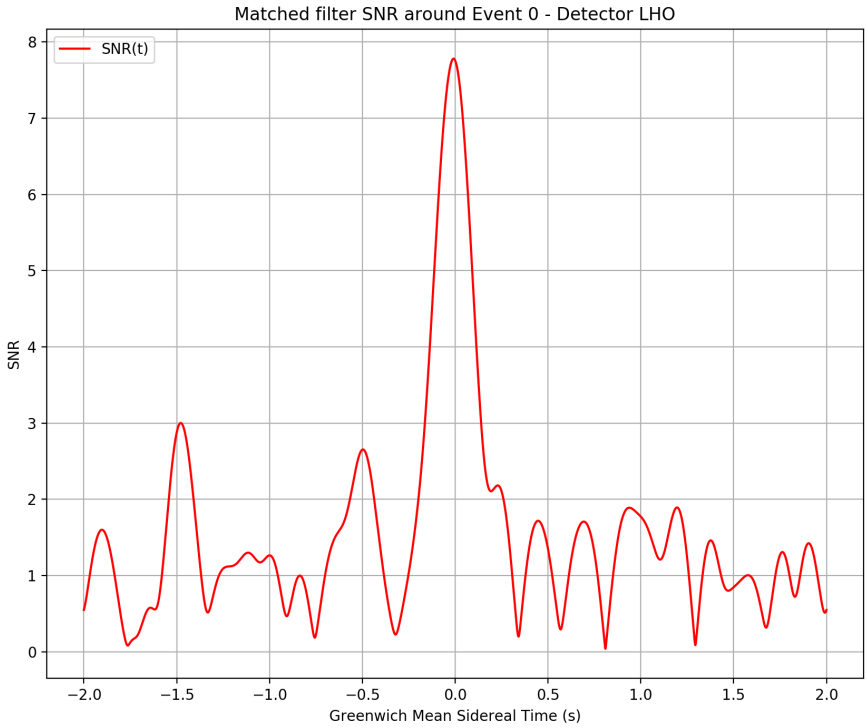

(b)

Figure 5.3. *Matched filtered LHO detector response for the noisy signal in Fig. 5.2.* Both the response strain in the frequency domain, with the analytical PSD superimposed (a) and the time evolution of the SNR of the response (b) are reported. As expected, the SNR shows a peak for the time of arrival of the wave.

5.3 Bayesian Inference of the Gravitational-Wave Polarization Content

In this section, we present the results of our phenomenological study. We limited our analysis to Bayesian parameter estimation. Indeed, the *posterior distributions* found for the polarization (normalized) amplitudes ϵ's or the hyper-parameters λ's encode all the information we need to study both the *accuracy* and *precision* of polarization reconstruction.

5.3.1 Tools

For the sake of completeness, we recall in the following the main ingredients to perform Bayesian parameter estimation given some experimental data $\mathbf{D}$ and a model $\mathcal{H}$ that depends on a set of parameters $\boldsymbol{\theta}$. In Sec. 4.3.2, we have found that we can use Bayes' theorem to recover the joint *posterior* probability distribution function on the multidimensional space of parameters

$$P(\boldsymbol{\theta}|\mathcal{H},\mathbf{D}) = \frac{P(\mathbf{D}|\mathcal{H},\boldsymbol{\theta})P(\boldsymbol{\theta}|\mathcal{H})}{P(\mathbf{D}|\mathcal{H})}\,, \tag{5.13}$$

where:

- $P(\mathbf{D}|\mathcal{H},\boldsymbol{\theta})$ is the *likelihood*.
- $P(\boldsymbol{\theta}|\mathcal{H})$ is the (multidimensional) *prior* of our model. We can choose a single parameter and find the (one-dimensional) probability distribution function for it by integrating over the other parameters: this procedure is called *marginalization*.
- $P(\mathbf{D}|\mathcal{H}) = \int_{\boldsymbol{\Theta}} P(\mathbf{D}|\mathcal{H},\boldsymbol{\theta})P(\boldsymbol{\theta}|\mathcal{H})d\boldsymbol{\theta}$, often indicated by $\mathcal{Z}$, is the *evidence*, the core target of computations performed with the Nested-sampling algorithm (Sec. 4.3.5).

In the following, we define each object that appears in Eq. (5.13) for the case in point.

Parameters space — Assuming the toy model described in Sec. 5.2.1, fixing the sine-Gaussian frequency Ω and damping time τ, we are left with a total of 12 independent parameters $\{\alpha, \delta, |A|, \phi_+, \phi_\times, \phi_x, \phi_y, \phi_s, \epsilon_\times, \epsilon_y, \lambda_v, \lambda_s\}$. Notice that d_L is degenerate with $|A|$, ψ is degenerate with some of the amplitudes (as shown in appendix A in [37]) and the time of arrival t_0 cannot be inferred since we simulate the response of the network for a symmetric interval in time with respect to t_0 itself (2 s before and 2 s after). Due to the heavy computational cost of each simulation, for practical purposes we chose to reduce the dimensions of the parameters space to 6, assuming the overall amplitude and the five amplitude phases to be known.

Priors — Priors in the sky locations are set to be uniform over the celestial sphere: the right ascension (α) prior is flat in the interval $[0, 2\pi)$ while the cosine of declination ($\cos\delta$) prior is flat in the interval $[-1, 1)$. Priors on the amplitude parameters (the two λ's and the two ϵ's) are taken to be flat in the interval $[0, 1)$, provided we get the normalization to one of the five ϵ's square sum. Indeed, it can happen that these four amplitude parameters are not compatible with each other: in this case, we reject the point in the parameter space, weighting it by a negative infinite likelihood, which is well handled by the Python code as it can be implemented as a NumPy constant.

Likelihood — As seen in Sec. 4.3.4, the likelihood for a network of GW detectors with uncorrelated noise can be written in the general form:

$$\begin{aligned} P(\mathbf{d}|\mathcal{H}, \boldsymbol{\theta}) &= \prod_I P(d_I|\mathcal{H}, \boldsymbol{\theta}; S_n^I(f)) \\ &= \exp \sum_I \sum_j \left[- \frac{2\left|\tilde{h}_j^I(\boldsymbol{\theta}) - \tilde{d}_j^I\right|^2}{TS_n^I(f_j)} - \frac{1}{2}\log\frac{\pi T S_n^I(f_j)}{2}\right], \end{aligned} \tag{5.14}$$

where $\tilde{d}_j^I$ is the content of the j-th bin of the Discrete Fourier Transform [defined in Eq. (4.31)] of the noisy signal as seen by the I-th detector, $\tilde{h}_j^I(\boldsymbol{\theta})$ is the pure signal prediction for it at fixed value of the parameters $\boldsymbol{\theta}$, $S_n^I(f_j)$ is the PSD of the noise for the I-th detector in the j-th frequency bin, and the sum runs over all frequency bin and detector index values j and I. A visual study on the mono-dimensional and bi-dimensional behaviour of this likelihood in parameter space is reported in Appendix A for a random high-SNR signal.

Bayesian sampler and Output — The likelihood and the priors were plugged into the Bayesian Nested-sampler. The sampler outputs the posterior distributions for the parameters we choose to infer. These can be visualized using the built-in Dynesty plotting utility. The two used in the following are *trace plot*, showing the evolution of the values sorted for the parameters (and their marginal posterior distributions) in one-dimensional projections, and the *corner plot*, which shows a combination of one-dimensional and two-dimensional marginalized posteriors.

Posteriors Analysis — The marginalized one-dimensional posteriors for each simulation are then saved and stored in Python dictionaries. The grafic utility Seaborn [71] is then used to compute Kernel Density Estimations (KDEs) and to produce *violin plots*: this kind of plot shows the distribution of quantitative data across several levels of one (or more) categorical variables so that those distributions can be compared. Unlike a box plot, in which all of the plot components correspond to actual datapoints, the violin plot features a KDE of the underlying distribution. This is indeed the most effective and appealing way of showing multiple distributions of data at once.

5.3.2 Results

In this section, we present the results of our research. As a first example to validate our methodology, we tested our inference code on two signals with different SNRs, to recover six parameters of the wave (sky location and four amplitude parameters), as discussed in the previous section. These cases represent a low (about 10 in each detector) and a high SNR scenario (about 100 or more). *Trace plots* and *corner plots* of the two examples are reported in Fig. 5.4 and in Fig. 5.5. The trace plots show the evolution of the sampled parameter space points as a function of the variable X, which corresponds to the one-dimensional variable used to compute the evidence integral (the *prior mass* defined in Sec. 4.3.5). This variable (or more appropriately, $-\ln(X)$) can be seen as a proxy for the number of iterations the algorithm needs to converge to the global maximum of the likelihood. The corner plots show the two-dimensional posteriors for each parameter pair (marginalized over all other parameters), and, on the diagonal, the mono-dimensional posterior distribution of each single parameter (marginalized over all other parameters), as recovered by the algorithm. In all plots, red lines identify the injected value.

In both cases, the injected value is recovered correctly with a high accuracy (generally within one sigma), but the precision of the result crucially, and not surprisingly, depends on the SNR. In the second simulation, in which the SNR is much lower, the posterior distributions are wider and less peaked around the true value. This is the first important result of our study: the network (within this model) is able to disentangle all the polarization degrees of the wave, but the precision (i.e., the sensitivity of the network to each specific polarization) strictly depends on the strength of the signal and its SNR in each detector.

To further analyze the systematics of this behaviour, we simulated several different signals from sources with increasing value of the hyper-parameters λ's, randomly setting the other ten parameters to have three different SNRs (in each detector) for each λ: greater than 100, between 25 and 100, lower than 30. We repeated this study for a mixture of two polarizations (taking one of the two λ's to be vanishing) and three polarizations (allowing both λ's to be non-zero and set to the same value). The marginalized posterior distributions for the λ's are reported in Fig. 5.6 for the two-polarization admixture and Fig. 5.7 for the three-polarization one. As expected, the higher the SNR is, narrower and better peaked around the injected value the posterior distribution is. Qualitatively — for low SNR sources — the more the wave is a mixture of different polarizations, the worse it is generally recovered by the network. This can be explained thinking that for highly mixed waves we are adding possible degeneracies to the network responses: for a complex wave (superposition of many different polarizations), it is more difficult to disentangle the single contributions. Besides this qualitative behaviour, there is no particular systematic on the value at which the distribution is peaked at: they are — at least for the low SNR scenario, in which they can significantly differ from the true value — randomly distributed around the true injected value.

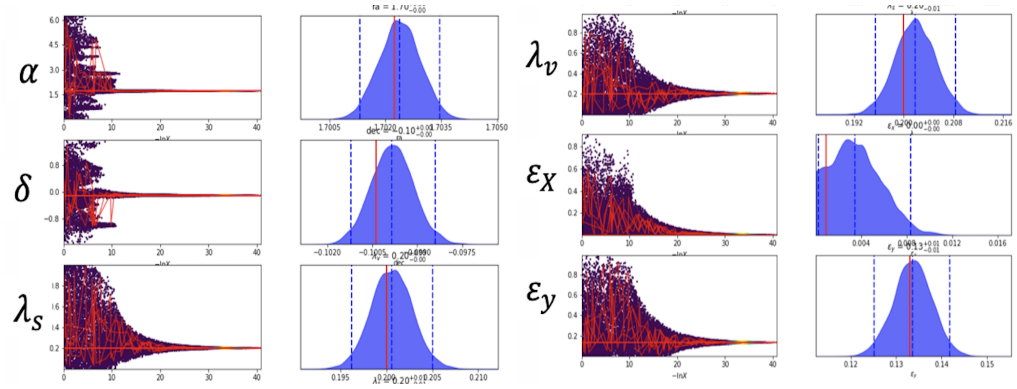

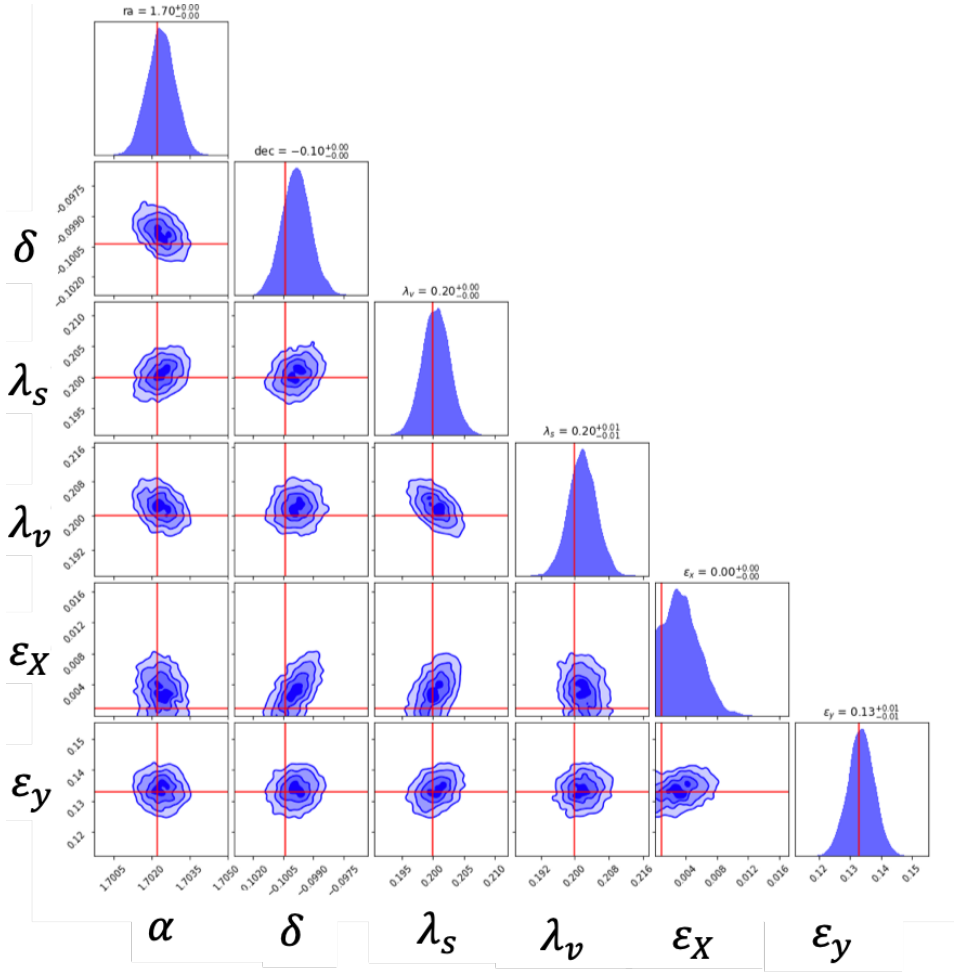

Figure 5.4. *Trace plots and corner plots of a high SNR source.* The injected true value (red lines in both plots) is well recovered after some iterations of the sampling algorithm, with high accuracy and high precision. This specific source was randomly chosen with an $\epsilon_\times$ close to zero: the algorithm correctly provides upper limits for its value. Dashed lines in the trace plots enclose the 95% (2-sigma) credible intervals.

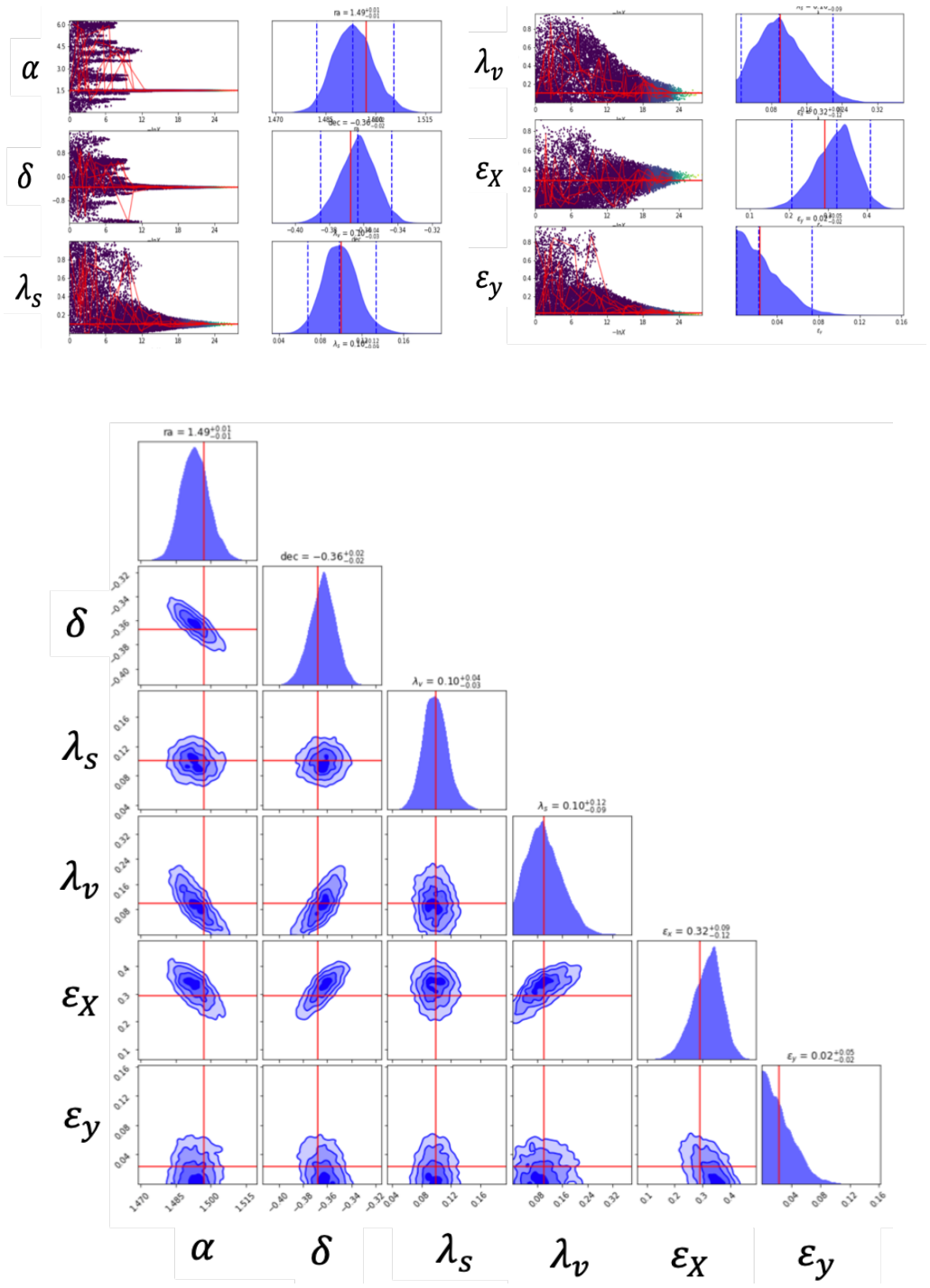

Figure 5.5. *Trace plots and corner plots of a low SNR source.* Same as Fig. 5.4, but for the low SNR scenario. The injected values are still well recovered, but with a lower precision with respect to the previous case. This specific source was randomly chosen with an ϵ_y close to zero: the algorithm correctly provides upper limits for its value.

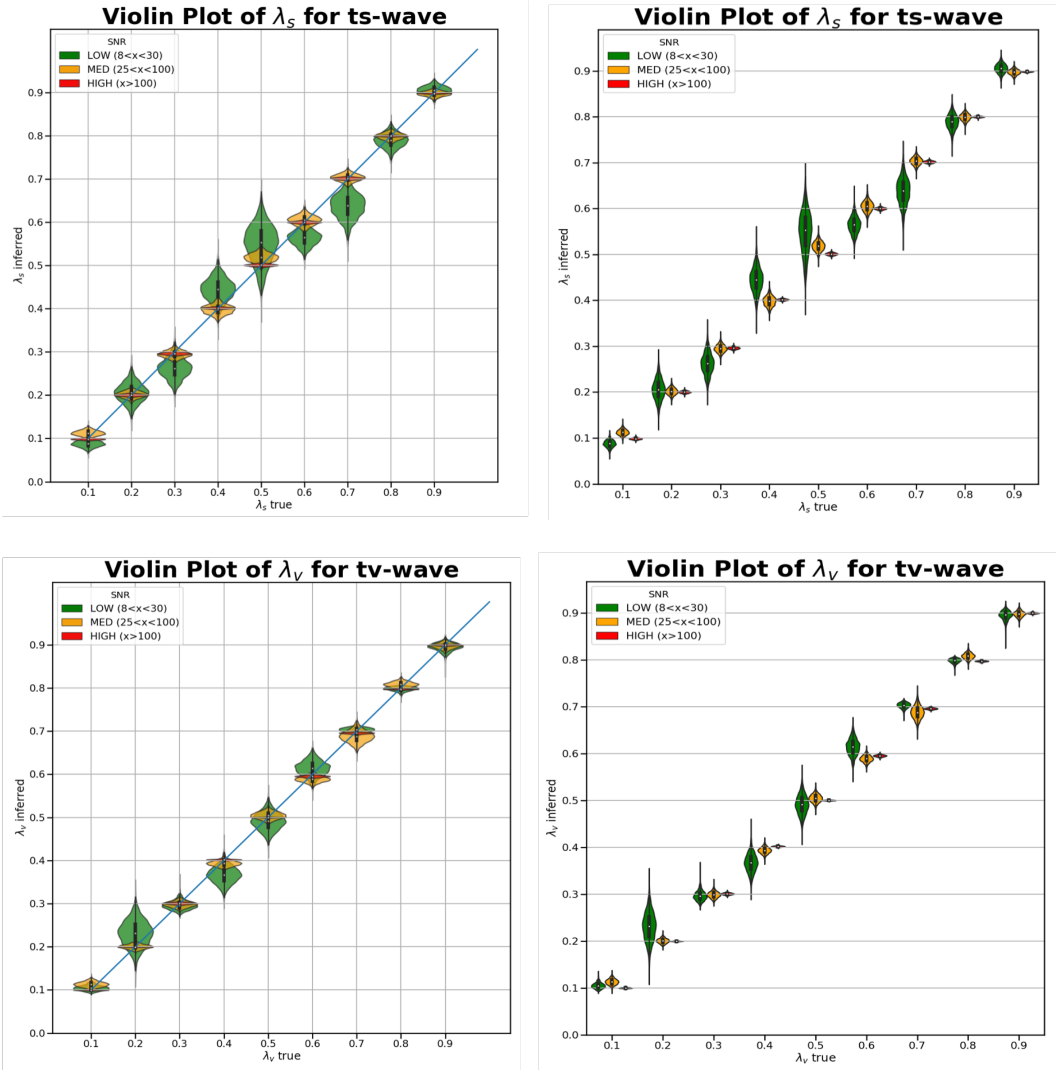

Figure 5.6. *KDE of the marginalized posterior distribution for λ_s in the case of tensor-scalar polarized waves (top) and for λ_v in the case of tensor-vector polarized waves (bottom), with different SNR and increasing non-GR content.* Both plots for each kind of two-polarization wave represent the same data: the horizontal axis shows the true injected value, while on the vertical axis reports the posterior distribution as recovered by our Bayesian analysis. The difference between the two panels on each is only in the way results are plotted: on the left, violin plots for the three SNR sources are superimposed to show if there are systematic deviations from the diagonal line, which represents the true injected value. On the right, the three violin plots are plotted next to each other, so the horizontal grid line is the only meaningful reference for the true value. The white dot inside the distribution corresponds to the mean value, while the black band represents the first quartile interval.

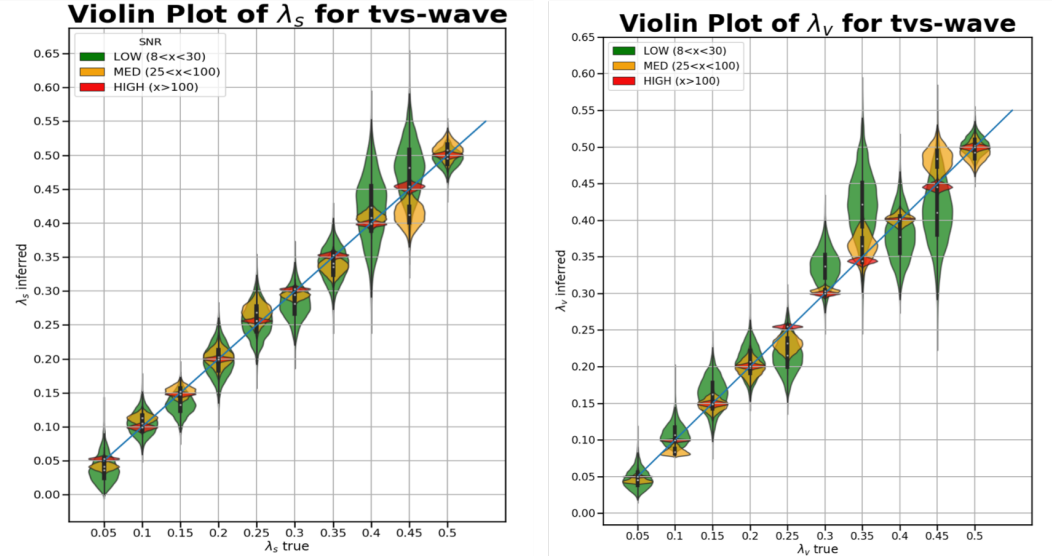

Figure 5.7. *KDEs of marginalized posterior distributions for λ_s (left) and λ_v (right) for tensor-vector-scalar polarized waves, with different SNR and increasing non-GR content.* The plotting convention is the same as the one adopted in the left panels of Fig. 5.6. Qualitatively, the true value for low SNR scenarios is recovered generally worse in this case than the previous ones, due to the fact that a highly mixed wave generally increases the complexity and the possible degeneracies in the parameter space.

Finally, we simulated many other sources, fixing the mean SNR (within a range of two units) for the network, in the case of a tensor-vector-scalar polarized wave with increasing non-GR content. Posterior distributions for λ_s are reported in Fig. 5.8. As expected, the disentangling power of the network and approach generally increases with the mean SNR with some exceptions, due either to SNRs being distributed very unevenly (with a high standard deviation) among the detectors, or to statistical fluctuations in the nested sampling algorithm. The latter explanation is confirmed by repeating the analysis for the same data-sets multiple times, obtaining slightly different posterior distributions, compatible with the observed inversions.

In conclusion, it was found that through Bayesian inference it is indeed possible to accurately extract the polarization content of transient GW signals, and with precision limited by the SNR in the response. As expected, the precision mostly improves with the total network SNR, with some exceptions, due either to an SNR distributed very unevenly among the five detectors or to statistical fluctuations in the Bayesian sampler.

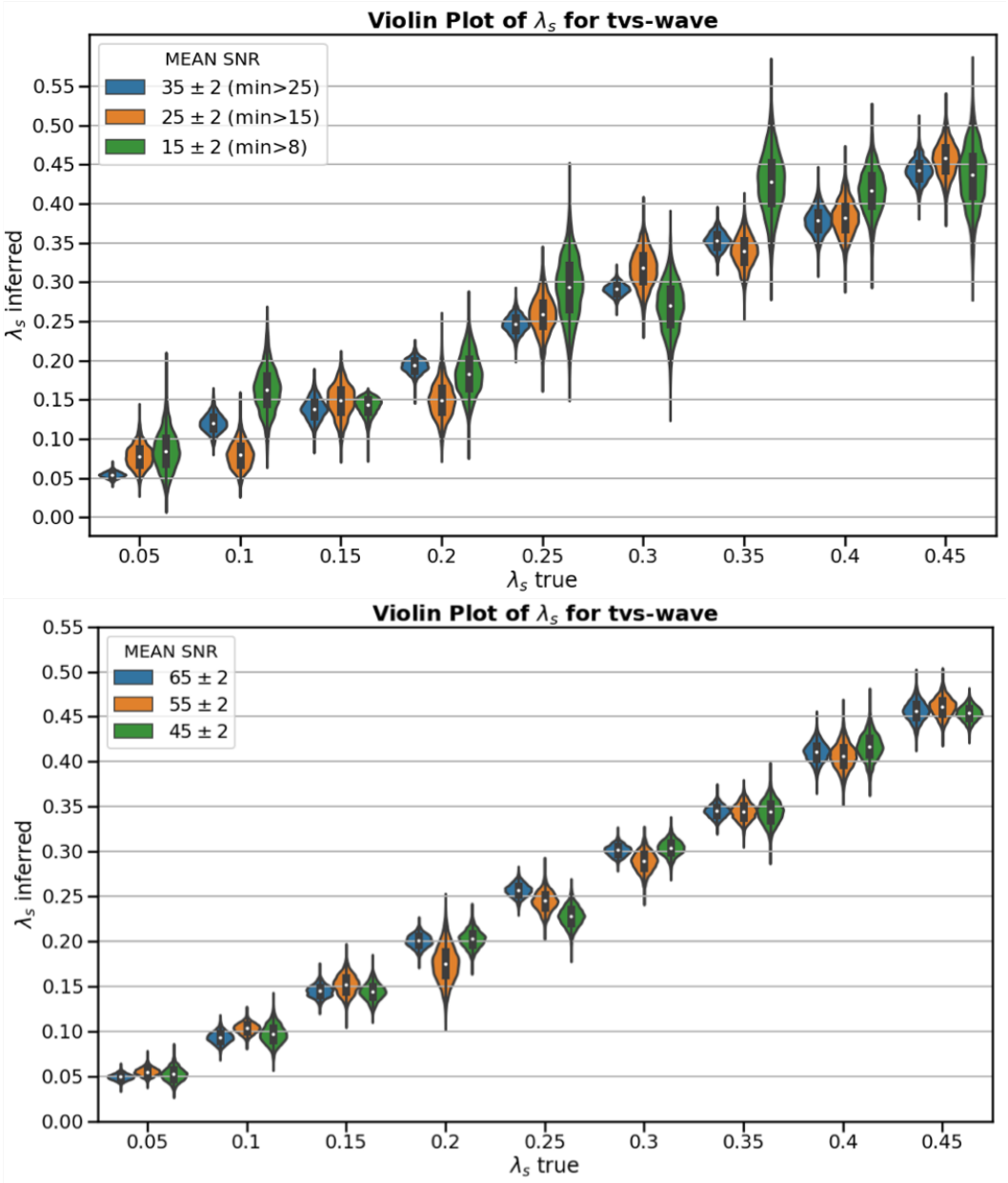

Figure 5.8. *KDEs of the marginalized posterior distributions of λ_s for tensor-vector-scalar polarized waves, with increasing SNR mean and non-GR content.* The plotting convention is the same as the one adopted in the right panels of Fig. 5.6. Inversions in the behaviour of the recovered distribution for increasing SNR mean are due both to statistical fluctuations in the sampling algorithm and to a very uneven distribution of the SNR among the five detectors.

Conclusions

«Apri la mente a quel ch'io ti paleso
e fermalvi entro; ché non fa scienza,
sanza lo ritenere, avere inteso»

Dante, *Paradiso* V

In this thesis, we have first shown that generic metric theories of gravity allow for six independent polarization modes for their waves. Depending on the field content of the theory, only some of these may be allowed. GR is undoubtedly the most restrictive theory, predicting only the two transverse tensor polarization. We have seen that the response in amplitude of a network of GW detectors is strictly correlated to the polarization of the wave through the *antenna patterns* of each interferometer, which depend only on the relative geometry between the source and the detector. After reviewing the most updated data analysis techniques to handle GW data, we proposed and realized an extensive and original phenomenological study of the performance of the five-detector network configuration [LIGO Hanford (USA), LIGO Livingston (USA), Virgo (Italy), KAGRA (Japan) and LIGO-India] in disentangling polarization modes within a Bayesian approach.

We found that, even using a monochromatic sine-Gaussian as toy model for the waveform, the network of five L-shaped interferometers at design sensitivity available in the near future is able to efficiently disentangle the five polarization components for a generic transient signal: the precision strictly depends on the SNR of the signal and how it is distributed between the five detectors. The results were obtained within a Bayesian framework, using parameter estimation techniques. Most of the code was written from scratch by the author and it flexibly allows to add (or removal) ground-based interferometers with two or three arms to the network. Such studies are of crucial importance since they can provide strong evidence in support of specific configurations for future detectors. A technical note on this phenomenological study is publicly available on the LIGO Document Control Center [54].

As a first suggested future work, model selection can be used to discriminate between different models, measuring the odds of a generic theory of gravity, given the simulated data. Since the GW polarization is mainly a geometric factor, the results found are essentially independent of any theory model. On the theoretical side, it would be interesting to numerically develop some waveforms for alternative

theories of gravity to be used in similar phenomenological studies. Some classes of extended templates that can take into account possible deviations from GR have already been studied in the literature (see [80, 19]) and it would be interesting to repeat the study using more plausible waveforms.

So far, we dealt exclusively with transient signals. However, it should be mentioned that if we have a longer lasting signal (a persistent signal detected with current detectors, 3G detectors or LISA), the motion of the interferometer relative to the source would allow us to study the evolution in time of antenna patterns, extracting more information from the single detector. For continuous GW signals, a complete study with three ground interferometers was reported in [37]. An extension of this methodology can be applied also to a larger network.

We recall that, the detection of GW non-tensor polarizations would be the first, direct evidence of new physics; at the same time, repeated non-detections would allow us to place more and more stringent tests on GR.

Appendix A

Visual Study of the Likelihood

To better understand the complexity of the likelihood, a visual study of the function in Eq. 4.32 is reported in this Appendix for a high SNR source and the toy model described in Ch. 5 with random parameters.

In Fig. A.1, we see the behaviour of the likelihood as a function of one of the phases: we uniformly sampled a one-dimensional slice of the parameter space, allowing only one of the amplitude phases to vary (ϕ_+), starting from the injected true value. On the vertical axis the difference between the value of the likelihood at the x-value minus the value of the likelihood at the injected value is plotted. If the true injected value is a global maximum for the likelihood, this difference should be always non positive and equal to zero only for the true value. The plot shows the expected behaviour.

In Fig. A.2, the likelihood as a function of the overall amplitude is studied. On the vertical axis, the absolute value of the difference between the value of the likelihood at the x-value and the value of the likelihood at the injected value is plotted. If the true injected value is a global maximum for the likelihood, the plot should drop down to $-\infty$ for A_0 equal to the true value. Also in this case, the plot shows the expected behaviour.

In Fig. A.3, two bi-dimensional studies of the likelihood are shown. In the first case, the right ascension α and declination δ are varied, while in the second case the dependence on two λ hyper-parameters of Eqs. 5.12 is shown. In the former case, the likelihood is highly non-regular, with several local maxima. This is due to the *fringe effect*, relevant for the waveform used: changing the sky location shifts the sine-Gaussians in the N detectors with respect to one another. For high frequency (f_0) signals, a small difference in time (whenever $f_0 \cdot \Delta t = 2n\pi$, for a small integer n) is sufficient to allow the shifted sine-Gaussian to properly approximate the exact waveform. This makes the likelihood itself very sensitive to a small perturbation of the two sky location parameters. However, there is one global maximum, although it can be barely distinguished at the center of the plot: it corresponds to the true injected values for the sky location parameters in this specific simulation. In the second plot, the surface is smooth and regular, with a global maximum for the injected true value.

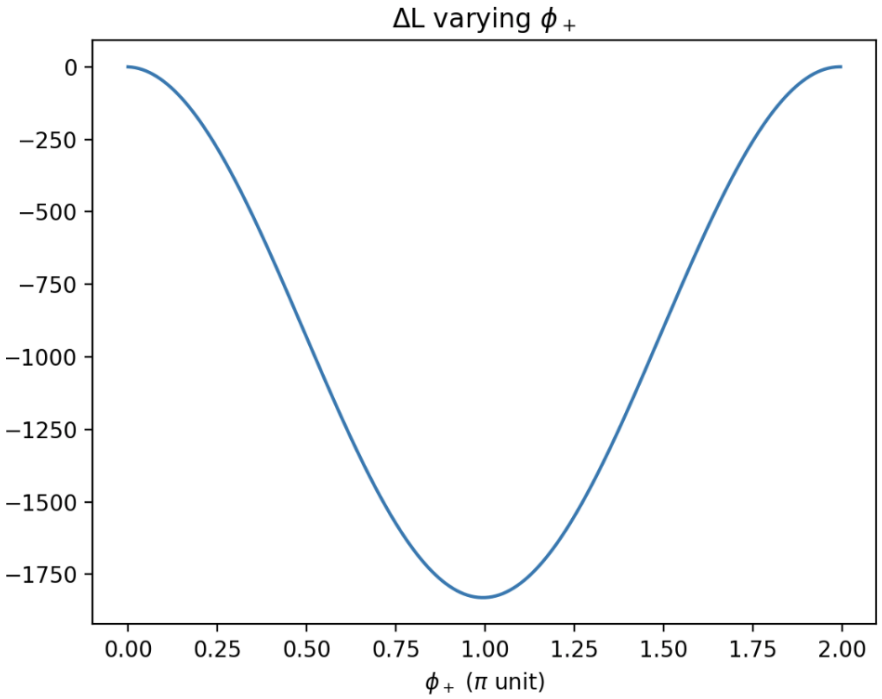

Figure A.1. *Likelihood as a function of* ϕ_+. On the vertical axis the difference between the value of the likelihood at the x-value and the value of the likelihood at the injected value is plotted, while on the horisontal axis $\phi_+ - \phi_{true}$ in units of π is reported.

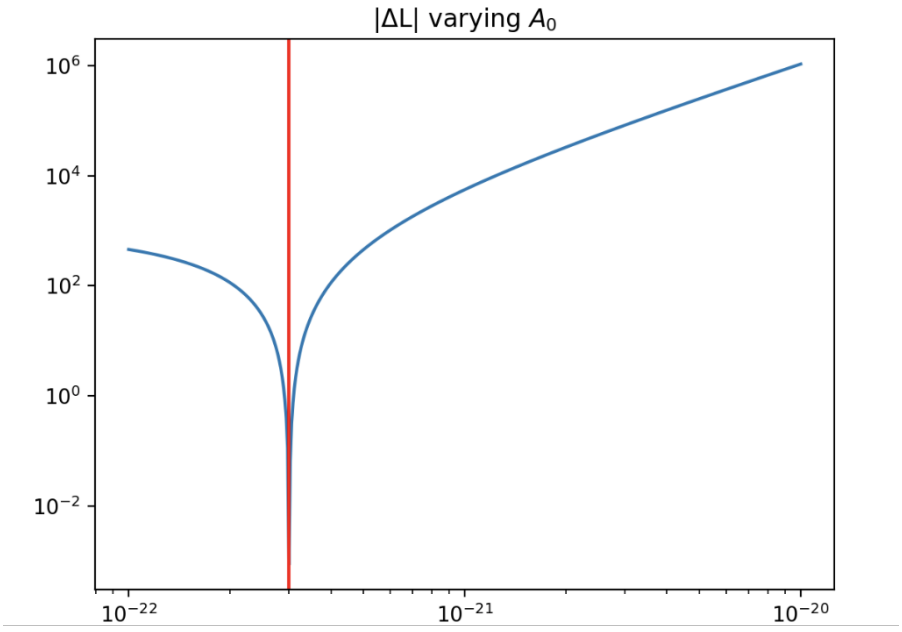

Figure A.2. *Likelihood as a function of* A_0. Same as Fig. A.1 but for the overall amplitude A_0, which is log-uniformly sampled around the injected value. The red line shows the true injected value for A_0.

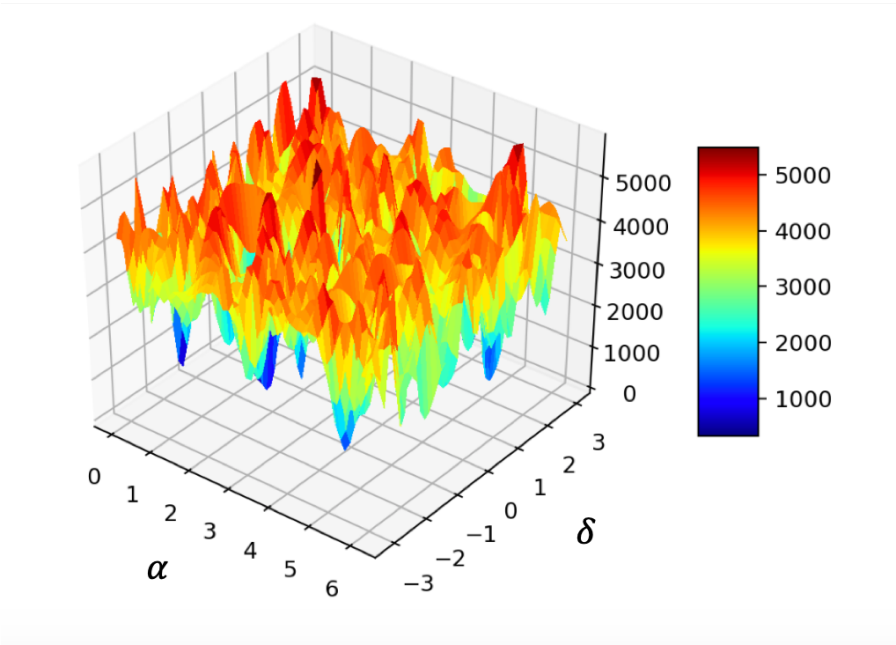

(a)

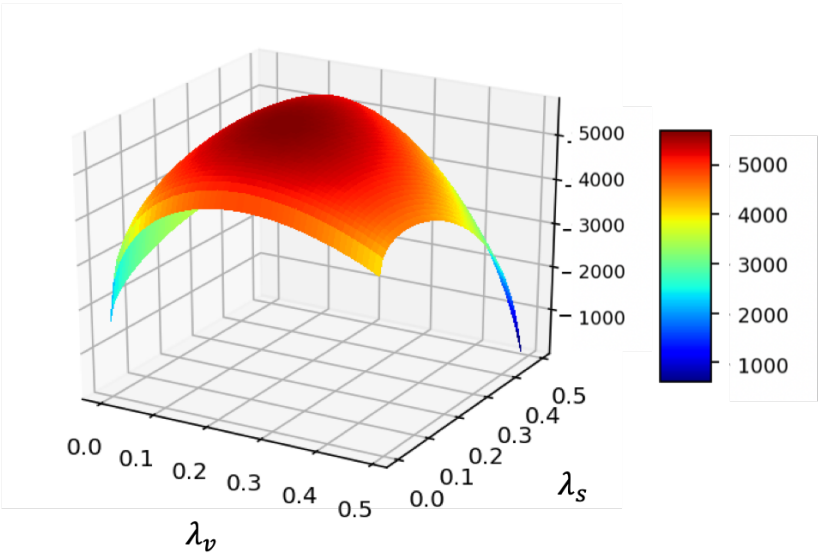

(b)

Figure A.3. *Two-dimensional study of the likehood* The likelihood 2D-surfaces are plotted as functions of right ascension and declination (α, δ) (a), and of the two hyper-parameters (λ_s, λ_v) (b).

Appendix B

Python Code

1 Bayesian Study of a nonGR polarized GW

1.1 Lib import

[ ]:
```
%matplotlib notebook
import pandas as pd
import numpy as np
from numpy import sin, cos
import matplotlib as mpl
import matplotlib.pyplot as plt
from mpl_toolkits.mplot3d import Axes3D
from matplotlib import cm
from matplotlib.ticker import LinearLocator, FormatStrFormatter
import pycbc
import astropy
from astropy import units as u
from astropy.coordinates import SkyCoord, EarthLocation
from astropy.time import Time
from astropy import constants as const
import warnings
import pycbc.psd
import pycbc.noise
import dynesty
import scipy.stats as sc
from pycbc.types.timeseries import TimeSeries
import matplotlib.mlab as mlab
from scipy.interpolate import interp1d
import time
from time import time
from dynesty import NestedSampler
import warnings
import pickle
from dynesty.utils import resample_equal
import corner
from scipy.stats import gaussian_kde
from dynesty import plotting as dyplot
```

1.2 Interferometers Data stored in a Dictionary

1.2.1 (taken from https://git.ligo.org/lscsoft/lalsuite/blob/master/lal/src/tools/LALDetectors.h)

[ ]:
```
data2arms=pd.read_csv("data2arms.txt", names=['name', 'value', 'comment'],
                      sep='=|#', engine='python')
```

[ ]:
```
warnings.filterwarnings("ignore", 'This pattern has match groups')

name=['VIRGO', 'LHO', 'LLO', 'LIO', 'KAGRA']
```

```
spec=['(LON|LAT|ELE)', '(LOCATION_X|LOCATION_Y|LOCATION_Z)',␣
 ↪'(X_DIRECTION_X|X_DIRECTION_Y|X_DIRECTION_Z)',␣
 ↪'(Y_DIRECTION_X|Y_DIRECTION_Y|Y_DIRECTION_Z)']

TwoArmDetectorData={}
dic={}
diclabel=['geodetic_pos', 'position', 'nx', 'ny']

for k in range(len(name)):
    for j in range(len(spec)):
        dic[diclabel[j]]=(data2arms[data2arms.name.str.contains(name[k]+'.
 ↪*'+spec[j])].value.to_numpy(float))
    TwoArmDetectorData[name[k]]= dic.copy()
```

1.3 Useful functions

[ ]:
```
def gmst_from_gps(gps_time):

    #519630571.347 gps is almost 0 gmst. This function computes the gmst_time in␣
 ↪radians for a given gps_time. If no gps_time=None, the gmst_time is set to␣
 ↪zero radians

    if gps_time is None:
        return 0
    else:
        return Time(gps_time, format='gps', scale='utc',location=(0,0)).
 ↪sidereal_time('mean').radian

def ColoredNoiseGen(psd,fs,name,signal):
    import pycbc.psd
    import pycbc.noise
    if psd is 'white':
        SNR=float(input('Please, provide a number for the SNR of the signal for␣
 ↪%s detector:' %name))
        noise=np.random.normal(0,1,len(signal))
        Spwr=np.linalg.norm(signal)/len(signal)
        Npwr=np.linalg.norm(noise)/len(signal)
        scale=(Spwr/(Npwr*SNR))
        return noise*scale
    else:
        while(psd is None):
            psd=input('Please, provide a psd-string to add colored noise to the␣
 ↪signal for %s detector \n (press enter to see all the possible psd or type␣
 ↪\'white\' for a constant unitary PSD):'%name)
            if(psd is ''):
                print(pycbc.psd.get_lalsim_psd_list())
```

```
                psd=None
                #Fix a seed for noise reproducibility
        return np.array(pycbc.noise.gaussian.noise_from_string(psd,len(signal),1.
↪/fs,seed=123))

def P2R(radii, angles):
    return radii * np.exp(1j*angles)
```

1.4 Source class implementation

[ ]:
```
class Source():

    def __init__ (self, right_ascension, declination, polarization_angle,␣
↪polarization_amplitude, gps_time=None, gmst_time=None, d_l=1):

        self.ra=right_ascension
        self.dec=declination
        self.pol_ang=polarization_angle
        self.pol_amp=polarization_amplitude
        self.dl=d_l

        if gmst_time is None:
            self.time=gmst_from_gps(gps_time)
        else:
            self.time=(2*np.pi*gmst_time)/86164.0905
```

1.5 Detector class implementation

[ ]:
```
class Detector():

    def __init__ (self, detector_name, geo_pos=None, pos=None):

        #geo_pos is a numpy ndarray with the location of the detector expressed␣
↪in geodetic coordinates [longitude,latitude,height]

        #pos is a numpy ndarray with the location of the detector expressed in␣
↪geocentric cartesian coordinates [x,y,z]

        self.name=str(detector_name)
        from astropy import units as u
        if pos is None:
            if geo_pos is None:
                raise Exception("Error! You must specify the position of the␣
↪interferometer on the earth!")
            else:
```

```
            self.position=EarthLocation.from_geodetic(lon=geo_pos[0]*u.rad,␣
↪lat=geo_pos[1]*u.rad, height=geo_pos[2])
        else:
            self.position=EarthLocation.from_geocentric(pos[0], pos[1], pos[2],␣
↪unit=u.m)

        self.latitude=self.position.lat
        self.longitude=self.position.lon

    def __str__(self):
        return "[Class Detector] name: %s"%self.name

    def antenna_pattern (self, right_ascension, declination, polarization_angle,␣
↪gmst_time=None, gps_time=None):

        ant_pat={}

        #Source in Celestial Coordinates (dec=pi/2-theta and ra=-phi in␣
↪spherical geocentric coordinates)

        ra=right_ascension
        dec=declination
        psi=polarization_angle

        #Compatibility check for multiple sources

        if len(np.atleast_1d(ra))!=len(np.atleast_1d(dec)) or len(np.
↪atleast_1d(ra))!=len(np.atleast_1d(psi)):
            raise Exception('Non compatible data for multiple sources: please␣
↪provide array of equal length for ra, dec, pol_ang!')
        if hasattr(gmst_time,'__len__') and len(np.atleast_1d(ra))!
↪=len(gmst_time):
            raise Exception('Non compatible data for multiple sources: please␣
↪provide array of equal length for times and sky location parameters!')
        if hasattr(gps_time,'__len__') and len(np.atleast_1d(ra))!=len(gps_time):
            raise Exception('Non compatible data for multiple sources: please␣
↪provide array of equal length for times and sky location parameters!')

        #Greenwhich hour angle of the source (which is -phi in spherical␣
↪geocentric coordinates)
        #if gmst_time is provided, gha is calculated directly using its value
        #if gps_time is provided, the corrspondent gmst_time is calculated from␣
↪it
        #if no times are provided, the gmst_time of the event is set to zero␣
↪(see gmst_from_gps function)
```

```
        if gmst_time is None:
            gha=gmst_from_gps(gps_time)-ra
        else:
            gha=gmst_time-ra

        #Given the position of the source in celestial coordinates, we want to␣
↪express them in geocentric coordinates.
        #We can express the celestial vector basis (X,Y,Z) in function of the␣
↪geocentric ones just performing three rotations consecutively where Z is along␣
↪the direction of propagation

        X=np.array([-cos(psi)*sin(gha)-sin(psi)*cos(gha)*sin(dec),
                    -cos(psi)*cos(gha)+sin(psi)*sin(gha)*sin(dec),
                    sin(psi)*cos(dec)])
        Y=np.array([sin(psi)*sin(gha)-cos(psi)*cos(gha)*sin(dec),
                    sin(psi)*cos(gha)+cos(psi)*sin(gha)*sin(dec),
                    cos(psi)*cos(dec)])
        Z=np.array([-cos(dec)*cos(gha),cos(dec)*sin(gha),-sin(dec)])

        #We can write the antenna pattern just computing out the double internal␣
↪product between the detector response and the basis.

        e_plus=np.einsum('i...,j...->ij...',X,X)-np.einsum('i...,j...->ij...
↪',Y,Y)
        e_cross=np.einsum('i...,j...->ij...',X,Y)+np.einsum('i...,j...->ij...
↪',Y,X)
        e_x=np.einsum('i...,j...->ij...',X,Z)+np.einsum('i...,j...->ij...',Z,X)
        e_y=np.einsum('i...,j...->ij...',Y,Z)+np.einsum('i...,j...->ij...',Z,Y)
        e_b=np.einsum('i...,j...->ij...',X,X)+np.einsum('i...,j...->ij...',Y,Y)
        e_l=np.einsum('i...,j...->ij...',Z,Z)

        plus=np.einsum('...ij,ij...->...',self.response,e_plus)
        cross=np.einsum('...ij,ij...->...',self.response,e_cross)
        x=np.einsum('...ij,ij...->...',self.response,e_x)
        y=np.einsum('...ij,ij...->...',self.response,e_y)
        b=np.einsum('...ij,ij...->...',self.response,e_b)
        l=np.einsum('...ij,ij...->...',self.response,e_l)

        for k in range(len(np.atleast_1d(ra))):
            ant_pat[k]={}
            ant_pat[k]['plus']=plus[k]
            ant_pat[k]['cross']=cross[k]
            ant_pat[k]['x']=x[k]
            ant_pat[k]['y']=y[k]
            ant_pat[k]['b']=b[k]
            #ant_pat[k]['l']=l[k]
```

```
        return ant_pat

    def amp_response(self, ra, dec, pol_ang, pol_amp, gmst_time=None,␣
↪gps_time=None):
        amp_res={}
        for k in pol_amp.keys():
            amp=0
            for i, mode in enumerate(['plus', 'cross','x','y','b']):
                amp+=pol_amp[k][mode]*self.antenna_pattern(ra, dec, pol_ang,␣
↪gmst_time=gmst_time, gps_time=gps_time)[k][mode]
            amp_res[k]=amp
        return amp_res

    def time_delay_from_location(self, location, right_ascension, declination,␣
↪gmst_time=None, gps_time=None):

    #Let be "location" a ndarray representing a reference position in cartesian␣
↪geocentric coordinates where the GW signal is detected at a given gps time:␣
↪this method returns the time delay at which GW signal is seen by the detector,␣
↪given the position in the sky (in celestial coordinates) of the source. In␣
↪other words, let t1 be the arrival time in this detector and t2 the arrival␣
↪time in the location, this method returns t1-t2 in seconds.

        #Location of the source in Celestial Coordinates (dec=pi/2-theta,␣
↪ra=-phi in spherical geocentric coordinates)

        ra=np.atleast_1d(right_ascension)
        dec=np.atleast_1d(declination)

        #Compatibility check for multiple sources

        if len(ra)!=len(dec):
            raise Exception('Non compatible data for multiple sources: please␣
↪provide array of equal length for ra, dec, pol_ang!')
        if hasattr(gmst_time,'__len__') and len(ra)!=len(gmst_time):
            raise Exception('Non compatible data for multiple sources: please␣
↪provide array of equal length for times and sky location parameters!')
        if hasattr(gps_time,'__len__') and len(ra)!=len(gps_time):
            raise Exception('Non compatible data for multiple sources: please␣
↪provide array of equal length for times and sky location parameters!')


        #Greenwhich hour angle of the source (-phi in spherical geocentric␣
↪coordinates)
        #if gmst_time is provided, gha is calculated directly using its value
```

```
        #if gps_time is provided, the corrspondent gmst_time is calculated from␣
↪it
        #if no times are provided, the gmst_time of the event is set to zero

        if gmst_time is None:
            gha=gmst_from_gps(gps_time)-ra
        else:
            gha=gmst_time-ra

        #unit vector representing source direction

        versor=cos(dec)*cos(gha),-cos(dec)*sin(gha),sin(dec)

        #difference vector between positions
        deltav= np.array([self.position.x.value, self.position.y.value, self.
↪position.z.value]) - location

        #time of flight
        dt_vector=-deltav.dot(versor)/const.c.value

        deltat={}
        for k in range(len(ra)):
            deltat[k]=dt_vector[k]

        return deltat


    def time_delay_from_earth_center(self, right_ascension, declination,␣
↪gmst_time=None, gps_time=None):
        return self.time_delay_from_location(np.array([0,0,0]), right_ascension,␣
↪declination, gmst_time, gps_time)

    def time_delay_from_detector(self, other_detector, right_ascension,␣
↪declination, gmst_time=None, gps_time=None):
        location=np.array([other_detector.position.x.value, other_detector.
↪position.y.value, other_detector.position.z.value])
        return self.time_delay_from_location(location, right_ascension,␣
↪declination, gmst_time, gps_time)

    def SinGausResponse(self, source, Omega=628, tau=0.1, T=32, fs=4096,␣
↪plot=False, noise=False, psd=None):

        #Constructing the signal

        t_0=source.time*86164.0905/(2*np.pi)
```

```
        A_comp=self.amp_response(source.ra, source.dec, np.zeros(len(np.
↪atleast_1d(source.ra))), source.pol_amp, gmst_time=source.time)

        dt_dict=self.time_delay_from_earth_center(source.ra, source.dec,␣
↪gmst_time=source.time)

        timeseries=np.arange(t_0-T/2,t_0+T/2,1/fs)

        response={k: {'A': np.absolute(A_comp[k])/source.dl,
                      'phi': np.angle(A_comp[k])-Omega*(dt_dict[k]+t_0),
                      'dt': dt_dict[k]+t_0,
                      'pure_signal': np.absolute(A_comp[k])/source.dl*np.
↪cos(Omega*(timeseries-t_0-dt_dict[k]) +  np.angle(A_comp[k]))*np.
↪exp(-(timeseries-t_0-dt_dict[k])**2/tau**2)} for k in A_comp.keys()}

        if plot is True:
            for k in A_comp.keys():
                plt.tight_layout()
                plt.plot(timeseries, response[k]['signal'])
                plt.title('Response of %s - Source no. %s'%(self.name,k))
                plt.ylabel('R [a.u.]')
                plt.xlabel('Greenwich Mean Sidereal Time (s)')
                plt.show()
        for k in response.keys():
            if noise is True:
                response[k]['response'] = response[k]['pure_signal'] +␣
↪ColoredNoiseGen(psd,fs,self.name,response[k]['pure_signal'])
            else:
                response[k]['response'] = response[k]['pure_signal']
        return response

    def show_map(self):
        fig = plt.figure(figsize=(7,4))
        plt.title('Position of "%s" detector'%self.name)
        map = Basemap(projection='cyl', lat_0 = 0, lon_0 = 0, resolution = 'c',␣
↪area_thresh = 0.1, llcrnrlon=-180.0, llcrnrlat=-90.0, urcrnrlon=180.0,␣
↪urcrnrlat=90.0)
        map.drawcoastlines()
        map.drawparallels(np.arange(-90,90,45),labels=[1,1,0,1])
        map.drawmeridians(np.arange(-180,180,45),labels=[1,1,0,1])
        map.drawmapboundary()
        map.scatter(self.longitude.value,self.latitude.value,c='red',latlon=True)
        plt.show()
```

[ ]:
```
class TwoArmDetector(Detector):

    def __init__ (self, detector_name, n_x, n_y, geo_pos=None, pos=None):
```

```
        Detector.__init__(self, detector_name, geo_pos, pos)
        self.nx=n_x
        self.ny=n_y
        self.response=0.5*(np.einsum('i,j->ij', self.nx, self.nx) - np.
↪einsum('i,j->ij', self.ny, self.ny))

    def __str__(self):
        return "[Class TwoArmDetector] name: %s"%self.name

    def display(self):
        print("%s is a Two-Arm Detector - Geodetic Coordinates \n\t[lon, lat,␣
↪height] = [%s, %s, %s]" %(self.name, self.position.lon, self.position.lat,␣
↪self.position.height))
```

[ ]:
```
class ThreeArmDetector(Detector):

    def __init__ (self, detector_name, n_x, n_y, n_z, geo_pos=None, pos=None):

        Detector.__init__(self,detector_name,geo_pos,pos)
        self.nx=n_x
        self.ny=n_y
        self.nz=n_z
        self.response_x=0.5*(np.einsum('i,j->ij', self.nx, self.nx) - np.
↪einsum('i,j->ij', self.ny, self.ny))
        self.response_y=0.5*(np.einsum('i,j->ij', self.ny, self.ny) - np.
↪einsum('i,j->ij', self.nz, self.nz))
        self.response_z=0.5*(np.einsum('i,j->ij', self.nz, self.nz) - np.
↪einsum('i,j->ij', self.nx, self.nx))
        self.response=np.array([self.response_x, self.response_y, self.
↪response_z])

    def __str__(self):
        return "[Class ThreeArmDetector] name: %s"%self.name

    def display(self):
        print("%s is a Three-Arm Detector - Geodetic Coordinates \n\t[lon, lat,␣
↪height] = [%s, %s, %s]" %(self.name, self.position.lon, self.position.lat,␣
↪self.position.height))
```

[ ]:
```
class Network():

    def __init__(self,name):
        self.name=name
        self.web={}
```

```
    def __str__(self):
        return "[Class Network] composed of %i detectors \n(use display method␣
↪to generate the list of detectors included)"%len(self.web)

    def display(self):
        print("Network: %s is composed by the following %i detectors:" %(self.
↪name, len(self.web)))
        for k in self.web.keys():
            self.web[k].display()

    def get_lat(self):
        return {k: self.web[k].latitude.value for k in self.web.keys()}

    def get_lon(self):
        return {k: self.web[k].longitude.value for k in self.web.keys()}

    def add_detector(self,detector):
        self.web[detector.name] = detector

    def remove_detector(self,detector):
        self.web.pop(detector.name)

    def amp_response(self,ra,dec,pol_ang,pol_amp,gmst=None,gps=None):
        res=self.web[list(self.web.keys())[0]].amp_response(ra, dec, pol_ang,␣
↪pol_amp, gmst_time=gmst, gps_time=gps).keys()
        return {k: {self.web[i].name: self.web[i].amp_response(ra, dec, pol_ang,␣
↪pol_amp, gmst_time=gmst, gps_time=gps)[k] for i in self.web.keys()} for k in␣
↪res}

    def time_response(self,ra,dec,gmst=None,gps=None):
        res=self.web[list(self.web.keys())[0]].time_delay_from_earth_center(ra,␣
↪dec, gmst_time=gmst, gps_time=gps).keys()
        return {k: {self.web[i].name: self.web[i].
↪time_delay_from_earth_center(ra, dec, gmst_time=gmst, gps_time=gps)[k] for i␣
↪in self.web.keys()} for k in res}

    def Response_SNR(self, source,  Omega=628, tau=0.1, T=32, fs=4096,␣
↪plot_res=False, plot_SNR=False, plot_PSD=False, noise=False, psd=None):

        t_0=source.time*86164.0905/(2*np.pi)
        timeseries=np.arange(t_0-T/2, t_0+T/2, 1/fs)

        if psd is None: psd={i: None for i in self.web.keys()}
        if psd is 'white': psd={i: 'white' for i in self.web.keys()}
        res=self.web[list(self.web.keys())[0]].SinGausResponse(source,␣
↪Omega=Omega, tau=tau, T=T, fs=fs).keys()
```

```
        response={k: {self.web[i].name: self.web[i].SinGausResponse(source,␣
↪Omega=Omega, tau=tau, T=T, fs=fs, noise=noise, psd=psd[i])[k] for i in self.
↪web.keys()} for k in res}

        if plot_res is True:
            for k in response.keys():
                fig, ax = plt.subplots(nrows=len(self.web), sharex=True,␣
↪sharey=True, figsize=(10,10))
                fig.subplots_adjust(hspace=0.3)
                fig.suptitle('Signal of the source %s'%k)
                for i,j in enumerate(self.web.keys()):
                    ax[i].plot(timeseries, response[k][self.web[j].
↪name]['response'])
                    ax[i].set_title('Response of %s'%(self.web[j].name))
                    ax[i].set_ylabel('R [a.u.]')
                    ax[i].set_xticks(np.arange(t_0-T/2,t_0+T/2,T/10))
                    ax[i].grid(True)
                ax[len(self.web)-1].set_xlabel('Greenwich Mean Sidereal Time␣
↪(s)')
                plt.show()

        psd={k: pycbc.psd.analytical.from_string(name_psd[k],fs*T,1/T,10) for k␣
↪in self.web.keys()}
        NFFT=4*fs
        f_min=10
        f_nyq=fs/2
        SNR={}

        for k in response.keys():
            SNR[k]={}
            for i in response[k].keys():
                data_timeser=TimeSeries(response[k][i]['response'],1./fs)
                template_timeser=TimeSeries(response[k][i]['pure_signal'],1./fs)
                SNR_complex=np.array(pycbc.filter.matchedfilter.
↪matched_filter(template_timeser, data_timeser, psd[i],␣
↪low_frequency_cutoff=10))
                peaksample=int((response[k][i]['dt']+T/2-t_0)*fs)
                SNR_complex = np.roll(SNR_complex, peaksample)
                SNR[k][i] = abs(SNR_complex)

                if plot_SNR is True:
                    plt.figure(figsize=(10,8))
                    plt.plot(np.arange(t_0-T/2, t_0+T/2, 1/
↪fs),SNR[k][i],'r',label='SNR(t)')
                    plt.grid()
                    plt.ylabel('SNR')
```

```
                    plt.xlabel('Greenwich Mean Sidereal Time (s)')
                    plt.legend(loc='upper left')
                    plt.title('Matched filter SNR around Event %d - Detector␣
↪%s'%(k,i))
                    plt.show()

                if plot_PSD is True:
                    data_psd, freqs = mlab.psd(response[k][i]['response'], Fs =␣
↪fs, NFFT = NFFT)
                    plt.figure(figsize=(8,3))
                    plt.loglog(freqs, np.sqrt(data_psd),'g',label='Strain Event␣
↪%d - Detector %s'%(k,i))
                    plt.loglog(psd[i].sample_frequencies, np.sqrt(psd[i]),'b',␣
↪label='Sqrt(Analytical PSD) - Detector %s'%i)
                    plt.grid()
                    plt.ylabel('ASD (strain/rtHz)')
                    plt.xlabel('Freq (Hz)')
                    plt.xlim(f_min,f_nyq)
                    plt.ylim(1e-25,1e-20)
                    plt.legend(loc='upper center')
                    plt.show()

        SNR_max={k: {i: np.max(SNR[k][i]) for i in response[k].keys()} for k in␣
↪response.keys()}
        response['SNR(t)']=SNR

        return response, SNR_max

    def show_map(self):
        from mpl_toolkits.basemap import Basemap
        fig = plt.figure(figsize=(7,4))
        plt.title('Network "%s" detectors'%self.name)
        map = Basemap(projection='moll', lat_0 = 0, lon_0 = 0)
        map.drawcoastlines()
        map.drawparallels(np.arange(-90,90,45),labels=[1,1,0,1])
        map.drawmapboundary()
        map.scatter(np.array(list(self.get_lon().values())), np.array(list(self.
↪get_lat().values())), c='red', latlon=True)
        plt.show()
```

2 Simulation of the response of a network of interferometers to GW signal

2.1 Creation of the network

[ ]:
```
OldNet=Network("LIGO-Virgo")
OldNet.add_detector(TwoArmDetector('VIRGO', TwoArmDetectorData['VIRGO']['nx'],␣
↪TwoArmDetectorData['VIRGO']['ny'],␣
↪pos=TwoArmDetectorData['VIRGO']['position']))
OldNet.add_detector(TwoArmDetector('LHO', TwoArmDetectorData['LHO']['nx'],␣
↪TwoArmDetectorData['LHO']['ny'], pos=TwoArmDetectorData['LHO']['position']))
OldNet.add_detector(TwoArmDetector('LLO', TwoArmDetectorData['LLO']['nx'],␣
↪TwoArmDetectorData['LLO']['ny'], pos=TwoArmDetectorData['LLO']['position']))

Net=Network("TheFive")
for k in TwoArmDetectorData:
    Net.add_detector(TwoArmDetector(k,TwoArmDetectorData[k]['nx'],␣
↪TwoArmDetectorData[k]['ny'], pos=TwoArmDetectorData[k]['position']))
```

2.2 Creation of a random source uniformly distributed on the celestial sphere, at random sidereal time

2.2.1 Generating function

[ ]:
```
def generate_random_sky_location (N=100,plot=False):

    cos_theta, ra = np.random.uniform(-1,1,N), np.random.uniform(0,2*np.pi,N)
    dec = np.arcsin(cos_theta)

    if plot is True:
        fig=plt.figure()
        n=80
        cos_theta0, phi0 = np.linspace(-1, 1, n), np.linspace(0, 2*np.pi, n)
        theta0 = np.arccos(cos_theta0)
        THETA, PHI = np.meshgrid(theta0, phi0, indexing = "ij")
        R=np.zeros((n,n))
        for i in range(n):
            for j in range(n):
                R[i,j]=1
        X = R * np.sin(THETA) * np.cos(PHI)
        Y = R * np.sin(THETA) * np.sin(PHI)
        Z = R * np.cos(THETA)
        ax = fig.add_subplot(111, projection='3d')
        ax.set_xlim(-1,1)
        ax.set_ylim(-1,1)
        ax.set_zlim(-1,1)
        ax.set_xlabel('x')
```

```
        ax.set_ylabel('y')
        ax.set_zlabel('z')
        ax.set_xticks(np.arange(-1,1.2,0.5))
        ax.set_yticks(np.arange(-1,1.2,0.5))
        ax.set_zticks(np.arange(-1,1.2,0.5))
        plot = ax.plot_surface(X, Y, Z, rstride=1, cstride=1, linewidth=0,␣
 ↪alpha=0.2, antialiased=False)
        xi=1.01*np.cos(dec)*np.cos(ra)
        yi=-1.01*np.cos(dec)*np.sin(ra)
        zi=1.01*np.sin(dec)
        ax.scatter(xi, yi, zi, s=10, c='r', zorder=10)
        x, y, z = np.zeros((3,3))
        u, v, w = np.array([[1.5,0,0],[0,1.5,0],[0,0,1.5]])
        ax.quiver(x,y,z,u,v,w, arrow_length_ratio=0.05, color='black')
        ax.view_init(30,45)
        ax.figure.set_size_inches(5,5)
        ax.set_title('%d sources uniformily distributed \non the Celestial␣
 ↪Sphere'%N)
        plt.show()
    return ra, dec


def generate_random_sidereal_time ():
    return np.random.uniform(0,86164.0905,1)[0]

def generate_random_amplitudes(lambda_v,lambda_s,A_0=1e-21,N=10):
    ampl={}
    for i in range(N):
        phi=np.random.uniform(0,2*np.pi,5)
        f=np.random.uniform(0,1,2)
        e_cross,e_y=np.sqrt(1-lambda_v-lambda_s)*f[0], np.sqrt(lambda_v)*f[1]
        e_plus,e_x=np.sqrt(1-lambda_v-lambda_s-e_cross**2), np.
 ↪sqrt(lambda_v-e_y**2)
        e_s=np.sqrt(lambda_s)
        r=A_0*np.array([e_plus,e_cross,e_x,e_y,e_s])
        c=P2R(r,phi)
        ampl[i]={}
        ampl[i]['plus']= c[0]
        ampl[i]['cross']= c[1]
        ampl[i]['x']= c[2]
        ampl[i]['y']= c[3]
        ampl[i]['b']= c[4]
    return ampl

def generate_random_sources(lambda_v,lambda_s,A_0=1,N=10,plot=False):
    ra,dec=generate_random_sky_location(N=N,plot=plot)
    t_0=0
```

```
    amplitude=generate_random_amplitudes(lambda_v,lambda_s,A_0=A_0,N=N)
    psi=np.zeros(N)
    return Source(ra,dec,psi,amplitude,gmst_time=t_0) #WARNING: MULTIPLE TIMES␣
↪NOT IMPLEMENTED
```

2.2.2 Creation of the Source

[ ]:
```
lambda_v=0.1
lambda_s=0.1
A_0=1e-22
T=4
fs=4096
sourceran=generate_random_sources(lambda_v,lambda_s,N=1,A_0=A_0)
t_0=0
true={'ra': sourceran.ra[0], 'dec': sourceran.dec[0],
      'phi_plus': (2*np.pi+np.angle(sourceran.pol_amp[0]['plus']))%(2*np.pi),
      'phi_cross': (2*np.pi+np.angle(sourceran.pol_amp[0]['cross']))%(2*np.pi),
      'phi_x': (2*np.pi+np.angle(sourceran.pol_amp[0]['x']))%(2*np.pi),
      'phi_y': (2*np.pi+np.angle(sourceran.pol_amp[0]['y']))%(2*np.pi),
      'phi_s': (2*np.pi+np.angle(sourceran.pol_amp[0]['b']))%(2*np.pi),
      'lambda_v': (np.abs(sourceran.pol_amp[0]['x'])**2+np.abs(sourceran.
↪pol_amp[0]['y'])**2)/A_0**2,
      'lambda_s': np.abs(sourceran.pol_amp[0]['b'])**2/A_0**2,
      'epsilon_cross': np.abs(sourceran.pol_amp[0]['cross'])/A_0,
      'epsilon_y': np.abs(sourceran.pol_amp[0]['y'])/A_0,'A_0': A_0}
```

3 Toy model response of the network for a single source with a Gaussian Colored Noise with PSD & SNR study

[ ]:
```
name_psd={'VIRGO':'AdvVirgo', 'LHO':'aLIGOAPlusDesignSensitivityT1800042', 'LLO':
↪'aLIGOAPlusDesignSensitivityT1800042', 'LIO':
↪'aLIGOAPlusDesignSensitivityT1800042', 'KAGRA':'KAGRA'}
response,SNR=Net.Response_SNR(sourceran, T=T, plot_res=True, plot_SNR=True,␣
↪plot_PSD=True, noise=True, psd=name_psd)
```

4 Recap

[ ]:
```
print(true)
print(SNR)
true_arr=np.array(list(true.values()))
```

5 Bayesian analysis

5.1 Preliminaries

[ ]:
```
datafreq = np.fft.rfftfreq((fs*T),1/fs)
df=datafreq[1]-datafreq[0]
psd={}
data_fft={}

for k in response[0].keys():

    data_fft[k]=np.fft.rfft(response[0][k]['response'])

    psd_var=np.interp(datafreq,np.array(pycbc.psd.analytical.
 ↪from_string(name_psd[k], fs*T,1/T,10).sample_frequencies), np.array(pycbc.psd.
 ↪analytical.from_string(name_psd[k], fs*T,1/T,10)))
    psd[k]=psd_var

def plot_result(res, thruths, labels, filename=None):
    from dynesty import plotting as dyplot
    plt.tight_layout()
    cfig, caxes = dyplot.cornerplot(res, color='blue', truths=truths,␣
 ↪truth_color='red', show_titles=True, max_n_ticks=5, quantiles=None,␣
 ↪labels=labels)
    fg, ax = dyplot.cornerpoints(res, cmap='plasma', truths=truths, kde=False,␣
 ↪labels=labels)
    fig, axes = dyplot.traceplot(res, truths=truths, truth_color='red',␣
 ↪kde=False, show_titles=True, trace_cmap='viridis', connect=True,␣
 ↪connect_highlight=range(5), labels=labels)
    if filename is not None:
        fig.savefig(filename+'_trace.png')
        cfig.savefig(filename+'_corn.png')
        fg.savefig(filename+'_pcorn.png')

allpar=False
sixpar=False
skypar=False
amppar=True
lambdapar=True
```

5.2 Full estimation of the 12 parameters

[ ]:
```
if allpar is True:
    def prior_transform(u):
        """Transforms the uniform random variable `u ~ Unif[0., 1.)`
        to the parameter of interest
        """
```

```
        x=np.array(u)

        # right_ascension \in [0, 2pi]
        x[0] = 2*np.pi*np.mod(u[0],1)

        # cos(declination) uniform \in [-1., 1]
        x[1] = np.arcsin(2.*np.minimum(np.maximum(u[1], abs(u[1])), 2 - u[1])- 1.
↪)

        # phi_p \in [0, 2pi]
        x[2:7]=2*np.pi*np.mod(u[2:7],1)

        # lambda_v \in [0,1)
        x[7]=u[7]

        # lambda_s \in [0,lambda_v)
        x[8]=u[8]*(1-u[7])

        # epsilon_cross \in [0,sqrt(1-lambda_v-lambda_s))
        x[9]=u[9]*np.sqrt(1-u[7]-u[8]*(1-u[7]))

        # epsilon_y \in [0,sqrt(lambda_v))
        x[10]=u[10]*np.sqrt(u[7])

        # A_0 log-uniform \in [1e-22,1e-20)
        x[11]=10.** (u[11]*2 - 22.)

        return x

    def model_fft(theta,detector,T,fs,Omega=628,tau=0.1,event=0):
            #Building the source_amplitude
            phi=theta[2:7]
            e_plus,e_x=np.sqrt(1-theta[7]-theta[8]-theta[9]**2), np.
↪sqrt(theta[7]-theta[10]**2)
            e_cross,e_y=theta[9],theta[10]
            e_s=np.sqrt(theta[8])
            r=theta[11]*np.array([e_plus,e_cross,e_x,e_y,e_s])
            c=P2R(r,phi)
            ampl={event: {}}
            ampl[event]['plus']= c[0]
            ampl[event]['cross']= c[1]
            ampl[event]['x']= c[2]
            ampl[event]['y']= c[3]
            ampl[event]['b']= c[4]
            so=Source(theta[0], theta[1], np.array([0]), ampl,gmst_time=t_0)
            res=detector.SinGausResponse(so, T=T, fs=fs, Omega=Omega, tau=tau)
            return np.fft.rfft(res[event]['pure_signal'])
```

```
    def lnlike(theta):
        delta_fft={}
        delta_fft_sqr={}
        exp=0
        for k in response[0].keys():
            if model_fft(theta,detector=Net.web[k],T=T,fs=fs) is None: return␣
↪-np.inf
            delta_fft[k]=data_fft[k]-model_fft(theta,detector=Net.
↪web[k],T=T,fs=fs)
            delta_fft_sqr[k]=np.abs(delta_fft[k])**2
            exp+=np.sum(-2*(delta_fft_sqr[k][T*10:]/psd[k][T*10:])*df/fs**2-0.
↪5*np.log(np.pi*T*psd[k][T*10:]/2))
        return exp

    truths=true_arr
    labels=list(true.keys())
    t1=time()
    sampler = NestedSampler(lnlike,␣
↪prior_transform,12,periodic=[0,1,2,3,4,5,6],sample='rwalk')
    sampler.run_nested(dlogz=100)
    results = sampler.results
    t1_end=time()
    plot_result(results,truths,labels)
```

5.3 Sky-location+Ampl param estimate (6 params)

[ ]:
```
if sixpar is True:
    def prior_transform(u):
        """Transforms the uniform random variable `u ~ Unif[0., 1.)`
        to the parameter of interest
        """
        x=np.array(u)

        # right_ascension \in [0, 2pi]
        x[0] = 2*np.pi*np.mod(u[0], 1)

        # cos(declination) uniform \in [-1., 1]
        x[1] = np.arcsin(2.*np.minimum(np.maximum(u[1], abs(u[1])), 2 - u[1])- 1.
↪)

        # lambda_v \in [0,1)
        x[2]=u[2]

        # lambda_s \in [0,lambda_v)
        x[3]=u[3]*(1-u[2])
```

```
        # epsilon_cross \in [0,sqrt(1-lambda_v-lambda_s))
        x[4]=u[4]*np.sqrt(1-u[2]-u[3]*(1-u[2]))

        # epsilon_y \in [0,sqrt(lambda_v))
        x[5]=u[5]*np.sqrt(u[2])

        return x

    def model_fft(theta,detector,T,fs,Omega=628,tau=0.1,event=0):
            #Building the source_amplitude
            phi=true_arr[2:7]
            e_plus,e_x=np.sqrt(1-theta[2]-theta[3]-theta[4]**2),np.
↪sqrt(theta[2]-theta[5]**2)
            e_cross,e_y=theta[4],theta[5]
            e_s=np.sqrt(theta[3])
            r=true_arr[11]*np.array([e_plus,e_cross,e_x,e_y,e_s])
            c=P2R(r,phi)
            ampl={event: {}}
            ampl[event]['plus']= c[0]
            ampl[event]['cross']= c[1]
            ampl[event]['x']= c[2]
            ampl[event]['y']= c[3]
            ampl[event]['b']= c[4]
            so=Source(theta[0],theta[1],np.array([0]),ampl,gmst_time=t_0)
            res=detector.SinGausResponse(so,T=T,fs=fs,Omega=Omega,tau=tau)
            return np.fft.rfft(res[event]['pure_signal'])

    def lnlike(theta):
        delta_fft={}
        delta_fft_sqr={}
        exp=0
        for k in response[0].keys():
            if model_fft(theta,detector=Net.web[k],T=T,fs=fs) is None: return␣
↪-np.inf
            delta_fft[k]=data_fft[k]-model_fft(theta,detector=Net.
↪web[k],T=T,fs=fs)
            delta_fft_sqr[k]=np.abs(delta_fft[k])**2
            exp+=np.sum(-2*(delta_fft_sqr[k][T*10:]/psd[k][T*10:])*df/fs**2-0.
↪5*np.log(np.pi*T*psd[k][T*10:]/2))
        return exp

    truths=np.
↪array([true_arr[0],true_arr[1],true_arr[7],true_arr[8],true_arr[9],true_arr[10]])
    labels=[list(true.keys())[0],list(true.
↪keys())[1],'$\lambda_v$','$\lambda_s$','$\epsilon_x$','$\epsilon_y$']
```

```
    t2=time()
    halfsampler = NestedSampler(lnlike,␣
↪prior_transform,6,periodic=[0,1],sample='rwalk')
    halfsampler.run_nested(dlogz=1)
    halfresults = halfsampler.results
    t2_end=time()
    plot_result(halfresults,truths,labels)
```

5.4 Sky-location estimate (ra/dec)

[ ]:
```
if skypar is True:
    def prior_transform(u):
        """Transforms the uniform random variable `u ~ Unif[0., 1.)`
        to the parameter of interest
        """
        x=np.array(u)

        # right_ascension \in [0, 2pi]
        x[0] = 2*np.pi*np.mod(u[0], 1)

        # cos(declination) uniform \in [-1., 1]
        x[1] = np.arcsin(2.*np.minimum(np.maximum(u[1], abs(u[1])), 2 - u[1])- 1.
↪)

        return x

    def model_fft(theta,detector,T,fs,Omega=628,tau=0.1,event=0):

            #Building the source_amplitude
            phi=true_arr[2:7]
            e_plus,e_x=np.sqrt(1-true_arr[7]-true_arr[8]-true_arr[9]**2),np.
↪sqrt(true_arr[7]-true_arr[10]**2)
            e_cross,e_y=true_arr[9],true_arr[10]
            e_s=np.sqrt(true_arr[8])
            r=true_arr[11]*np.array([e_plus,e_cross,e_x,e_y,e_s])
            c=P2R(r,phi)
            ampl={event: {}}
            ampl[event]['plus']= c[0]
            ampl[event]['cross']= c[1]
            ampl[event]['x']= c[2]
            ampl[event]['y']= c[3]
            ampl[event]['b']= c[4]
            so=Source(theta[0],theta[1],np.array([0]),ampl,gmst_time=t_0)
            res=detector.SinGausResponse(so,T=T,fs=fs,Omega=Omega,tau=tau)
            return np.fft.rfft(res[event]['pure_signal'])
```

```
    def lnlike(theta):
        delta_fft={}
        delta_fft_sqr={}
        exp=0
        for k in response[0].keys():
            if model_fft(theta,detector=Net.web[k],T=T,fs=fs) is None: return␣
↪-np.inf
            delta_fft[k]=data_fft[k]-model_fft(theta,detector=Net.
↪web[k],T=T,fs=fs)
            delta_fft_sqr[k]=np.abs(delta_fft[k])**2
            exp+=np.sum(-2*(delta_fft_sqr[k][T*10:]/psd[k][T*10:])*df/fs**2-0.
↪5*np.log(np.pi*T*psd[k][T*10:]/2))
        return exp

    truths=true_arr[0:2]
    labels=list(true.keys())[0:2]
    t3=time()
    skysampler = NestedSampler(lnlike, prior_transform,2,periodic=[0,1])
    skysampler.run_nested()
    skyresults = skysampler.results
    t3_end=time()
    plot_result(skyresults,truths,labels)
```

5.5 Lambda/Epsilon estimate (4 params)

[ ]:
```
if amppar is True:
    def prior_transform(u):
        """Transforms the uniform random variable `u ~ Unif[0., 1.)`
        to the parameter of interest
        """
        x=np.array(u)

        # lambda_v \in [0,1)
        x[0]=u[0]

        # lambda_s \in [0,lambda_v)
        x[1]=u[1]*(1-u[0])

        # epsilon_cross \in [0,sqrt(1-lambda_v-lambda_s))
        x[2]=u[2]*np.sqrt(1-u[0]-u[1]*(1-u[0]))

        # epsilon_y \in [0,sqrt(lambda_v))
        x[3]=u[3]*np.sqrt(u[0])

        return x
```

```
   def model_fft(theta,detector,T,fs,Omega=628,tau=0.1,event=0):
           #Building the source_amplitude
           phi=true_arr[2:7]
           e_plus,e_x=np.sqrt(1-theta[0]-theta[1]-theta[2]**2),np.
↪sqrt(theta[0]-theta[3]**2)
           e_cross,e_y=theta[2],theta[3]
           e_s=np.sqrt(theta[1])
           r=true_arr[11]*np.array([e_plus,e_cross,e_x,e_y,e_s])
           c=P2R(r,phi)
           ampl={event: {}}
           ampl[event]['plus']= c[0]
           ampl[event]['cross']= c[1]
           ampl[event]['x']= c[2]
           ampl[event]['y']= c[3]
           ampl[event]['b']= c[4]
           so=Source(true_arr[0],true_arr[1],np.array([0]),ampl,gmst_time=t_0)
           res=detector.SinGausResponse(so,T=T,fs=fs,Omega=Omega,tau=tau)
           return np.fft.rfft(res[event]['pure_signal'])

   def lnlike(theta):
       delta_fft={}
       delta_fft_sqr={}
       exp=0
       for k in response[0].keys():
           if model_fft(theta,detector=Net.web[k],T=T,fs=fs) is None: return␣
↪-np.inf
           delta_fft[k]=data_fft[k]-model_fft(theta,detector=Net.
↪web[k],T=T,fs=fs)
           delta_fft_sqr[k]=np.abs(delta_fft[k])**2
           exp+=np.sum(-2*(delta_fft_sqr[k][T*10:]/psd[k][T*10:])*df/fs**2-0.
↪5*np.log(np.pi*T*psd[k][T*10:]/2))
       return exp

   truths=true_arr[7:11]
   labels=['$\lambda_v$','$\lambda_s$','$\epsilon_x$','$\epsilon_y$']
   t4=time()
   ampsampler = NestedSampler(lnlike, prior_transform,4)
   ampsampler.run_nested()
   ampresults = ampsampler.results
   t4_end=time()
   plot_result(ampresults,truths,labels)
```

5.6 Lambdas estimate

```
[ ]: if lambdapar is True:
    def prior_transform(u):
        """Transforms the uniform random variable `u ~ Unif[0., 1.)`
        to the parameter of interest
        """
        x=np.array(u)
        x[0]=u[0]                                                    # lambda_v␣
↪\in [0,1)
        x[1]=u[1]*(1-u[0])                                           # lambda_s␣
↪\in [0,lambda_v)

        return x

    def model_fft(theta,detector,T,fs,Omega=628,tau=0.1,event=0):
            #Building the source_amplitude
            phi=true_arr[2:7]
            if 1-theta[0]-theta[1]-true_arr[9]**2<0 or␣
↪theta[0]-true_arr[10]**2<0: return None
            e_plus,e_x=np.sqrt(1-theta[0]-theta[1]-true_arr[9]**2),np.
↪sqrt(theta[0]-true_arr[10]**2)
            e_cross,e_y=true_arr[9],true_arr[10]
            e_s=np.sqrt(theta[1])
            r=true_arr[11]*np.array([e_plus,e_cross,e_x,e_y,e_s])
            c=P2R(r,phi)
            ampl={event: {}}
            ampl[event]['plus']= c[0]
            ampl[event]['cross']= c[1]
            ampl[event]['x']= c[2]
            ampl[event]['y']= c[3]
            ampl[event]['b']= c[4]
            so=Source(true_arr[0],true_arr[1],np.array([0]),ampl,gmst_time=t_0)
            res=detector.SinGausResponse(so,T=T,fs=fs,Omega=Omega,tau=tau)
            return np.fft.rfft(res[event]['pure_signal'])

    def lnlike(theta):
        delta_fft={}
        delta_fft_sqr={}
        exp=0
        for k in response[0].keys():
            if model_fft(theta,detector=Net.web[k],T=T,fs=fs) is None: return␣
↪-np.inf
            delta_fft[k]=data_fft[k]-model_fft(theta,detector=Net.
↪web[k],T=T,fs=fs)
            delta_fft_sqr[k]=np.abs(delta_fft[k])**2
```

```
            exp+=np.sum(-2*(delta_fft_sqr[k][T*10:]/psd[k][T*10:])*df/fs**2-0.
↪5*np.log(np.pi*T*psd[k][T*10:]/2))
        return exp

    truths=true_arr[7:9]
    labels=['$\lambda_v$','$\lambda_s$']
    t5=time()
    lambdasampler = NestedSampler(lnlike, prior_transform,2)
    lambdasampler.run_nested(dlogz=40)
    lambdaresults = lambdasampler.results
    t5_end=time()
    plot_result(lambdaresults,truths,labels)
```

6 DATA storing and plotting functions

[ ]:
```
def lambda_res(data):
    SNR=np.array(list(data['SNR'][0].values()))
    res=data['lambda']['res']
    time=data['lambda']['time']
    logZdynesty = res.logz[-1]        # value of logZ
    logZerrdynesty = res.logzerr[-1]  # estimate of the statistcal uncertainty␣
↪on logZ

    # posterior samples
    weights = np.exp(res['logwt'] - res['logz'][-1])
    samples_dynesty = resample_equal(res.samples, weights)
    print('weights are fine!')
    lambda_v=np.zeros(len(samples_dynesty))
    lambda_s=np.zeros(len(samples_dynesty))
    for i in range(len(samples_dynesty)): lambda_v[i]=samples_dynesty[i][0]
    for i in range(len(samples_dynesty)): lambda_s[i]=samples_dynesty[i][1]
    resdict={}
    resdict['samples']=samples_dynesty
    resdict['lv_mu'] = np.mean(samples_dynesty[:,0])      # mean of lambda_v␣
↪samples
    resdict['lv_sig'] = np.std(samples_dynesty[:,0])      # standard deviation␣
↪of lambda_v samples
    resdict['ls_mu'] = np.mean(samples_dynesty[:,1])      # mean of lambda_s␣
↪samples
    resdict['ls_sig'] = np.std(samples_dynesty[:,1])      # standard deviation␣
↪of lambda_s samples
    resdict['cc'] = np.corrcoef(samples_dynesty.T)[0,1]   # correlation␣
↪coefficient between parameters
```

```
    resdict['npos'] = len(samples_dynesty)                  # number of posterior␣
↪samples
    resdict['logZ'] = logZdynesty                           # log marginalised␣
↪likelihood
    resdict['logZerr'] = logZerrdynesty                     # uncertainty on log(Z)
    resdict['time'] = time                                  #running time of the␣
↪bayes code (in seconds)
    resdict['v'] = lambda_v
    resdict['s'] = lambda_s
    resdict['SNR_mu']=np.mean(SNR)
    resdict['SNR_std']=np.std(SNR)/np.mean(SNR)
    return resdict

def trydict(data):
    try:
        data['lambda_res']=lambda_res(data)
        print('resdict_created')
        return 1
    except Exception:
        print('err_trydict')
        return 0

def plot_dy(data):
    res=data['lambda']['res']
    truths=[data['true']['lambda_v'], data['true']['lambda_s']]
    labels=['$\lambda_v$','$\lambda_s$']
    cfig, caxes = dyplot.cornerplot(res, color='blue', truths=truths,␣
↪truth_color='red', show_titles=True, max_n_ticks=5, quantiles=None,␣
↪labels=labels)
    fg, ax = dyplot.cornerpoints(res, cmap='plasma', truths=truths, kde=False,␣
↪labels=labels)
    fig, axes = dyplot.traceplot(res, truths=truths, truth_color='red',␣
↪show_titles=True, trace_cmap='viridis', connect=True,␣
↪connect_highlight=range(5), labels=labels)

def plot_cor(data):
    """
    Function to plot posteriors using corner.py and scipy's gaussian KDE␣
↪function.
    """
    samples=data['resdict']['samples']
    fig = corner.corner(samples, labels=[r'$\lambda_v$', r'$\lambda_s$'],␣
↪hist_kwargs={'density': True})

    # plot KDE smoothed version of distributions
    for axidx, samps in zip([0, 3], samples.T):
```

```
        kde = gaussian_kde(samps)
        xvals = fig.axes[axidx].get_xlim()
        xvals = np.linspace(xvals[0], xvals[1], 100)
        fig.axes[axidx].plot(xvals, kde(xvals), color='firebrick')
```

[ ]:
```
data={'response': response, 'SNR': SNR, 'true': true}

if allpar is True: data['allpar']={'results':results,'time':t1_end-t1}
if sixpar is True: data['sixpar']={'results':halfresults,'time':t2_end-t2}
if skypar is True: data['skypar']={'results':skyresults,'time':t3_end-t3}
if amppar is True: data['amppar']={'results':ampresults,'time':t4_end-t4}
if lambdapar is True: data['lambdapar']={'results':lambdaresults,'time':
 ↪t5_end-t5}

trydict(data)

filename='data'

# Store data (serialize)
with open(filename+'.pickle', 'wb') as handle:
    print('Saving data in %s'%filename)
    pickle.dump(data, handle, protocol=pickle.HIGHEST_PROTOCOL)

#Get data (deserialize)
with open(filename+'.pickle', 'rb') as handle:
    print('Getting data from %s'%filename)
    data= pickle.load(handle)
```

7 APPENDIX) Uni- and Bi- dimensional Study of the Likelihood

[ ]:
```
def model_fft(theta,detector,T,fs,Omega=628,tau=0.1,event=0):
        #Building the source_amplitude
        phi=theta[2:7]
        e_plus,e_x=np.sqrt(1-theta[7]-theta[8]-theta[9]**2),np.
 ↪sqrt(theta[7]-theta[10]**2)
        e_cross,e_y=theta[9],theta[10]
        e_s=np.sqrt(theta[8])
        r=theta[11]*np.array([e_plus,e_cross,e_x,e_y,e_s])
        c=P2R(r,phi)
        ampl={event: {}}
        ampl[event]['plus']= c[0]
        ampl[event]['cross']= c[1]
        ampl[event]['x']= c[2]
        ampl[event]['y']= c[3]
        ampl[event]['b']= c[4]
        so=Source(theta[0], theta[1], np.array([0]), ampl,gmst_time=t_0)
```

```
        res=detector.SinGausResponse(so, T=T, fs=fs, Omega=Omega, tau=tau)
        return np.fft.rfft(res[event]['pure_signal'])

def lnlike(theta):
    delta_fft={}
    delta_fft_sqr={}
    exp=0
    for k in response[0].keys():
        if model_fft(theta,detector=Net.web[k],T=T,fs=fs) is None: return -np.inf
        delta_fft[k]=data_fft[k]-model_fft(theta, detector=Net.web[k],T=T,fs=fs)
        delta_fft_sqr[k]=np.abs(delta_fft[k])**2
        exp+=np.sum(-2*(delta_fft_sqr[k][T*10:]/psd[k][T*10:])*df/fs**2-0.5*np.
 ↪log(np.pi*T*psd[k][T*10:]/2))
    return exp
```

[ ]:
```
#ra,dec and phases

k=2
N=400
false=np.copy(true_arr)

delta=np.zeros(N)
for i in range(N):
    delta[i]=(lnlike(false)-lnlike(true_arr))
    print('%d'%i,end="\r")
    false[k]+=2*np.pi/N

plt.figure()
plt.plot(2/N*np.arange(N),delta)
plt.title('$\Delta$L varying $\phi_+$')
plt.xlabel('$\phi_+$ ($\pi$ unit)')
plt.show()
```

[ ]:
```
#amplitude param

for k in range(4):

    N=500
    false=np.copy(true_arr)

    delta=np.zeros(N)
    xdelta=np.zeros(N)
    for i in range(N):
        delta[i]=(lnlike(false)-lnlike(true_arr))
        xdelta[i]=false[k+7]
        print('%d'%i,end="\r")
        false[k+7]=np.random.random_sample()
```

```
        while((1-false[7]-false[8]-false[9]**2)<0 or (false[7]-false[10]**2)<0):
            false[k+7]=np.random.random_sample()

    plt.figure()
    plt.plot(xdelta,delta)
    plt.axvline(x=true_arr[k+7],color='red')
    plt.title('Likelihood varying %s'%list(true.keys())[k+7])
    plt.show()
```

[ ]:
```
#overall_amplitude

N=500
false=np.copy(true_arr)
delta=np.zeros(N)

falseamp=np.logspace(0,2,N,base=10)/1e22

for i in range(N):
    false[11]=falseamp[i]
    delta[i]=(lnlike(false)-lnlike(true_arr))
    print('%d'%i,end="\r")

plt.figure()
plt.loglog(falseamp,np.abs(delta))
plt.axvline(x=true_arr[11],color='red')
plt.title('|$\Delta$L| varying $A_0$')
plt.xlabel('$A_0$ (a.u.)')
plt.show()

#I am plotting the deltaln absolute value, which is 0 only for the true value,␣
 ↪otherwise positive
```

[ ]:
```
def model_fft(theta,detector,T,fs,Omega=628,tau=0.1,event=0):
        #Building the source_amplitude
        phi=true_arr[2:7]
        e_plus,e_x=np.sqrt(1-true_arr[7]-true_arr[8]-true_arr[9]**2),np.
 ↪sqrt(true_arr[7]-true_arr[10]**2)
        e_cross,e_y=true_arr[9],true_arr[10]
        e_s=np.sqrt(true_arr[8])
        r=true_arr[11]*np.array([e_plus,e_cross,e_x,e_y,e_s])
        c=P2R(r,phi)
        ampl={event: {}}
        ampl[event]['plus']= c[0]
        ampl[event]['cross']= c[1]
        ampl[event]['x']= c[2]
        ampl[event]['y']= c[3]
        ampl[event]['b']= c[4]
```

```
        so=Source(theta[0],theta[1],np.array([0]),ampl,gmst_time=t_0)
        res=detector.SinGausResponse(so,T=T,fs=fs,Omega=Omega,tau=tau)
        return np.fft.rfft(res[event]['pure_signal'])

def lnlike(theta):
    delta_fft={}
    delta_fft_sqr={}
    exp=0
    for k in response[0].keys():
        if model_fft(theta,detector=Net.web[k],T=T,fs=fs) is None: return -np.inf
        delta_fft[k]=data_fft[k]-model_fft(theta,detector=Net.web[k],T=T,fs=fs)
        delta_fft_sqr[k]=np.abs(delta_fft[k])**2
        exp+=np.sum(-2*(delta_fft_sqr[k][T*10:]/psd[k][T*10:])*df/fs**2-0.5*np.
 ↪log(np.pi*T*psd[k][T*10:]/2))
    return exp-2100000

fig = plt.figure()
ax = fig.gca(projection='3d')
N=50
# Make data.
x = np.arange(0, 2*np.pi, 2*np.pi/N)
y = np.arange(-np.pi,np.pi, 2*np.pi/N)
X, Y = np.meshgrid(x, y)
Z=np.zeros((N,N))
for i in range(N):
    for j in range(N):
        Z[i,j] = lnlike(np.array([x[i],y[j]]))

# Plot the surface.
surf = ax.plot_surface(X, Y, Z, cmap=cm.get_cmap('jet'),
                       linewidth=0, antialiased=False)

fig.colorbar(surf, shrink=0.5, aspect=5)
plt.show()
```

[ ]:
```
def model_fft(theta,detector,T,fs,Omega=628,tau=0.1,event=0):
        #Building the source_amplitude
        phi=true_arr[2:7]
        if 1-theta[0]-theta[1]-true_arr[9]**2<0 or theta[0]-true_arr[10]**2<0:␣
 ↪return None
        e_plus,e_x=np.sqrt(1-theta[0]-theta[1]-true_arr[9]**2),np.
 ↪sqrt(theta[0]-true_arr[10]**2)
        e_cross,e_y=true_arr[9],true_arr[10]
        e_s=np.sqrt(theta[1])
        r=true_arr[11]*np.array([e_plus,e_cross,e_x,e_y,e_s])
        c=P2R(r,phi)
        ampl={event: {}}
```

```
        ampl[event]['plus']= c[0]
        ampl[event]['cross']= c[1]
        ampl[event]['x']= c[2]
        ampl[event]['y']= c[3]
        ampl[event]['b']= c[4]
        so=Source(true_arr[0],true_arr[1],np.array([0]),ampl,gmst_time=t_0)
        res=detector.SinGausResponse(so,T=T,fs=fs,Omega=Omega,tau=tau)
        return np.fft.rfft(res[event]['pure_signal'])

def lnlike(theta):
    delta_fft={}
    delta_fft_sqr={}
    exp=0
    for k in response[0].keys():
        if model_fft(theta,detector=Net.web[k],T=T,fs=fs) is None: return -np.inf
        delta_fft[k]=data_fft[k]-model_fft(theta,detector=Net.web[k],T=T,fs=fs)
        delta_fft_sqr[k]=np.abs(delta_fft[k])**2
        exp+=np.sum(-2*(delta_fft_sqr[k][T*10:]/psd[k][T*10:])*df/fs**2-0.5*np.
 ↪log(np.pi*T*psd[k][T*10:]/2))
    return exp-2100000

fig2 = plt.figure()
ax2 = fig2.gca(projection='3d')

# Make data.
x = np.arange(0, 0.5, 0.01)
y = np.arange(0, 0.5, 0.01)
X, Y = np.meshgrid(x, y)
Z=np.zeros((50,50))
for i in range(50):
    for j in range(50):
        Z[i,j] = lnlike(np.array([x[i],y[j]]))

# Plot the surface.
surf2 = ax2.plot_surface(X, Y, Z, cmap=cm.get_cmap('jet'),
                       linewidth=0, antialiased=False)

fig2.colorbar(surf2, shrink=0.5, aspect=5)
plt.show()
```

Bibliography

[1] Abbott, B., et al. Tests of General Relativity with GW150914. *Physical Review Letters*, **116** (2016). Available from: http://dx.doi.org/10.1103/PhysRevLett.116.221101, doi:10.1103/physrevlett.116.221101. (Cited on page 64.)

[2] Abbott, B. et al. Gravitational Waves and Gamma-rays from a Binary Neutron Star Merger: GW170817 and GRB 170817A. *Astrophys. J. Lett.*, **848** (2017), L13. arXiv:1710.05834, doi:10.3847/2041-8213/aa920c. (Cited on page 25.)

[3] Abbott, B. et al. GW170817: Observation of Gravitational Waves from a Binary Neutron Star Inspiral. *Phys. Rev. Lett.*, **119** (2017), 161101. arXiv:1710.05832, doi:10.1103/PhysRevLett.119.161101. (Cited on page 25.)

[4] Abbott, B., et al. Gwtc-1: A gravitational-wave transient catalog of compact binary mergers observed by ligo and virgo during the first and second observing runs. *Physical Review X*, **9** (2019). Available from: http://dx.doi.org/10.1103/PhysRevX.9.031040, doi:10.1103/physrevx.9.031040. (Cited on pages 24 and 86.)

[5] Abbott, B., et al. Tests of general relativity with the binary black hole signals from the LIGO-Virgo catalog GWTC-1. *Physical Review D*, **100** (2019). doi:10.1103/PhysRevD.100.104036. (Cited on page 36.)

[6] Abbott, B. P., et al. Observation of gravitational waves from a binary black hole merger. *Phys. Rev. Lett.*, **116** (2016), 061102. Available from: https://link.aps.org/doi/10.1103/PhysRevLett.116.061102, doi:10.1103/PhysRevLett.116.061102. (Cited on page 24.)

[7] Abbott, B. P. et al. Multi-messenger Observations of a Binary Neutron Star Merger. *Astrophys. J.*, **848** (2017), L12. arXiv:1710.05833, doi:10.3847/2041-8213/aa91c9. (Cited on pages 25 and 63.)

[8] Abbott, B. P. et al. Tests of General Relativity with GW170817. *Phys. Rev. Lett.*, **123** (2019), 011102. arXiv:1811.00364, doi:10.1103/PhysRevLett.123.011102. (Cited on page 85.)

[9] Adhikari, R. X. Gravitational radiation detection with laser interferometry. *Rev. Mod. Phys.*, **86** (2014), 121. Available from: https://link.aps.org/doi/10.1103/RevModPhys.86.121, doi:10.1103/RevModPhys.86.121. (Cited on page 71.)

[10] Akutsu, T. et al. Overview of KAGRA: Detector design and construction history (2020). arXiv:2005.05574. (Cited on page 70.)

[11] Alexander, S. and Yunes, N. Chern–simons modified general relativity. *Physics Reports*, **480** (2009), 1–55. Available from: http://dx.doi.org/10.1016/j.physrep.2009.07.002, doi:10.1016/j.physrep.2009.07.002. (Cited on page 21.)

[12] Arfken, G. *Mathematical Methods for Physicists*. Academic Press, Inc., San Diego, third edn. (1985). (Cited on page 68.)

[13] Barsotti, L., McCuller, L., Evans, M., and Fritschel, P. The a+ design curve. *LIGO DCC*, **LIGO-T1800042** (2018). Available from: https://dcc.ligo.org/public/0149/T1800042/004/T1800042-v4.pdf. (Cited on page 92.)

[14] Blanchet, L. Gravitational radiation from post-newtonian sources and inspiralling compact binaries. *Living Reviews in Relativity*, **17** (2014), 2. Available from: https://doi.org/10.12942/lrr-2014-2, doi:10.12942/lrr-2014-2. (Cited on page 86.)

[15] Brans, C. and Dicke, R. H. Mach's principle and a relativistic theory of gravitation. *Phys. Rev.*, **124** (1961), 925. Available from: https://link.aps.org/doi/10.1103/PhysRev.124.925, doi:10.1103/PhysRev.124.925. (Cited on page 18.)

[16] Brooks, S., Gelman, A., Jones, G., and Meng, X.-L. *Handbook of Markov Chain Monte Carlo*. CRC press (2011). (Cited on page 81.)

[17] Carroll, S. M. *Spacetime and Geometry*. Cambridge University Press (2019). ISBN 978-0-8053-8732-2, 978-1-108-48839-6, 978-1-108-77555-7. (Cited on page 40.)

[18] Chandrasekhar, S. and Contopoulos, G. On a post-galilean transformation appropriate to the post-newtonian theory of einstein, infeld and hoffmann. *Proc. R. Soc. A*, **298** (1967), 123. doi:10.1098/rspa.1967.0095. (Cited on page 16.)

[19] Chatziioannou, K., Yunes, N., and Cornish, N. Model-independent test of general relativity: An extended post-einsteinian framework with complete polarization content. *Physical Review D*, **86** (2012). [Erratum: Phys. Rev.D95,no.12,129901(2017)]. Available from: http://dx.doi.org/10.1103/PhysRevD.86.022004, doi:10.1103/PhysRevD.86.022004,10.1103/PhysRevD.95.129901. (Cited on pages 63, 85, 86, 87, and 103.)

[20] Cornish, N. J. and Littenberg, T. B. BayesWave: Bayesian Inference for Gravitational Wave Bursts and Instrument Glitches. *Class. Quant. Grav.*, **32** (2015), 135012. arXiv:1410.3835, doi:10.1088/0264-9381/32/13/135012. (Cited on page 63.)

[21] de Rham, C. Massive gravity. *Living Reviews in Relativity*, **17** (2014). Available from: http://dx.doi.org/10.12942/lrr-2014-7, doi:10.12942/lrr-2014-7. (Cited on page 21.)

[22] de Rham, C., Deskins, J. T., Tolley, A. J., and Zhou, S.-Y. Graviton mass bounds. *Rev. Mod. Phys.*, **89** (2017), 025004. Available from: https://link.aps.org/doi/10.1103/RevModPhys.89.025004, doi:10.1103/RevModPhys.89.025004. (Cited on page 36.)

[23] Eardley, D. M., Lee, D. L., and Lightman, A. P. Gravitational-wave observations as a tool for testing relativistic gravity. *Phys. Rev. D*, **8** (1973), 3308. Available from: https://link.aps.org/doi/10.1103/PhysRevD.8.3308, doi:10.1103/PhysRevD.8.3308. (Cited on pages 39 and 52.)

[24] Eardley, D. M., Lee, D. L., Lightman, A. P., Wagoner, R. V., and Will, C. M. Gravitational-wave observations as a tool for testing relativistic gravity. *Phys. Rev. Lett.*, **30** (1973), 884. Available from: https://link.aps.org/doi/10.1103/PhysRevLett.30.884, doi:10.1103/PhysRevLett.30.884. (Cited on page 39.)

[25] Ehlers, J., Rosenblum, A., Goldberg, J. N., and Havas, P. Comments on gravitational radiation damping and energy loss in binary systems. *Astrophysical Journal Letters*, **208** (1976), L77. doi:10.1086/182236. (Cited on page 24.)

[26] Einstein, A. Näherungsweise Integration der Feldgleichungen der Gravitation. *Sitzungsberichte der Königlich Preußischen Akademie der Wissenschaften (Berlin)*, (1916), 688. (Cited on page 24.)

[27] Einstein, A. Über Gravitationswellen. *Sitzungsberichte der Königlich Preußischen Akademie der Wissenschaften (Berlin)*, (1918), 154. (Cited on pages 24 and 31.)

[28] Einstein, A. and Rosen, N. On Gravitational Waves. *Journal of The Franklin Institute*, **223** (1937), 43. doi:10.1016/S0016-0032(37)90583-0. (Not cited.)

[29] Eling, C. and Jacobson, T. Static post-newtonian equivalence of general relativity and gravity with a dynamical preferred frame. *Phys. Rev. D*, **69** (2004), 064005. Available from: https://link.aps.org/doi/10.1103/PhysRevD.69.064005, doi:10.1103/PhysRevD.69.064005. (Cited on page 19.)

[30] Faller, J. E. and Cook, A. H. e. a. Gravity. *Encyclopaedia Britannica*, (2019). Available from: https://www.britannica.com/science/gravity-physics. (Not cited.)

[31] Flanagan, E. E. and Hughes, S. A. The basics of gravitational wave theory. *New Journal of Physics*, **7** (2005), 204. Available from: "https://doi.org/10.1088%2F1367-2630%2F7%2F1%2F204", doi:10.1088/1367-2630/7/1/204. (Not cited.)

[32] Foster, B. Z. Strong field effects on binary systems in einstein-aether theory. *Physical Review D*, **76** (2007). Available from: http://dx.doi.org/10.1103/PhysRevD.76.084033, doi:10.1103/physrevd.76.084033. (Cited on page 20.)

[33] Foster, B. Z. and Jacobson, T. Post-newtonian parameters and constraints on einstein-aether theory. *Phys. Rev. D*, **73** (2006), 064015. Available from: https://link.aps.org/doi/10.1103/PhysRevD.73.064015, doi:10.1103/PhysRevD.73.064015. (Cited on page 19.)

[34] Fowles, G. *Introduction to Modern Optics*. Dover Books on Physics Series. Dover Publications (1989). ISBN 9780486659572. Available from: https://books.google.it/books?id=SL1n9TuJ5YMC. (Cited on pages 46 and 49.)

[35] Gong, Y., Hou, S., Liang, D., and Papantonopoulos, E. Gravitational waves in einstein-æther and generalized teves theory after gw170817. *Physical Review D*, **97** (2018). Available from: http://dx.doi.org/10.1103/PhysRevD.97.084040, doi:10.1103/physrevd.97.084040. (Cited on page 35.)

[36] GWIC-3G. Gravitational-wave astronomy with the next-generation earth-based observatories. https://gwic.ligo.org/3Gsubcomm/documents/3G-observatory-science-case.pdf (2019). (Cited on page 58.)

[37] Isi, M., Pitkin, M., and Weinstein, A. J. Probing Dynamical Gravity with the Polarization of Continuous Gravitational Waves. *Phys. Rev.*, **D96** (2017), 042001. arXiv:1703.07530, doi:10.1103/PhysRevD.96.042001. (Cited on pages 78, 89, 94, and 103.)

[38] Isi, M. and Weinstein, A. J. Probing gravitational wave polarizations with signals from compact binary coalescences. *LIGO DCC*, (2017). arXiv:1710.03794. (Cited on pages 52, 59, 64, and 85.)

[39] Jacobson, T. and Mattingly, D. Gravity with a dynamical preferred frame. *Physical Review D*, **64** (2001). Available from: http://dx.doi.org/10.1103/PhysRevD.64.024028, doi:10.1103/physrevd.64.024028. (Cited on page 19.)

[40] Jacobson, T. and Mattingly, D. Einstein-aether waves. *Physical Review D*, **70** (2004). Available from: http://dx.doi.org/10.1103/PhysRevD.70.024003, doi:10.1103/physrevd.70.024003. (Cited on pages 19 and 53.)

[41] Landau, L. and Lifshitz, E. M. *The Classical Theory of Fields (Fourth Edition)*, vol. 2 of *Course of Theoretical Physics*. Pergamon, Amsterdam, fourth edition edn. (1975). ISBN 978-0-08-025072-4. Available from: http://www.sciencedirect.com/science/article/pii/B9780080250724500058, doi:https://doi.org/10.1016/B978-0-08-025072-4.50005-8. (Cited on page 25.)

[42] Lee, D. L., Lightman, A. P., and Ni, W. T. Conservation laws and variational principles in metric theories of gravity. *Phys. Rev. D*, **10** (1974), 1685. Available from: https://link.aps.org/doi/10.1103/PhysRevD.10.1685, doi:10.1103/PhysRevD.10.1685. (Cited on pages 16, 17, and 32.)

[43] Martynov, D., et al. Sensitivity of the advanced ligo detectors at the beginning of gravitational wave astronomy. *Physical Review D*, **93** (2016). Available from: http://dx.doi.org/10.1103/PhysRevD.93.112004, doi:10.1103/physrevd.93.112004. (Cited on pages 69 and 70.)

[44] Mattingly, D. and Jacobson, T. Relativistic gravity with a dynamical preferred frame. *CPT and Lorentz Symmetry*, (2002). Available from: http://dx.doi.org/10.1142/9789812778123_0042, doi:10.1142/9789812778123_0042. (Cited on page 19.)

[45] Michelson, A. A. Art. xxi.–the relative motion of the earth and the luminiferous ether. *American Journal of Science (1880-1910)*, **22** (1881), 120. (Cited on pages 46 and 47.)

[46] Michelson, M. E. W., A. A. On the relative motion of the earth and the luminiferous ether. *Amer. J. Sci*, **34** (1887), 333. (Cited on page 47.)

[47] Milgrom, M. A modification of the Newtonian dynamics - Implications for galaxies. *Astrophysical Journal*, **270** (1983), 371. doi:10.1086/161131. (Cited on page 20.)

[48] Misner, C. W., Thorne, K. S., and Wheeler, J. A. *Gravitation*. Princeton University Press (2017). (Cited on pages 9, 12, 17, 33, and 41.)

[49] Newman, E. and Penrose, R. An Approach to gravitational radiation by a method of spin coefficients. *J. Math. Phys.*, **3** (1962), 566. doi:10.1063/1.1724257. (Cited on page 39.)

[50] Nitz, A., et al. gwastro/pycbc: Pycbc v1.13.1 release (2018). Available from: https://doi.org/10.5281/zenodo.1490104, doi:10.5281/zenodo.1490104. (Cited on pages 85 and 90.)

[51] Nordtvedt, K. Equivalence principle for massive bodies. ii. theory. *Phys. Rev.*, **169** (1968), 1017. Available from: https://link.aps.org/doi/10.1103/PhysRev.169.1017, doi:10.1103/PhysRev.169.1017. (Cited on page 8.)

[52] Pati, M. E. and Will, C. M. Post-newtonian gravitational radiation and equations of motion via direct integration of the relaxed einstein equations: Foundations. *Phys. Rev. D*, **62** (2000), 124015. Available from: https://link.aps.org/doi/10.1103/PhysRevD.62.124015, doi:10.1103/PhysRevD.62.124015. (Cited on pages 26 and 27.)

[53] Pati, M. E. and Will, C. M. Post-newtonian gravitational radiation and equations of motion via direct integration of the relaxed einstein equations. ii. two-body equations of motion to second post-newtonian order, and radiation reaction to 3.5 post-newtonian order. *Phys. Rev. D*, **65** (2002), 104008. Available from: https://link.aps.org/doi/10.1103/PhysRevD.65.104008, doi:10.1103/PhysRevD.65.104008. (Cited on page 26.)

[54] Patrone, S. and Weinstein, A. J. Gravitational wave polarizations: a general relativity test. *LIGO DCC*, **LIGO-T1900468** (2020). Available from: https://dcc.ligo.org/LIGO-T1900468/public. (Cited on pages iv, x, 83, and 102.)

[55] Petrov, A. Z. Classification of spaces defining gravitational fields. *Jubilee collection*, **114** (1954), 55–69. (Cited on page 43.)

[56] Poisson, E. and Will, C. *Gravity: Newtonian, Post-Newtonian, Relativistic*. Cambridge University Press (2014). ISBN 9781107032866. Available from: https://books.google.it/books?id=PZ5cAwAAQBAJ. (Cited on pages 17 and 54.)

[57] Punturo, M. Et letter of intent. http://www.et-gw.eu/index.php/letter-of-intent (2019). (Cited on page 58.)

[58] Sampson, L., Yunes, N., and Cornish, N. Rosetta stone for parametrized tests of gravity. *Physical Review D*, **88** (2013). Available from: http://dx.doi.org/10.1103/PhysRevD.88.064056, doi:10.1103/physrevd.88.064056. (Cited on page 87.)

[59] Sathyaprakash, B. et al. Scientific Objectives of Einstein Telescope. *Class. Quant. Grav.*, **29** (2012), 124013. [Erratum: Class. Quant. Grav.30,079501(2013)]. arXiv:1206.0331, doi:10.1088/0264-9381/29/12/124013,10.1088/0264-9381/30/7/079501. (Cited on page 55.)

[60] Sathyaprakash, B. S. and Schutz, B. F. Physics, astrophysics and cosmology with gravitational waves. *Living Reviews in Relativity*, **12** (2009), 2. Available from: https://doi.org/10.12942/lrr-2009-2, doi:10.12942/lrr-2009-2. (Not cited.)

[61] Skilling, J. Nested Sampling. In *American Institute of Physics Conference Series* (edited by R. Fischer, R. Preuss, and U. V. Toussaint), vol. 735 of *American Institute of Physics Conference Series*, pp. 395–405 (2004). doi:10.1063/1.1835238. (Cited on page 81.)

[62] Skilling, J. Nested sampling for general bayesian computation. *Bayesian Anal.*, **1** (2006), 833. Available from: https://doi.org/10.1214/06-BA127, doi:10.1214/06-BA127. (Cited on page 80.)

[63] Skordis, C. The tensor-vector-scalar theory and its cosmology. *Classical and Quantum Gravity*, **26** (2009), 143001. Available from: http://dx.doi.org/10.1088/0264-9381/26/14/143001, doi:10.1088/0264-9381/26/14/143001. (Cited on page 20.)

[64] Speagle, J. S. dynesty: A dynamic nested sampling package for estimating bayesian posteriors and evidences (2019). arXiv:1904.02180. (Cited on pages 81 and 85.)

[65] Taylor, J. H., Fowler, L. A., and McCulloch, P. M. Measurements of general relativistic effects in the binary pulsar psr1913 + 16. *Nature*, **277** (1979), 437. Available from: https://doi.org/10.1038/277437a0, doi:10.1038/277437a0. (Cited on page 24.)

[66] Thorne, K. and Blandford, R. *Modern Classical Physics: Optics, Fluids, Plasmas, Elasticity, Relativity, and Statistical Physics*. Princeton University Press (2017). ISBN 9781400848898. Available from: https://books.google.it/books?id=U1S6BQAAQBAJ. (Cited on page 74.)

[67] Thorne, K. S., Lee, D. L., and Lightman, A. P. Foundations for a theory of gravitation theories. *Phys. Rev. D*, **7** (1973), 3563. Available from: https://link.aps.org/doi/10.1103/PhysRevD.7.3563, doi:10.1103/PhysRevD.7.3563. (Cited on page 6.)

[68] Veitch, J. and Vecchio, A. Bayesian coherent analysis of in-spiral gravitational wave signals with a detector network. *Phys. Rev. D*, **81** (2010). doi:10.1103/PhysRevD.81.062003. (Cited on page 82.)

[69] Veitch, J., et al. Parameter estimation for compact binaries with ground-based gravitational-wave observations using the lalinference software library. *Phys. Rev. D*, **91** (2015), 042003. Available from: https://link.aps.org/doi/10.1103/PhysRevD.91.042003, doi:10.1103/PhysRevD.91.042003. (Cited on page 79.)

[70] Visser, M. Lorentz symmetry breaking as a quantum field theory regulator. *Phys. Rev. D*, **80** (2009), 025011. Available from: https://link.aps.org/doi/10.1103/PhysRevD.80.025011, doi:10.1103/PhysRevD.80.025011. (Cited on page 19.)

[71] Waskom, M. Seaborn documentation. https://seaborn.pydata.org/generated/seaborn.violinplot.html. (Cited on page 95.)

[72] Weiss, R. Gravitational radiation. *Rev. Mod. Phys.*, **71** (1999), S187. Available from: https://link.aps.org/doi/10.1103/RevModPhys.71.S187, doi:10.1103/RevModPhys.71.S187. (Cited on page 48.)

[73] Wigner, E. On unitary representations of the inhomogeneous lorentz group. *Annals of Mathematics*, **40** (1939), 149. Available from: http://www.jstor.org/stable/1968551. (Cited on page 43.)

[74] Will, C. M. Theoretical Frameworks for Testing Relativistic Gravity. II. Parametrized Post-Newtonian Hydrodynamics, and the Nordtvedt Effect. *Astrophysical Journal*, **163** (1971), 611. doi:10.1086/150804. (Cited on page 8.)

[75] Will, C. M. The confrontation between general relativity and experiment. *Living Reviews in Relativity*, **9** (2006). Available from: https://doi.org/10.12942/lrr-2006-3, doi:10.12942/lrr-2006-3. (Cited on pages 7 and 22.)

[76] Will, C. M. *Theory and experiment in gravitational physics*. Cambridge university press (2018). (Cited on pages 4, 11, 13, 14, 15, 17, 27, and 35.)

[77] Will, C. M. and Nordtvedt, J., Kenneth. Conservation Laws and Preferred Frames in Relativistic Gravity. I. Preferred-Frame Theories and an Extended PPN Formalism. *Astrophysical Journal*, **177** (1972), 757. doi:10.1086/151754. (Cited on page 8.)

[78] Will, C. M. and Wiseman, A. G. Gravitational radiation from compact binary systems: Gravitational waveforms and energy loss to second post-newtonian order. *Phys. Rev. D*, **54** (1996), 4813. Available from: https://link.aps.org/doi/10.1103/PhysRevD.54.4813, doi:10.1103/PhysRevD.54.4813. (Cited on page 26.)

[79] Yagi, K., Blas, D., Barausse, E., and Yunes, N. Constraints on einstein-Æther theory and hořava gravity from binary pulsar observations. *Physical Review D*, **89** (2014). Available from: http://dx.doi.org/10.1103/PhysRevD.89.084067, doi:10.1103/physrevd.89.084067. (Cited on page 20.)

[80] Yunes, N. and Pretorius, F. Fundamental theoretical bias in gravitational wave astrophysics and the parametrized post-einsteinian framework. *Physical Review D*, **80** (2009). Available from: http://dx.doi.org/10.1103/PhysRevD.80.122003, doi:10.1103/physrevd.80.122003. (Cited on pages 87 and 103.)